

## University of Southampton Research Repository ePrints Soton

Copyright © and Moral Rights for this thesis are retained by the author and/or other copyright owners. A copy can be downloaded for personal non-commercial research or study, without prior permission or charge. This thesis cannot be reproduced or quoted extensively from without first obtaining permission in writing from the copyright holder/s. The content must not be changed in any way or sold commercially in any format or medium without the formal permission of the copyright holders.

When referring to this work, full bibliographic details including the author, title, awarding institution and date of the thesis must be given e.g.

AUTHOR (year of submission) "Full thesis title", University of Southampton, name of the University School or Department, PhD Thesis, pagination

**UNIVERSITY OF SOUTHAMPTON**

**FACULTY OF PHYSICAL SCIENCES AND ENGINEERING  
OPTOELECTRONICS RESEARCH CENTRE**

# **Direct write technologies for fabricating patterned metals and glasses**

by  
**Ehab Saleh**

Thesis for the degree of Doctor of Philosophy

March 2013



UNIVERSITY OF SOUTHAMPTON

## **ABSTRACT**

FACULTY OF ENGINEERING, SCIENCE AND MATHEMATICS

OPTOELECTRONICS RESEARCH CENTRE

Doctor of Philosophy

**Direct write technologies for fabricating patterned metals and glasses**

**By Ehab Saleh**

In the past few decades direct writing became a widely pervasive approach to producing well defined patterns of a variety of materials. Due to its flexibility, this mask-less and etch-free patterning approach shows great potential for rapid prototyping and manufacturing purposes.

This research aims to implement direct writing of challenging materials like metals and glasses, and also aims to achieve high resolution mask-less pattern printing with minimal pre-processing and post-processing requirements.

This work looks at different technologies to achieve the aims of the research, and intensively study and develop two approaches which have the potential of achieving these aims. Electrohydrodynamic (EHD) technology is used to achieve electrospinning of glass nano-fibres of ~100nm diameter, which is the first report to record glass electrospinning directly from glass melt. Spark-stream is another technology of direct writing, which uses electrical discharge to generate nanoparticles of a wide range of materials, with nanoparticle diameters of the range of 10 nm for gold, which is the main material explored in the spark-stream technology. These nanoparticles are focussed down to form micro-scale patterns using electrostatic 'diffusion focussing' techniques. The na-

nanoparticles are generated and focussed simultaneously and directly from the bulk material at room conditions.

# Contents

<b>ABSTRACT .....</b>	<b>i</b>
<b>Contents .....</b>	<b>i</b>
<b>List of tables .....</b>	<b>v</b>
<b>List of figures .....</b>	<b>vii</b>
<b>DECLARATION OF AUTHORSHIP.....</b>	<b>xv</b>
<b>Acknowledgements.....</b>	<b>xvii</b>
<b>1. Introduction to direct write technologies and motivations. ....</b>	<b>1</b>
1.1 Introduction .....	1
1.2 Why direct writing of metals and glasses? .....	2
1.3 Background on driving technologies .....	4
<b>2. Electrohydrodynamic (EHD) technology .....</b>	<b>11</b>
2.1 Introduction .....	11
2.2 Theory of Electrohydrodynamic EHD phenomena .....	12
2.3 Onset voltage for liquid jetting against surface tension .....	16
2.4 EHD experiments on water .....	18
2.4.1 EHD water experiment apparatus.....	19
2.4.2 Frequency analysis of liquid ejection .....	21
2.4.3 Pressure control.....	23
2.4.4 Droplet on demand.....	26
2.5 Conclusion .....	31
<b>3. Jetting glass strands using Electrohydrodynamic (EHD)</b>	
<b>technology.....</b>	<b>33</b>
3.1 Introduction .....	33
3.2 Surface tension of glasses and metals .....	34
3.3 Effect of temperature and separation gap on the electrical discharge .....	38
3.4 Experiments on borate glass .....	42
3.5 Conclusion .....	45

<b>4.</b>	<b>Introduction to Spark-Stream technology.....</b>	<b>47</b>
4.1	Introduction .....	47
4.2	Why electrical discharge .....	49
4.3	Electrical discharge phenomena .....	50
4.4	Mechanism of particle formation .....	52
4.4.1	From the vapour of the electrodes.....	52
4.4.2	From molten micro-pools .....	53
4.5	Introduction to electrostatic focussing of particles .....	53
4.6	Conclusion.....	55
<b>5.</b>	<b>Production of nanoparticles using Spark-Stream technology ...</b>	<b>57</b>
5.1	Introduction .....	57
5.2	Experiments on nanoparticle production.....	58
5.2.1	Metal and metal-oxide nanoparticles.....	58
5.2.2	Glass nano and microspheres .....	63
5.3	Properties of nanoparticles .....	66
5.3.1	Size of nanoparticles .....	66
5.3.2	Charge polarity of nanoparticles.....	69
5.3.3	Electrical resistance of deposition .....	71
5.4	Conclusion .....	74
<b>6.</b>	<b>Focussing of nanoparticles.....</b>	<b>77</b>
6.1	Introduction .....	77
6.2	Theory of electrostatic focussing .....	78
6.2.1	Concept of focussing .....	78
6.2.2	Diffusion of nanoparticle .....	80
6.2.3	Analysis of particle-particle interaction .....	82
6.2.4	Calculating the transit time of nanoparticles.....	86
6.3	Focussing of nanoparticles experimentally .....	89
6.3.1	Effect of focussing tube voltage.....	89
6.3.2	Measuring transit time and particle charge experimentally .....	94
6.3.3	Effect of diffusion and particle interaction investigated experimentally	100
6.4	Microstructure and patterns deposition.....	103
6.5	Conclusion .....	108
<b>7.</b>	<b>Further developments.....</b>	<b>111</b>
7.1	Introduction .....	111

7.2	Further development on EHD .....	112
7.3	Other spark-stream focussing configurations .....	115
7.4	Electrodes of different materials .....	119
7.5	Incorporating nanoparticles inside hollow fibres .....	121
7.6	Conclusion .....	123
<b>List of publications and conferences .....</b>		<b>125</b>
<b>Appendices .....</b>		<b>127</b>
	Appendix 1: EHD onset voltage equations.....	127
	Appendix 2: Paschen curve and field emission equations.....	129
	Appendix 3: Au nanoparticle deposition resistance.....	131
	Appendix 4: Submitted paper (to journal of nanoparticle research JNR).....	135
<b>Bibliography .....</b>		<b>151</b>





# List of tables

<i>Table 1.1 Evaluation of technologies reviewed</i>	6
<i>Table 2.1 Surface tension of some materials</i>	16
<i>Table 2.2 Zelney's empirical results to determine the constant C [22]</i>	17
<i>Table 3.1 Surface tension of molten metals [34,47,48]</i>	35
<i>Table 3.2 Surface tension of some silicate glasses. S1, A5, A6 and A7 are different silicate glass compositions [49]</i>	36
<i>Table 5.1 Effect of the focussing tube voltage polarity on the deposition of nanoparticles.</i>	70
<i>Table 6.1 Summary of the configurations used to deposit microscale spots.</i>	107



# List of figures

<i>Figure 1.1 Ring pattern of 10 <math>\mu\text{m}</math> thickness</i>	3
<i>Figure 2.1 Charge accumulation at the tip of the meniscus.</i>	13
<i>Figure 2.2 Onset instability voltage with surface tension of some materials for a 250 <math>\mu\text{m}</math> meniscus radius.</i>	18
<i>Figure 2.3 Schematic diagram of EHD setup to electrospray water</i>	19
<i>Figure 2.4 A deposited droplet associated with a pulse generated on the substrate</i>	21
<i>Figure 2.5 a) Current waveform labelled to groups 1 to 6, b) frequency spectrum of groups 1 and 6 of the current waveform</i>	22
<i>Figure 2.6 Frequency analysis of the current pulses waveform showing frequency decline with time</i>	23
<i>Figure 2.7 Pressure analysis graph</i>	24
<i>Figure 2.8 Theoretical calculations and empirical measurements of the pressure as it changes with the extension of the meniscus L</i>	25
<i>Figure 2.9 EHD apparatus with pressure control system to maintain the shape of the liquid meniscus</i>	26
<i>Figure 2.10 a) line of spots appears while printing, b) channel 2 (blue line) is HV pulse line and channel 1 (green line) is the pulses generated from each droplet at the substrate.</i>	27

Figure 2.11 High-speed camera setups, a) using laser beam reflecting from the meniscus, b) using high power LED transmitting light through the meniscus_____	28
Figure 2.12 Samples of jet cone images taken at 2000fps_____	29
Figure 2.13 High-speed camera images synchronised with the voltage oscillations appearing on the oscilloscope_____	29
Figure 2.14 Three ejections appear in images taken at 2000fps synchronised with the pulses associated with their arrival to the substrate _____	30
Figure 3.1 Surface tension of some borate glasses from [51], mol%: $\bullet$ = 100%B <sub>2</sub> O <sub>3</sub> , $\square$ = 70%B <sub>2</sub> O <sub>3</sub> -30%PbO, $\diamond$ = 70%B <sub>2</sub> O <sub>3</sub> - 30%Bi <sub>2</sub> O <sub>3</sub> ,_____	37
Figure 3.2 The breakdown threshold of air changes with temperature. Circles represent empirical results, and the solid black line represents theoretical results of the breakdown voltage ( $V = V_0 \sqrt{T_r T_g}$ ) where $V_0$ is the breakdown threshold of the gas at room temperature, $T_r$ is the room temperature in K and $T_g$ gas temperature in K [55] _____	38
Figure 3.3 Paschen curve showing the relationship between the breakdown voltage of air at atmospheric pressure and the gap between the electrodes_____	40
Figure 3.4 Paschen curve and Field emission threshold at short gaps between the electrodes_____	41
Figure 3.5 Schematic diagram of EHD setup on molten B <sub>2</sub> O <sub>3</sub> _____	43
Figure 3.6 Samples of B <sub>2</sub> O <sub>3</sub> strands as they appeared on the substrate _____	44
Figure 4.1 Concept of spark-stream technology_____	48

<i>Figure 4.2 a) Electron avalanche cascading toward the anode, b) electrons and ions flow in the discharge channel</i>	51
<i>Figure 4.3 Oscillatory behaviour of the voltage across the discharge [79]</i>	51
<i>Figure 4.4 Effect of pressure fluctuations on the micro-pools in the electrodes</i>	53
<i>Figure 4.5 The deflection of charged particles concept</i>	54
<i>Figure 5.1 Schematic diagram of spark-stream apparatus</i>	59
<i>Figure 5.2 Scanning electron microscope (SEM) graph of clusters of gold particles deposited on a carbon substrate</i>	60
<i>Figure 5.3 Clustering of particles following the electric field lines</i>	61
<i>Figure 5.4 TEM graphs of fine clusters of gold nanoparticles (scale bar 20nm)</i>	61
<i>Figure 5.5 a) (left) SEM graph of particles deposited from gold electrodes in air, and (right) EDX spectrum showing gold composition, b) (left) SEM graph of particles deposited from silicon electrodes in air, and (right) EDX spectrum showing silicon and oxygen composition, c) (left) SEM graph of particles deposited from zinc electrodes in air, and (right) EDX spectrum showing zinc and oxygen composition.</i>	62
<i>Figure 5.6 Electrical resistivity of tellurite glass made in-house (75%TeO<sub>2</sub> – 20%ZnO – 5%Na<sub>2</sub>O)</i>	64
<i>Figure 5.7 Spark-stream setup diagram for producing glass particles</i>	65
<i>Figure 5.8 SEM micrograph of tellurite glass particles generated by electrical discharge</i>	66

<i>Figure 5.9 SEM micrograph of spherical gold particles generated by the same spark-stream setup</i>	67
<i>Figure 5.10 SEM graph of a gold electrode after an experiment, where the tori appear surrounding craters</i>	68
<i>Figure 5.11 Schematic diagram of the substrate used for resistance measurment.</i>	71
<i>Figure 5.12 Resistance of gold nanoparticle deposition between two aluminium electrodes</i>	72
<i>Figure 5.13 Resistance of carbon thin film changes with time.</i>	74
<i>Figure 6.1 Electric field lines converging as a result of the voltage applied to the stainless tube.</i>	79
<i>Figure 6.2 Forces on similar charged particles moving under an applied electric field in air.</i>	80
<i>Figure 6.3 Distribution of Brownian particles due to diffusion in air.</i>	81
<i>Figure 6.4 FWHM of the distribution of Brownian particles increasing with time.</i>	82
<i>Figure 6.5 Particle drift due to charged particle interactions (60 elementary charges)</i>	84
<i>Figure 6.6 Effect of the initial separation on the final drift of a particle after 50ms in air and a charge of 60 elementary charges</i>	85
<i>Figure 6.7 Electric field configuration for transit time calculations</i>	87
<i>Figure 6.8 Transit time of nanoparticles with different diameters for a range of charge values</i>	88

<i>Figure 6.9 a) Deposition on substrate without using focussing tube. b) Deposition on substrate using focussing tube</i>	90
<i>Figure 6.10 Schematic diagram of the tube voltage analysis apparatus</i>	91
<i>Figure 6.11 Deposited spots using a) 400V focussing tube, b) 1200V focussing tube, c) 1800V focussing tube</i>	92
<i>Figure 6.12 Intensity profiles of deposited spot images for different tube voltages</i>	92
<i>Figure 6.13 FWHM of the deposited spots intensity profiles</i>	93
<i>Figure 6.14 Schematic diagram of transit time measurement apparatus</i>	95
<i>Figure 6.15 SEM graphs of the deposited gold nanoparticles on a pulse-synchronised spinning substrate.</i>	96
<i>Figure 6.16 Density of particles as a function of transit time.</i>	97
<i>Figure 6.17 Histogram of the elementary charges for each particle size.</i>	98
<i>Figure 6.18 Maximum charge of particles for different particle diameter.</i>	99
<i>Figure 6.19 Voltage across the capacitor as it charges and discharges.</i>	101
<i>Figure 6.20 The effect of the spark frequency on the deposition spot diameter.</i>	101
<i>Figure 6.21 The effect of the capacitor value on the spot diameter.</i>	103
<i>Figure 6.22 Effect of scaling down the focussing tube on the spot diameter</i>	104
<i>Figure 6.23 Gold deposition of parallel lines printed using a 0.5mm focussing tube with 350 V applied to it.</i>	105



Figure 6.24 a) pattern coordinates sent to the stages, b) pattern printed using a 0.5 mm ID focussing tube (1.5 mm long) with 500 V applied to it.	106
Figure 6.25 a) gold deposition using 0.35 mm ID focussing tube (~1.5 mm long), b) deposition using 0.21 mm focussing tube (~1 mm long), (100 $\mu\text{m}$ scale bars)	106
Figure 6.26 Copper nanoparticles are focussed inside photoresist PR pre-patterned mask from ref. [84] (scale bar is 1.5 $\mu\text{m}$ )	108
Figure 7.1 A comparison between the breakdown voltages for nitrogen, sulphur hexafluoride $\text{SF}_6$ and a mix of 1% of $\text{SF}_6$ with $\text{N}_2$ [108]	112
Figure 7.2 Paschen curve (—) and Field emission threshold (---) under ambient pressure are compared to Paschen curve (—) and Field emission threshold (---) at 10 kPa pressure for short gaps between the electrodes. Shaded area represents a potential experimental region.	113
Figure 7.3 Electric field calculated for the potential operating gaps at 10 kPa and at 100 kPa.	114
Figure 7.4 Illustration of the tube-ring focussing configuration	116
Figure 7.5 Schematic diagram of the tube-ring focussing configuration	117
Figure 7.6 Spot size comparison between single tube and tube-ring focussing configurations	118
Figure 7.7 Electric potential gradient and electric field lines of the ring-sequence focussing configuration	119
Figure 7.8 Spark-stream apparatus to produce bimetallic nanoparticles	120

*Figure 7.9 Setup for incorporating gold nanoparticles inside a glass fibre using the spark-stream technology concept*\_\_\_\_\_

122



# DECLARATION OF AUTHORSHIP

I, Ehab Saleh, declare that the thesis entitled “Direct write technologies for fabricating patterned metals and glasses” and the work presented in the thesis are both my own, and have been generated by me as the result of my own original research. I confirm that:

- this work was done wholly or mainly while in candidature for a research degree at this University;
- where any part of this thesis has previously been submitted for a degree or any other qualification at this University or any other institution, this has been clearly stated;
- where I have consulted the published work of others, this is always clearly attributed;
- where I have quoted from the work of others, the source is always given. With the exception of such quotations, this thesis is entirely my own work;
- I have acknowledged all main sources of help;
- where the thesis is based on work done by myself jointly with others, I have made clear exactly what was done by others and what I have contributed myself;
- parts of this work have been published as listed in the publications section.

Signed: .....

Date:.....



# Acknowledgements

I would like to express my great appreciation to various people in the University of Southampton and the Optoelectronics Research Centre (ORC) for their great support throughout the past years.

My deep gratitude to my supervisors Wei Loh, Will Stewart and Alun Vaughan for the great support and guidance they offered me during my research. I would like also to thank Matt Praeger, a research fellow in the group, for the great thoughtful discussions we had in the lab, and for his support in various theoretical and experimental aspects.

I wish also to thank Nick White for the enormous help he offered in the GlassJet lab, Xian Feng for making different glasses for the project, Allan Lian for the inspiring discussions we had, Dave Sager and Neil Sessions for all the help they gave in the clean-room facilities, the workshop team Mark, Ed and Paul for their generous support and indeed Trevor Austin for all the electrical advices he has given me.

Finally, my sincere gratitude to my beloved mom for her prayers that never stopped, to my wife, Huda, for the sweet encouragements and patience during my research, and to my family around the world.



# **Chapter 1**

## **1. Introduction to direct write technologies and motivations.**

### **1.1 Introduction**

Since its invention three decades ago, the success of inkjet printing proved direct write technologies to be a robust method to print polymer based inks and later other inorganic materials [1,2,3,4]. The flexibility of the direct write approach under ambient temperature and pressure conditions, and its ability to form different patterns on demand using the same apparatus make it very suitable for prototyping and manufacturing purposes.

For a direct write system to be used on a wide scale, robust and reliable technologies should drive it. A few techniques have emerged to demonstrate direct writing in the research and industrial sectors. Technologies like thermo-mechanical jetting using piezoelectric actuators [2,5], bubble jet inkjet printing [4,6], laser ablation [7,8,9] nanopen technology [10,11] and electrospraying/electrospinning technologies [12,13,14,15], all served the purpose of direct writing taking different routes to implement it.



In this chapter, the motivations for using direct write as a deposition method are introduced, and existing technologies on this subject are reviewed, followed by a comparison of the existing technologies, and their potential to serve the aims of this project.

## **1.2 Why direct writing of metals and glasses?**

The idea of direct writing of metals and glasses, and of being able to generate different geometries with minimal pre-processing and post-processing is an advantageous approach to speed up and improve rapid prototyping and manufacturing techniques. This flexibility in developing new designs provides the following benefits:

- Reducing the cost of research and development.
- Increasing the efficiency of new designs by enabling early error detection mechanisms.
- Allowing for fabricating patterns that are very challenging using conventional fabricating methods.

Many of the existing prototyping methods work only for a very limited class of the materials needed for electronic and optoelectronic purposes. Although it is sometimes possible to substitute materials by using the rapid-prototyped object as a mould, this is not very practical for refractory materials or small structures.

Being mask-free, direct writing has great flexibility in creating different patterns using computer aided design (CAD) software, with no need to implement any intrinsic physi-

cal change to the deposition apparatus. This means minimal pre-processing and post-processing of the work, resulting in faster and lower cost development processes.

The slow deposition rates of several existing physical vapour deposition (PVD) methods makes direct writing a competitive approach for depositing thick patterns and films. For example the Edwards BOC E500A e-beam evaporator used in the cleanroom at Southampton University has a deposition rate of 0.05nm/s - 0.1nm/s depending on the material. The Agar Gold Sputtering Coater gives a material deposition rate of around 0.1nm/s.

Assuming a PVD deposition rate of 0.1nm/s, to fabricate a simple ring shape film with a thickness of  $10\mu m$  as shown in Figure 1.1, the process would take 100,000s (more than 27 hours) not including the time taken for mask fabrication and machine preparation. Also in conventional lithography when the masks are removed all the material deposited on the masks will be wasted, which means that direct write has less material waste because it deposits material only at specific points on demand.

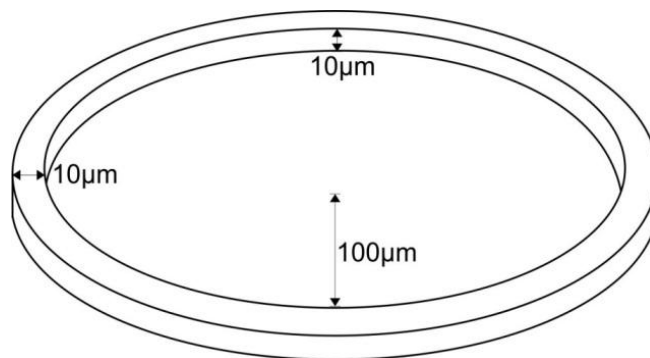


Figure 1.1 Ring pattern of  $10\mu m$  thickness

Direct write methods, electrospinning for instance, can deposit the complete pattern shown in Figure 1.1 at speeds ranging from less than 1 second up to 10 seconds for different systems [14,15].

This timescale comparison would have trade-offs with other parameters in the system, for instance, the surface roughness of PVD would be very small when compared with patterns printed using electrospinning for which the size of the smallest feature is in the order of 100nm. Also as PVD is capable of depositing large areas but with slow thickness build-up, if the pattern required is a large area, a thin film of 5nm thickness as an example, the deposition time required is less than a minute using PVD, and the film thickness is less than the smallest feature size of direct writing technologies, which makes the choice of a direct writing approach highly driven by the application.

### **1.3 Background on driving technologies**

A number of possible technologies that showed a potential to fulfil the aims of the project were reviewed. The likely performance of each technology was assessed against practical criteria driven by the aims of the project. The criteria include the ability to perform at high temperatures, produce high resolution patterns by generating micro-metre and sub-micrometre material deposition, inexpensive apparatus and applicability to a range of metals and glasses.

The following are the technologies that were considered:

- Thermo-Mechanical technology, which is based on melting the printing material in a reservoir and linking it to a nozzle where the liquid is mechanically forced out by applying high pressures using piezoelectric actuators [2,5,16,17].
- Bubble Jet mechanism, which uses a micro-heater inside the printing nozzle, and when an electric current is pulsed to the heater, the sudden rise in temperature vaporises the nearby component of the ink forming a bubble which ejects a droplet of the ink [6,18,19,4].
- Laser ablation, which uses short and high power laser pulses to focus intensive energy at a target material which is ablated onto a substrate [7,8,9].
- Nano-pen technology, where the printing material is liquefied and injected in a nano-pen, which is a nozzle similar to the one normally used in the thermo-mechanical technology, except it has sub-micrometre orifice diameter, and the liquid in nano-pen technology touches the substrate on leaving the nozzle in order to adhere to the substrate [10,11].
- ElectroHydroDynamic technologies (EHD), where a high electric field is applied to a liquid meniscus which causes instability of the liquid at the tip of the meniscus and leads to either spraying of the liquid for low viscosity liquids (known as electrospraying), or ejecting strands and fibres from the liquid meniscus for relatively high viscosity materials (known as electrospinning) [12] [13] [14] [15].
- Spark-Stream technology, this technology is developed as part of this project; it uses electrical discharge to generate nanoparticles from a very wide range of materials, and uses electrostatic techniques to focus down the nanoparticles to form deposition spots.

To evaluate the feasibility of these technologies, each technology is assessed under the criteria driven by the aims of the project, as shown in Table 1.1

Table 1.1 Evaluation of technologies reviewed

<b>Criteria Technology</b>	<b>Performance at high temperature</b>	<b>High resolu- tion</b>	<b>Inexpensive tools</b>	<b>Range of materials</b>
<b>Thermo-mechanical</b>	Moderate	Poor	Moderate	Moderate
<b>Bubble Jet</b>	Poor	Poor	Good	Poor
<b>Laser ablation</b>	Good	Good	Poor	Moderate
<b>Nano-Pen</b>	Moderate	Good	Moderate	Poor
<b>EHD</b>	Moderate	Good	Good	Poor
<b>Spark-Stream</b>	Good	Moderate	Good	Good

The rationale for this assessment is based on a number of factors for each technology summarised as:

- Thermo-Mechanical technology: Due to the surface tension of liquids, when high pressure is applied to push a liquid out of a nozzle, the surface tension of the liquid works against the pressure, which accumulates the liquid at the tip of the nozzle until the ejection force exceeds the surface tension of the liquid

where droplets leave the nozzle tip. As a result of that, in the case of using high surface tension liquids, molten solder or glass for instance, the smallest droplet diameter is approximately twice the orifice diameter [16], and fine droplets become very difficult to generate, so the resolution of the printing is low with average droplet diameter in the order of 50-150  $\mu\text{m}$  [20,21]. Also piezoelectric actuators are limited in operating temperatures, and for a thermo-mechanical approach using molten glasses at 500°C-1000°C, the printing task using piezoelectric actuators that could generate enough pressure thus becomes difficult.

- Bubble Jet mechanism: The fact that this technology requires vaporising the printing material in order to generate bubbles and force the liquid out of the nozzle makes it an unfeasible technology for materials like metals and glasses, which require very high temperatures in order to vaporise them.
- Laser ablation: The technology has good potential to fulfil some of the project's objectives, but the expensive laser equipment to form short pulses required for laser ablation leads to the search for other alternative technologies.
- Nano-pen technology: The fact that the nozzle tip is required to touch the substrate in order to wet its surface, makes the system very dependent on the surface properties of the substrate, where liquid-philic surfaces would be necessary for the wetting process to happen. This adds a limitation to the choice of materials that could be used in the printing process.
- ElectroHydroDynamic (EHD) technologies: One of the major advantages of EHD technologies is their ability to generate jets that are smaller than the nozzle size. As it will be described in chapter 2, the way EHD works is it initiates the jetting of material from the tip of the liquid meniscus. The challenge of EHD is

its dependence on the surface tension of the liquids. All reported work on EHD covers relatively low surface tension materials. This project investigates materials with higher surface tension values in comparison with all previously reported work, and it highlights the limits of EHD technologies at the materials range.

- Spark-Stream technology: The fact that spark-stream technology uses electrical discharge to generate nanoparticles makes the range of printing materials vast as will be described in later chapters. The stream of generated nanoparticles is focussed down one order of magnitude compared with the printing nozzle in air under ambient conditions, which is, like EHD, a major advantage of spark-stream technology.

This comparison between the strengths and weaknesses of each technology led to the adoption of EHD initially as a driving technology in this project. However, the limitations of EHD appeared at high surface tension materials, where applying a high electric field in air to overcome the surface tension of the liquids caused a breakdown of the surrounding air because of the high electric field, initiating an electric discharge and disturbing the EHD process. This appearance of an electrical discharge led to a further investigation of the electrical discharge phenomena, and highlighted their ability to erode materials and generate nanoparticles of a very wide range of materials. However, electrical discharge is a very violent erosion mechanism, where the generated nanoparticles scatter widely from the point of discharge, therefore electrostatic focussing techniques were introduced in order to make the stream of nanoparticles follow desired trajectories towards the substrate. This was done by studying the diffusion of nanoparticles in air, the inter-particle repulsion and the transit time of particles from the dis-

charge point to the substrate, to achieve a high level of focussing of the field-driven diffusing nanoparticles.





## **Chapter 2**

### **2. Electrohydrodynamic (EHD) technology**

#### **2.1 Introduction**

The ElectroHydroDynamic (EHD) technique has been in use since the time of Zeleny's successful attempt to eject liquid droplets in 1917 [22]. The concept behind EHD is to apply a high electric field to a liquid meniscus; if the field is high enough, it will eject liquid from the meniscus. The simple concept of the phenomena and its apparatus attracted many scientists to use it to produce sprays and fibres of many materials, including colloidal liquids [23,24,25] and polymers [26,27].

EHD direct write technologies, particularly electrospraying of low viscosity liquids [12,28,13] and electrospinning of relatively high viscosity liquids [29,27] have attracted a considerable interest because of their ability to produce jets and fibres with dimensions smaller than the printing nozzle [30,31].

The theory of EHD, as will be described in the next section, shows the important role of the surface tension of the liquid in initiating jets or strands from the tip of the liquid, where the surface tension of liquids works against the ejection force restricting EHD technology to relatively low surface tension liquids. Because of the high surface

tension values of molten ceramic and metals [32,33,34], different approaches are taken to the implementation of EHD on ceramics and metals. The use of suspended ceramic and metal particles in low surface tension liquids is a common approach to achieve implementing EHD with ceramics and metals [23,24,25], where the jetting of low surface tension liquids is used as a carrier of the ceramic and metal particles.

In this chapter the theory of electrohydrodynamic phenomena is introduced, the jetting conditions of liquids are discussed, and experimental details on jetting water droplets with colour additives is presented and analysed.

## **2.2 Theory of Electrohydrodynamic EHD phenomena**

The ejection of liquid droplets/fibres from a liquid meniscus in EHD is achieved by applying a high electric field to the meniscus. The mutual repulsion of the charges at the surface of the liquid meniscus and the applied field makes them migrate to and deform the surface into a tip. When the electric field force on the surface charges is higher than the surface tension force of the liquid a jet from the tip of the meniscus occurs.

The relatively strong electric field at the tip of the hemispherical liquid meniscus increases the electric field force at the tip, which elongates the liquid meniscus at the apex of the tip forming a cone shape of the liquid known as a Taylor cone [35]. This elongation enhances the electric field at the apex of the tip which in turn increases the effect of the electric field force until this force overcomes the surface tension of the liquid as shown in Figure 2.1.

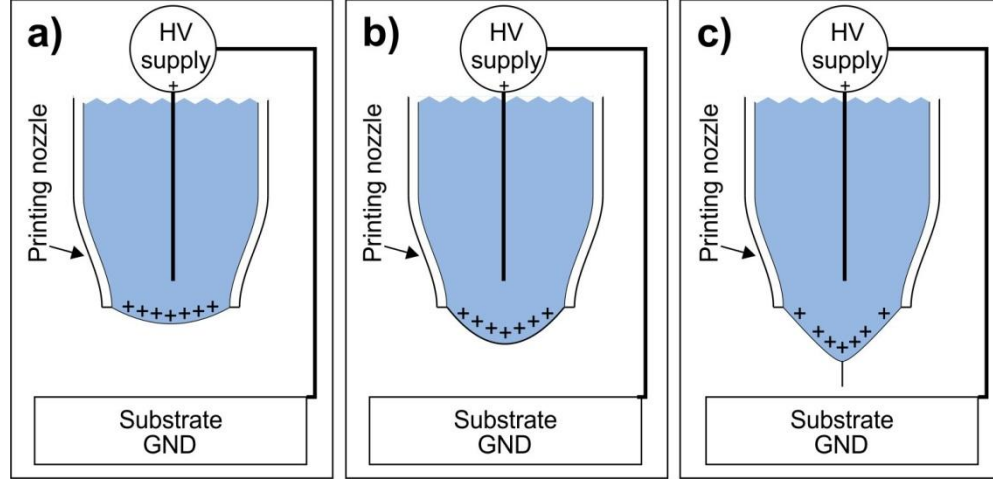


Figure 2.1 Charge accumulation at the tip of the meniscus.

The relationship between the bonding force on the surface of a liquid drop (surface tension) and the electric field force had been described by Rayleigh [36], who determined the maximum charge a liquid droplet can hold before it becomes unstable.

The experiments that Rayleigh conducted aimed to analyse capillary waves on liquids, in order to measure and analyse the angular frequency  $\omega_n$  of water droplets using a Laplace series, where the angular frequency relationship is:

$$\omega_n^2 = \frac{n(n-1)}{\rho r^3} \left[ (n+2)\gamma - \frac{Q^2}{16\epsilon_0\pi^2 r^3} \right] \dots\dots\dots (2.1)$$

where  $\rho$  is the density of the liquid,  $r$  is the radius of the droplet,  $\gamma$  is the surface tension,  $Q$  is the charge held in the droplet and  $\epsilon_0$  is the permittivity of free space.

Rayleigh observed that when  $(n+2)\gamma < (Q^2/16\epsilon_0\pi^2 r^3)$  the squared angular frequency would be negative, indicating instability. Rayleigh used the 2<sup>nd</sup> mode of the angular frequency to establish a charge limit as follows:

$$4\gamma = \frac{Q^2}{16\epsilon_0\pi^2 r^3} \dots\dots\dots (2.2)$$

$$Q^2 = 64\gamma\epsilon_0\pi^2r^3$$

$$Q_{ray} = 8\pi\sqrt{\gamma\epsilon_0r^3} \dots\dots (2.3)$$

This charge limit has subsequently been studied by other researchers, and experimentally it has been found that the charge limit is 70%-80 % of the limit that Rayleigh calculated [37,38,39].

The charge limit that Rayleigh introduced, and later assessed experimentally, could alternatively be derived by balancing the electrostatic pressure  $P_{ES}$  with the surface tension pressure  $P_T$  for a drop of liquid

$$P_{ES} = P_T \dots\dots (2.4)$$

The surface tension pressure is:

$$P_T = \frac{F_T}{A} \dots\dots (2.5)$$

In a drop of liquid, the surface tension force is:  $F_T = 2\pi r\gamma$ , and the surface area at the cross section of the drop is:  $A = \pi r^2$ , therefore equation 2.5 becomes:

$$P_T = \frac{2\pi r\gamma}{\pi r^2}$$

$$P_T = \frac{2\gamma}{r} \dots\dots (2.6)$$

The electrostatic pressure is the electrostatic force over the surface area of the sphere, and the electrostatic force is the product of the charge  $Q$  and the electric field  $E$ :

$$P_{ES} = \frac{EQ}{A} \dots\dots (2.7)$$

The surface charge density  $\sigma = \frac{Q}{A}$ , therefore equation 2.7 can be written as:

$$P_{ES} = E\sigma \dots\dots (2.8)$$

And the electric field derived from Gauss's law as a function of charge density as  $E = \frac{\sigma}{\epsilon_0}$  hence the electrostatic pressure equation 2.8 becomes:

$$P_{ES} = \frac{\sigma^2}{\epsilon_0} \dots\dots (2.9)$$

Substituting equations (2.9) and (2.6) in equation (2.4):

$$\frac{\sigma^2}{\epsilon_0} = \frac{2\gamma}{r} \dots\dots (2.10)$$

Since the surface charge density is  $\sigma = \frac{Q}{A}$  the left hand side of equation (2.10) could be manipulated to be:

$$\frac{\left(\frac{Q}{4\pi r^2}\right)^2}{\epsilon_0} = \frac{2\gamma}{r}$$

$$\frac{Q^2}{16\pi^2 \epsilon_0 r^4} = \frac{2\gamma}{r}$$

$$Q^2 = 32\pi^2 \epsilon_0 \gamma r^3$$

$$Q = 5.66\pi\sqrt{\gamma\epsilon_0}r^{3/2} \dots\dots (2.11)$$

This charge limit derived from the surface tension pressure and electrostatic pressure is 70.7% of the limit that Rayleigh calculated, and is closer to the critical charge for a liquid drop that was measured experimentally.

### 2.3 Onset voltage for liquid jetting against surface tension

As the surface tension of a liquid is the main force that counteracts the effect of the electric field, Table 2.1 shows the surface tension of different organic and inorganic liquids.

Table 2.1 Surface tension of some materials

Material	Surface tension (mN/m)
Methanol	23
Glycerol	64
Water	72
Molten Tellurite glass	150
Molten Indium	560

Since EHD is based on accumulating sufficient charge on the surface of a liquid meniscus in order initiate jetting, the electric potential required to provide this charge has to be determined.

Zeleny [22] used Rayleigh's equation to determine the onset voltage  $V_0$  required to initiate droplet ejection. Working in Centimetre-Gram-Second (C.G.S.) units, the Rayleigh

charge limit  $Q^2 = 16\pi\gamma r^3$  was substituted for the voltage as a function of charge ( $V=Q/r$ ) for different droplet geometries.

Zeleny found that the square of the onset voltage for droplet ejection is directly proportional to the product of the surface tension  $\gamma$  and the radius of the meniscus  $r$ .

$$V_o^2 = C\gamma r \dots\dots (2.12)$$

The constant  $C$  was measured empirically as shown in Table 2.2.

Table 2.2 Zelney's empirical results to determine the constant  $C$  [22]

Radius of point, 0.0250 cm. Average temperature, 23° C.				
Substance	Density	Surface tension	Instability potential	$C$
Acetone .....	0.790	24.9 dynes/cm.	9.30 electrostatic units	140
Methyl alcohol	0.804	25.3 "	9.25 "	137
Ethyl alcohol ...	0.812	25.3 "	9.25 "	137
Water .....	0.998	72.0 "	15.90 "	140
Acetic acid .....	1.053	30.0 "	9.67 "	125
Glycerine .....	1.259	65.2 "	15.17 "	142
Chloroform .....	1.483	27.0 "	10.17 "	153

Zeleny took the average value of the constant  $C$  from table Table 2.2 to be 140, and equation (2.12) therefore would be:

$$V_o^2 = 140\gamma r \dots\dots (2.13)$$

Writing equation (2.13) in  $SI$  units, and presenting the relationship between the onset voltage required to eject droplets and the surface tension of liquids shows an estimation of the voltage required to initiate liquid jetting:

$$V_o = 9.5 \times 10^5 \sqrt{\gamma r} \dots\dots (2.14)$$



Other recent studies presented various theories to calculate the onset voltage of liquid ejection. Results from Si [40,41] and Xiong [42] for the onset voltage are compared with the results that Zeleny calculated as shown in Figure 2.2. Equations from Si and Xiong are discussed in Appendix 1.

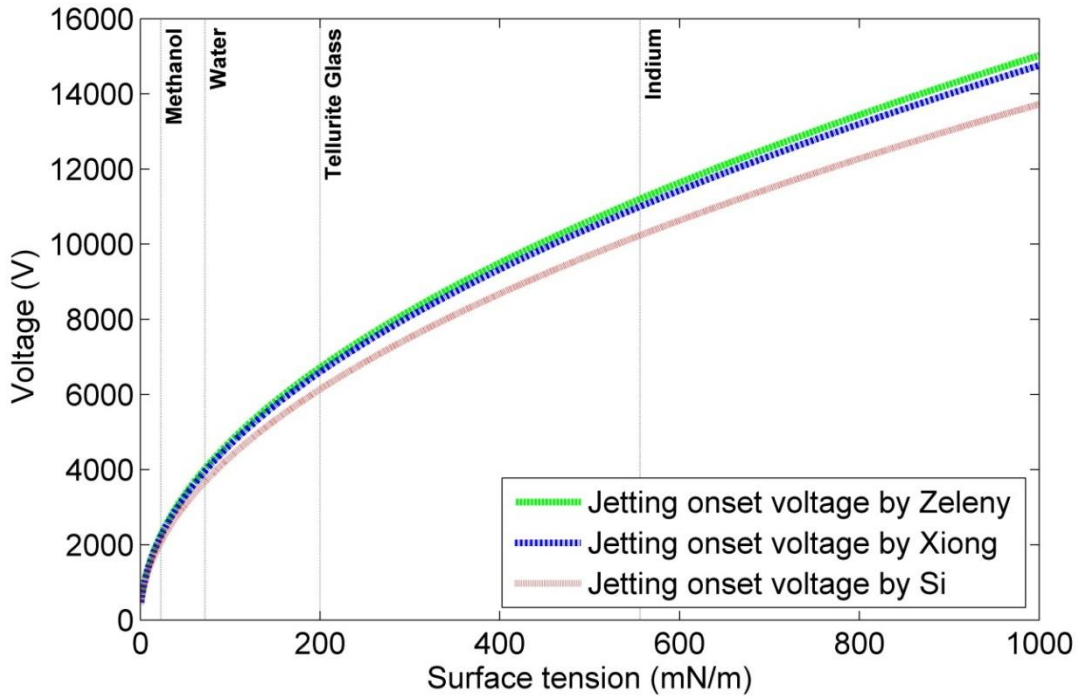


Figure 2.2 Onset instability voltage with surface tension of some materials for a 250  $\mu m$  meniscus radius.

## 2.4 EHD experiments on water

Water has one of the highest surface tension values for room temperature liquids, and the voltage required to eject water droplets using EHD in air under ambient conditions is close to the breakdown threshold of air [43,44,45]. In fact, most of the studies on

EHD use liquids that have surface tension values lower than water in order to avoid operating at voltages close to the electrical discharge voltage.

However, as the aim of this research is to jet glasses and metals, experiments on a high surface tension liquid like water highlight the EHD challenge for glasses and metals, whilst allowing experience with the EHD process and with the high voltage supply system in less challenging conditions of temperature and pressure than would be needed for molten glasses.

#### 2.4.1 EHD water experiment apparatus

The apparatus used to eject water droplets using EHD technology was built in-house, where a high voltage (HV) supply is connected to a nozzle filled with coloured water as shown in Figure 2.3. The HV source in this setup is acting as an amplifier driven by a signal generator to form HV pulses. The nozzle is a fused silica tapered capillary made in-house, and the colouring additive is food dye.

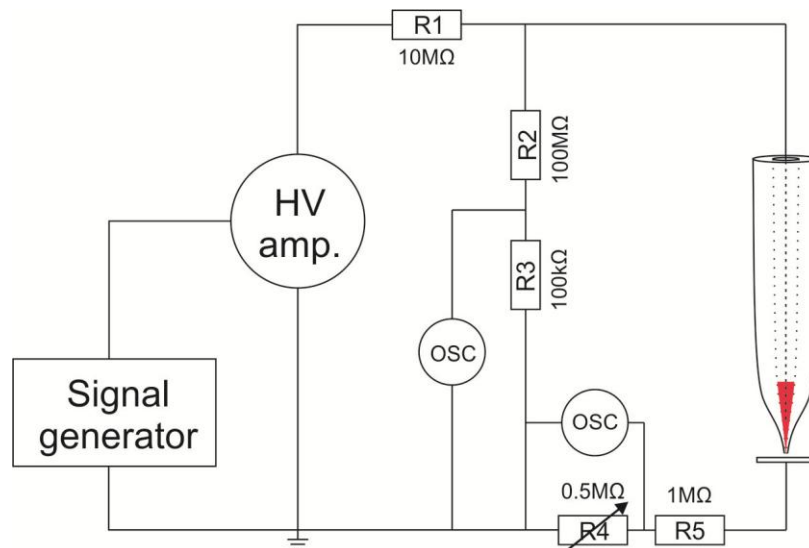


Figure 2.3 Schematic diagram of EHD setup to electrospray water

The high voltage source (in this setup 4kV dc/dc convertor-C40 from EMCO HV CO.) is connected in series with a resistor R1 which works as a current limiter to protect the supply, so even if the rest of the circuit is shorted, i.e. discharge occurs, the current drawn should not exceed the voltage divided by the value of this resistor. Resistors R2 and R3 act as a potential divider to scale down the voltage supplied by a factor of 1000, so an oscilloscope can be connected safely to monitor the voltage supplied to the liquid.

When liquid ejects from the meniscus, it carries a charge [28,46]. In this setup this charge is used to record the occurrence of droplets, where resistors R4/R5 are a potential divider to monitor the pulses generated by the arrival of droplets on the conductive aluminium substrate.

The first phase of experiments conducted using this setup aimed at determining the ability to implement EHD on water under ambient conditions. The following phase aimed to monitor the droplets occurrence. Figure 2.4 shows an example of dyed water droplet that was printed using this setup as well as the voltage pulse across R4 which occurs when droplets arrive at the substrate and unload their charge. The internal diameter of the capillary nozzle was  $50\text{ }\mu\text{m}$ , voltage supplied was 1100 V and the gap between the tip of the nozzle and the substrate was  $150\text{ }\mu\text{m}$ . The first pulse shown in Figure 2.4 is due to the internal capacitance of the circuit, where a small amount of current passes through the resistor R4 towards the ground. This pulse appears whenever the voltage is first supplied to the circuit even if no liquid ejection occurs.

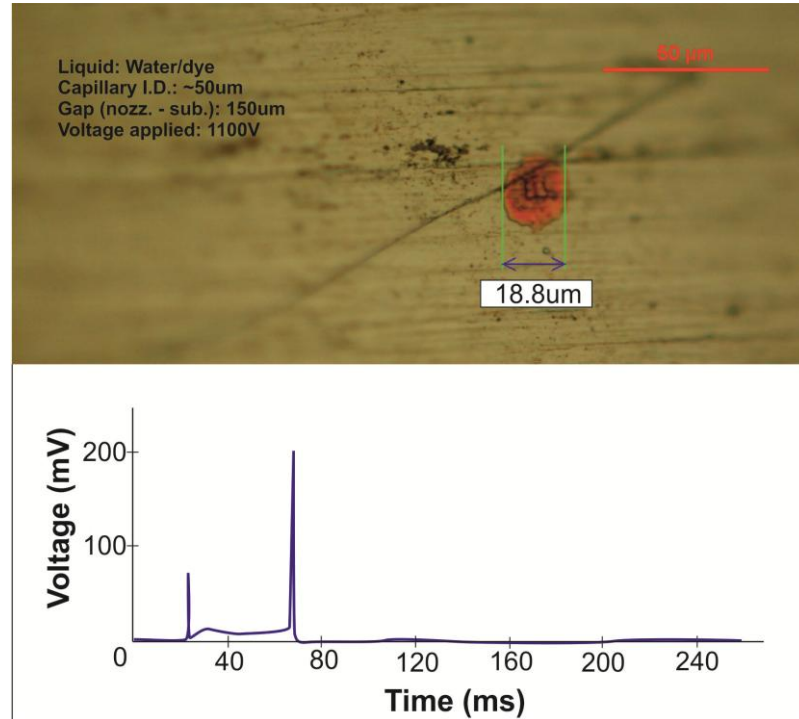


Figure 2.4 A deposited droplet associated with a pulse generated on the substrate

Using this setup, it was proved that an ejection of water droplets, where water has relatively high surface tension, is still possible under ambient conditions.

#### 2.4.2 Frequency analysis of liquid ejection

When the charged droplets eject from the liquid meniscus, they reduce the overall charge on the liquid meniscus. This halts the ejection until the charge again builds up to a sufficient value to initiate ejection. This oscillatory behaviour was analysed in order to study the ejection rate of droplets, which is an important parameter for the speed of printing.

Applying a H.V DC generates a series of voltage pulses on the substrate once droplets arrive. However, it was noticed that the pulse occurrence frequency declines with time, so an analysis of this behaviour was necessary.

Pulses were divided into groups 1- 6 as shown in Figure 2.5a below the current waveform, and a Fourier transform was applied to each group to observe the behaviour of the frequency over time. Figure 2.5 shows the waveform of the pulses used in the frequency analysis, and an example of the frequency analysis of the pulses in group 1.

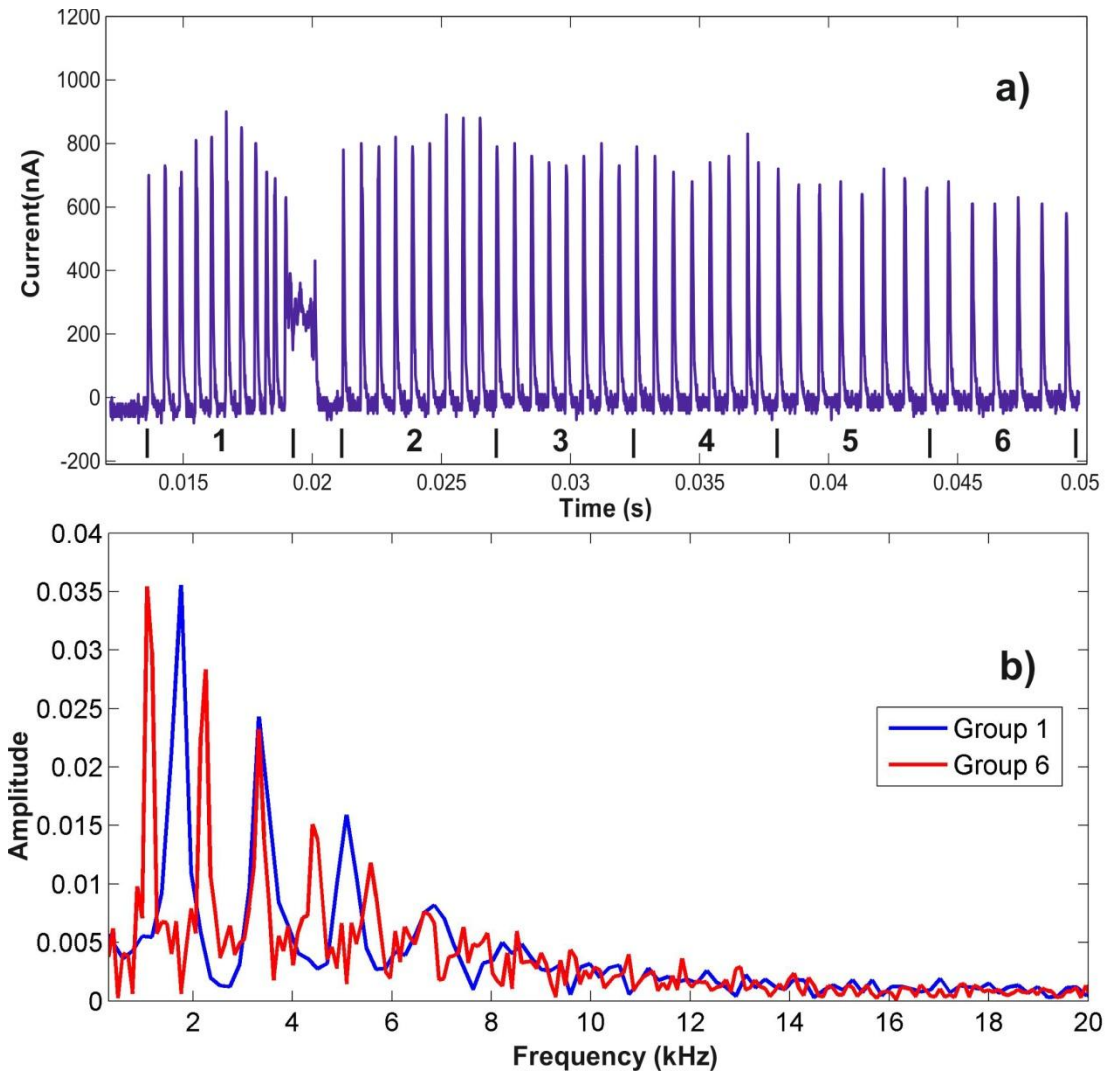


Figure 2.5 a) Current waveform labelled to groups 1 to 6, b) frequency spectrum of groups 1 and 6 of the current waveform

A summary of the frequency analysis is shown in Figure 2.6. The frequency drops with time which was determined to be a result of the decline in the volume of liquid in the meniscus as the droplets eject from it. Therefore, a method to maintain the volume of liquid was found to be necessary.

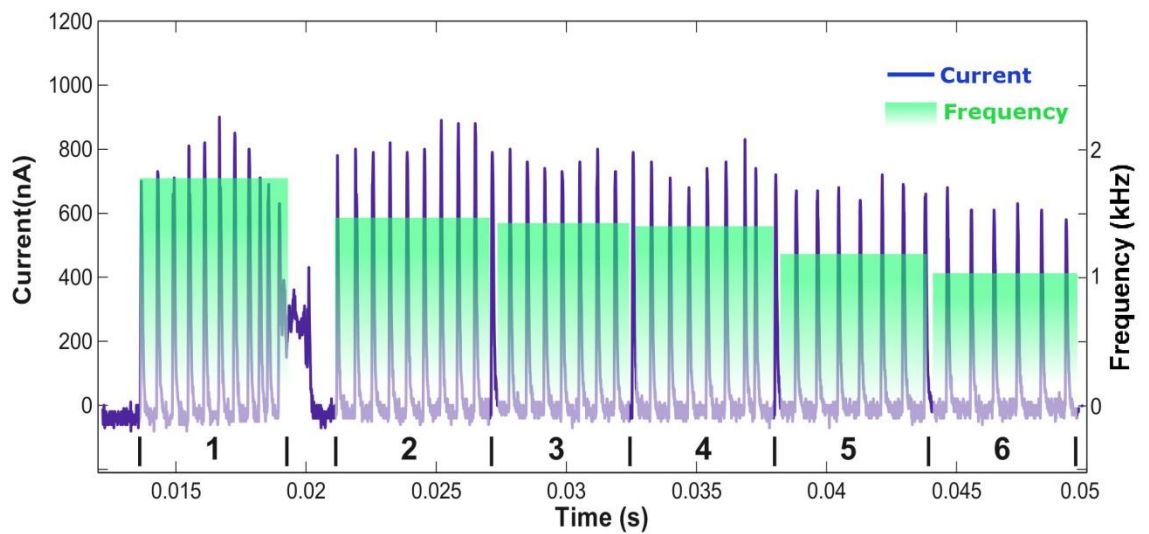


Figure 2.6 Frequency analysis of the current pulses waveform showing frequency decline with time

### 2.4.3 Pressure control

A pressure control system was considered as a method to control the volume and shape of the meniscus. However, ahead of designing a pressure control system, the range of pressure required should be theoretically calculated so the pressure parameters in the system could be estimated.

The pressure due to surface tension in a spherical liquid droplet  $P_T$  can be derived from the surface tension of the liquid as shown in equation (2.6) in section (2.2) :  $P_T = \frac{2\gamma}{r}$  . However, the pressure of a liquid meniscus protruding from a tip of a capillary follows the ratio  $(\theta/2\pi)$  as shown in Figure 2.7.

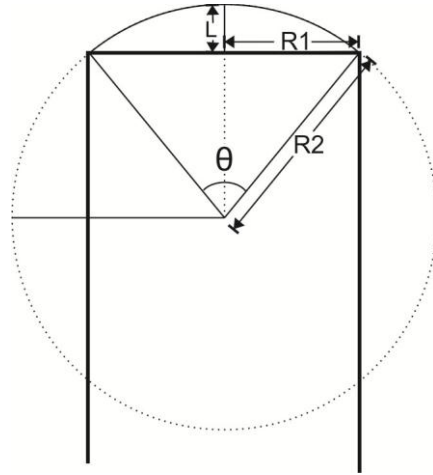


Figure 2.7 Pressure analysis graph

The pressure in the meniscus ( $P_m$ ) equals the pressure in a droplet  $P_T$  multiplied by the ratio  $(\theta/2\pi)$ , where the radius of the droplet from Figure 2.7 is  $R_2$ .

$$P_m = \frac{\gamma}{R_2} \frac{\theta}{\pi} \dots\dots\dots (2.15)$$

The value of the angle  $(\theta/2)$  is the inverse sine of the capillary radius  $R_1$  over the radius of curvature  $R_2$ , so:  $\theta = 2 \sin^{-1} \left( \frac{R_1}{R_2} \right)$ . So the pressure in the meniscus is:

$$P_m = \frac{2\gamma \sin^{-1} \left( \frac{R_1}{R_2} \right)}{\pi R_2} \dots\dots\dots (2.16)$$

where the radius of curvature  $R_2$  can be calculated as:  $R_2^2 = R_1^2 + (R_2 - L)^2$ , hence  $R_2 = (R_1^2 + L^2)/2L$  . Using equation (2.16) for water in a tapered capillary with 260um radius, a pressure was applied to the liquid in the capillary from a syringe pump, and

the extension  $L$  shown in Figure 2.7 was measured as the pressure increases in comparison with the room pressure which defines the pressure difference shown in Figure 2.8 below.

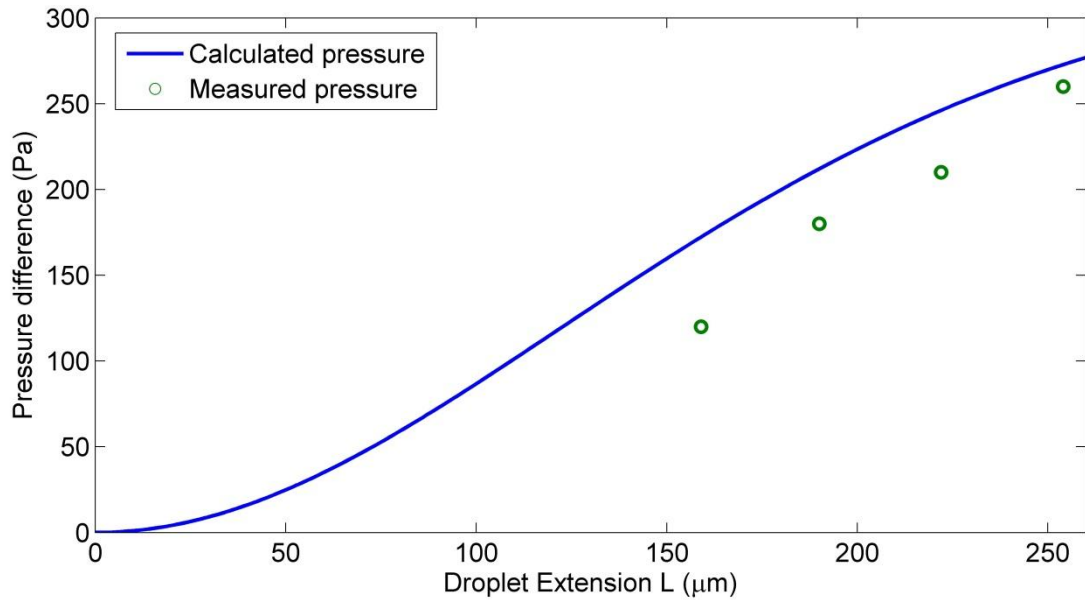


Figure 2.8 Theoretical calculations and empirical measurements of the pressure as it changes with the extension of the meniscus  $L$

The pressure range expected in these parameters was 0-300 Pa above the atmospheric pressure as shown in Figure 2.8. To confirm these results empirically, a commercial pressure sensor was used. Using a differential pressure sensor (MPXV7002) from Free-scale, the pressure sensor gave results in the order of 25% below the calculated pressure values. This could be due to pressure leakage in the experiment which caused the pressure difference.



As the pressure range is estimated, a pressure control system was implemented on the setup to maintain the shape of the meniscus using a closed-loop feedback control system between the pressure sensor and the syringe pump as shown in Figure 2.9.

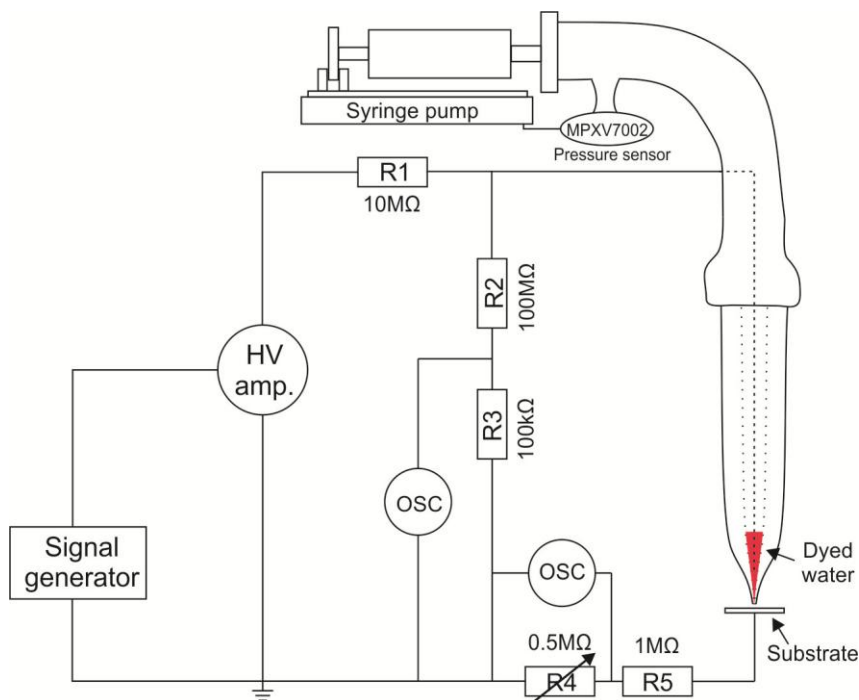


Figure 2.9 EHD apparatus with pressure control system to maintain the shape of the liquid meniscus

#### 2.4.4 Droplet on demand

The pressure control system described in section 2.4.3 maintains the stability of the meniscus. However, in order to print droplets on demand in a well-defined manner the gap between the tip of the meniscus and the substrate should be small. Bringing the substrate close to the meniscus will enable the droplets to be collected as they leave the tip of the jetting meniscus before they are scattered due to charge repulsion. Figure 2.10 shows the spots appearing on the substrate, and the voltage applied to eject

those droplets as well as the pulses appearing on the substrate via the oscilloscope channel across the resistor R4.

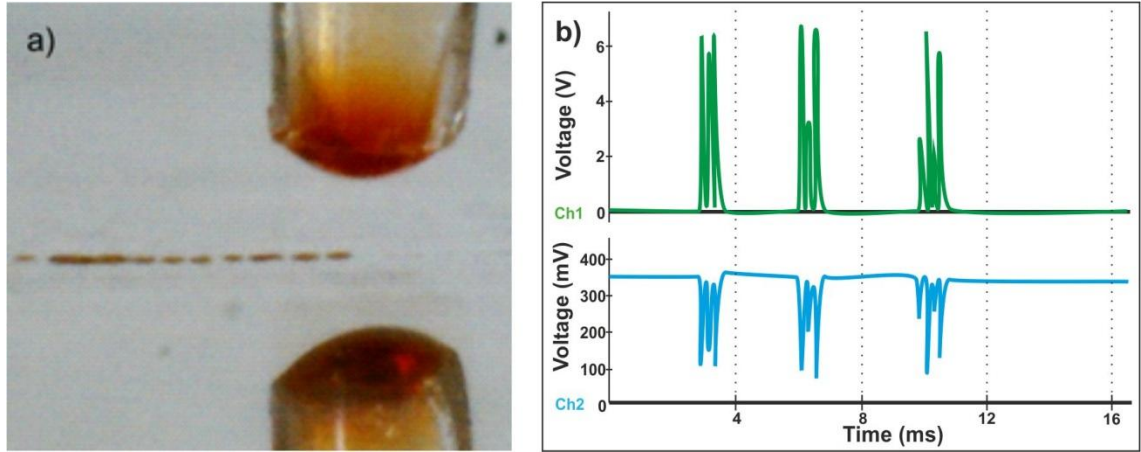


Figure 2.10 a) line of spots appears while printing, b) channel 2 (blue line) is HV pulse line and channel 1 (green line) is the pulses generated from each droplet at the substrate.

The process that printed the line in Figure 2.10 involved applying a pulse of high voltage, observing the droplet occurrence, and then moving the substrate using one axis of the translation stage. The onset voltage to eject droplets as it appears in Figure 2.10b is 350V (blue line - the graph shows the peak of the much longer pulse which looks like a DC voltage for this oscilloscope setting). Looking at channel 2 (blue line), the voltage drop from 350V to 100V suggests that a very low resistance medium appears in the gap at the time of droplet ejection. Comparing that observation with the strategy of bringing the substrate close to the meniscus so the droplets are collected as soon as they leave the parent meniscus, the very end tip of the jet seems to touch the substrate which causes the voltage drop across the gap.

On the same figure, pulses appearing on the green line are associated with a single high voltage pulse applied to the liquid, so it seems that each HV pulse generates more than one pulse on the substrate, or it is actually more than one droplet descending on the substrate in a very short time that the 30fps camera could not resolve.

In order to verify the relationship between droplet accumulation on each spot and the pulses that appear on the substrate line, high speed camera verification was required.

A RedLake HG-100K high speed camera was used. To provide sufficient lighting a high power LED was used to transmit light through the meniscus. Another lighting configuration was also used at high frame rates of 5000 fps using a 100mW 550nm CW laser configured to reflect light from the meniscus. The apparatus was constructed as shown in figure 3.14. Frame rates were varied starting from 250fps up to 5000 fps; the reflected/transmitted light was hardly visible to the camera at frame rates higher than 5000 fps.

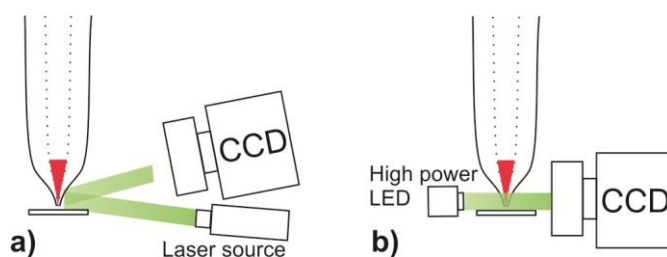


Figure 2.11 High-speed camera setups, a) using laser beam reflecting from the meniscus, b) using high power LED transmitting light through the meniscus

The camera trigger was synchronised with the H.V. source, such that the camera starts recording as soon as the H.V. pulse is initiated. At 2000fps, images could be taken with sufficient lighting, showing the jet cones as they appear in Figure 2.12.

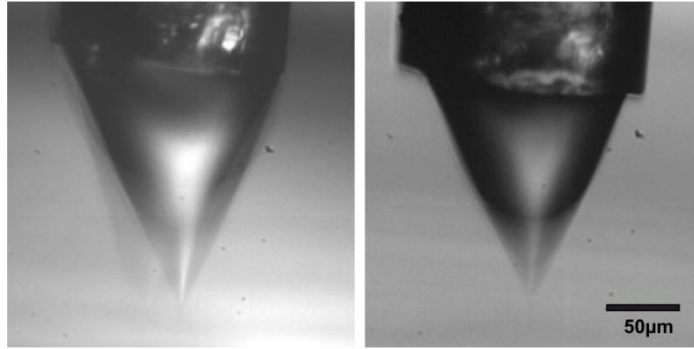


Figure 2.12 Samples of jet cone images taken at 2000fps

The formation of the cone accelerates after the HV pulse is turned on, which agrees with the physical analysis mentioned before, where the accumulation of charge speeds up the cone formation. This explains the shadowy shape at the tip of the cone where the speed of the camera is not sufficient to capture that moment of the image.

Answering the main question of whether we have one droplet or many in each HV pulse was achieved by synchronising the voltage pulses appearing on the substrate with the images taken at 2000fps, see Figure 2.13.

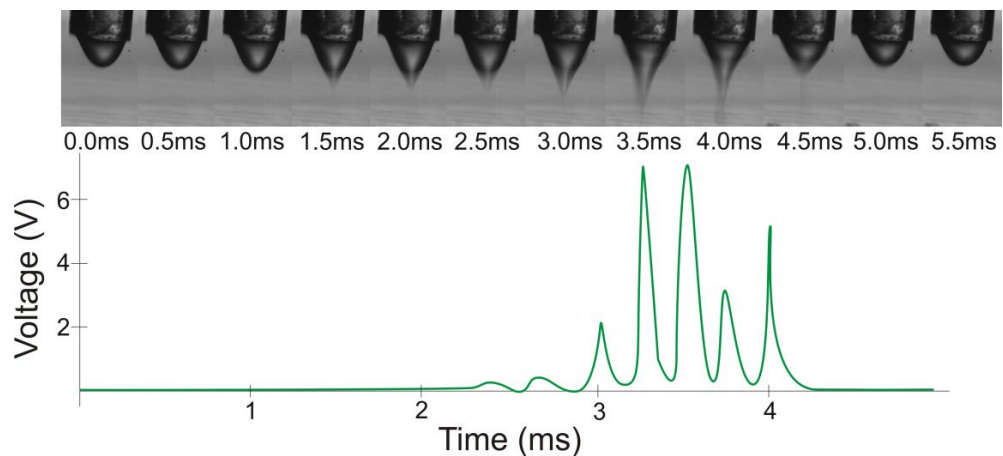


Figure 2.13 High-speed camera images synchronised with the voltage oscillations appearing on the oscilloscope

Comparing that to another sample, where three groups of oscillations appear on the oscilloscope, and synchronising it with the images associated with it, three ejections can be seen in the images associated with the oscillations as shown in Figure 2.14.

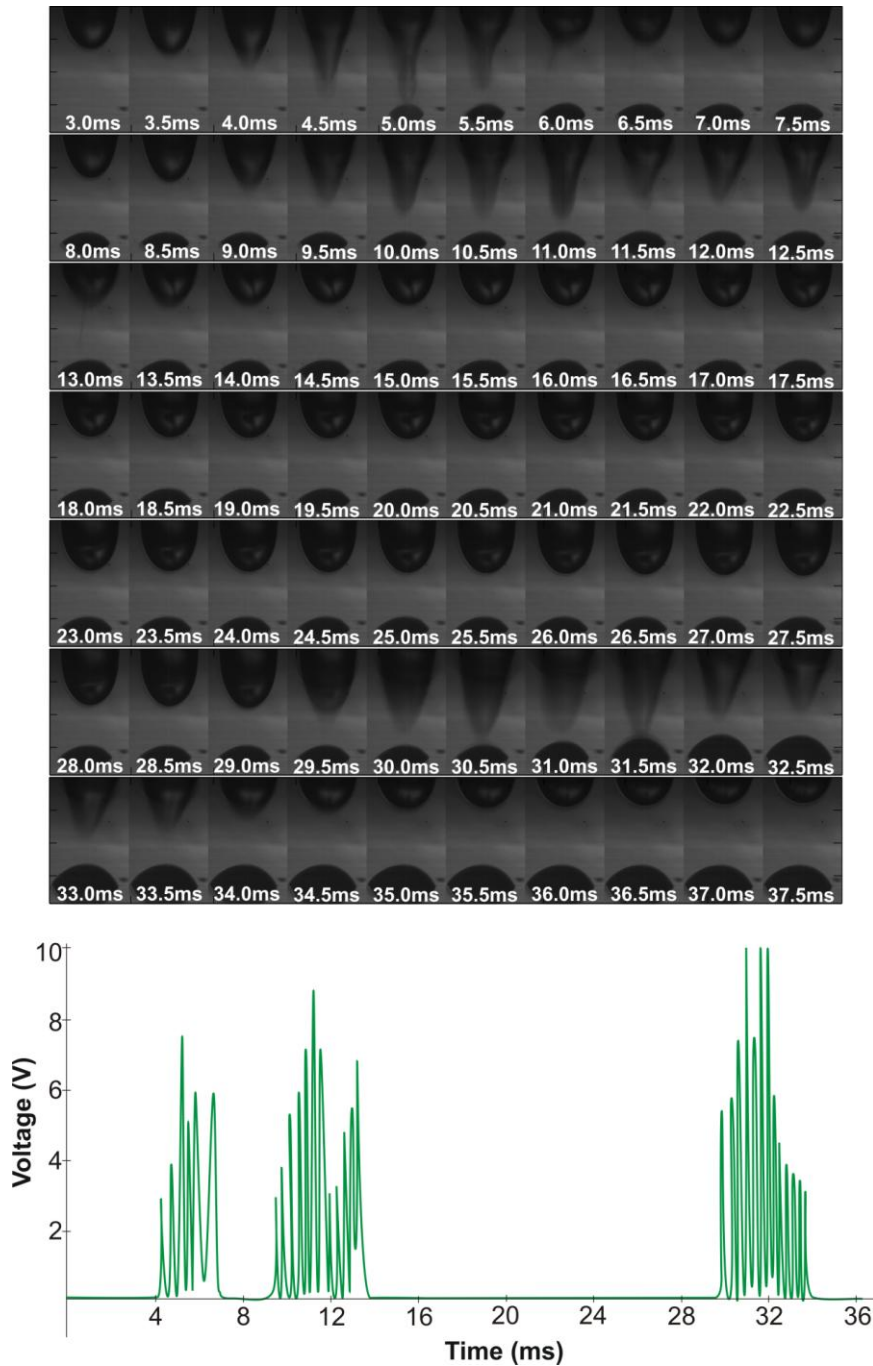


Figure 2.14 Three ejections appear in images taken at 2000fps synchronised with the pulses associated with their arrival to the substrate

From these sets of experiments using the high speed camera, the multi-ejection in each spot can be observed, and this demonstrates that the spots deposited in our configuration are a result of multi-droplet accumulation on one position. In order to form single ejection on demand shorter pulses are required, which was not available using the HV supply in these experiments (the maximum slew rate of EMCO HV DC/DC converter is 10 V/ms).

## **2.5 Conclusion**

Electrohydrodynamic phenomena have been studied throughout the chapter, starting from the theory of jetting up to demonstrating water ejection using an apparatus built in-house.

The accumulation of charge on a liquid meniscus as a result of applying a high electric field has been analysed theoretically by studying the charge limit (Rayleigh limit) and the voltage required to initiate liquid ejection (onset voltage). Comparing the ejection onset voltage to the surface tension of materials, water was chosen to analyse the EHD phenomena experimentally due to its high surface tension compared to other room temperature liquids.

An EHD water jet apparatus was built with a pressure control system to maintain the water meniscus shape as the material is ejected. Droplet ejection was monitored using the charge released as the droplets arrived at the substrate. High speed camera images

were also used to trace the ejections as they occurred, where multi-droplet ejection appears to form each deposited spot on the substrate.

As the principles of jetting liquid using EHD have been studied and demonstrated, other materials could be used following the same concept and experience gained from the work done in this chapter.

## **Chapter 3**

### **3. Jetting glass strands using Electrohydrodynamic (EHD) technology**

#### **3.1 Introduction**

Having conducted EHD successfully on water as discussed in chapter 2, this chapter describes work aimed at applying EHD phenomena to higher surface tension materials than water.

EHD was first studied theoretically and experimentally using water in order to gain a better understanding of the technology, which should be useful when extending experiments to molten high surface tension materials.

Knowing that surface tension is one of the major challenging parameters expected in conducting EHD experiments on glasses and metals, a survey of the surface tension of these materials was made. From the surface tension survey, glasses exhibit lower surface tension values than metals, therefore glasses were investigated and experiments were conducted on borate glass  $B_2O_3$  owing to its low surface tension value of around 10% above the surface tension of water.



Since the experiments were on molten glass, the electrical discharge issue was reviewed in a hot environment, and different methods to operate at high breakdown threshold values in air were considered.

The study of the conditions related to conducting the experiment led to successfully implementing EHD on molten  $B_2O_3$  in air, where glass strands of 100nm diameter were ejected from the apex of the glass melt.

### **3.2 Surface tension of glasses and metals**

Liquids that have high surface tension are expected to require a high applied voltage in order to eject material from the surface of the liquid meniscus. If the surface tension of a liquid is too high, an electrical discharge due to breakdown of air appears prior to any droplet ejection. Therefore the aim of this chapter is to assess the highest surface tension value that allows EHD experiments to be successfully conducted in air at atmospheric pressure.

The surface tension of molten metals is generally very high, as shown in Table 3.1, in comparison with room temperature liquids such as water, which has a surface tension value of 72 mN/m.

Table 3.1 Surface tension of molten metals [34,47,48]

<b>Metal</b>	<b>Surface tension (mN/m)</b>
Lead (Pb)	460
Indium (In)	560
Zinc (Zn)	790
Silver (Ag)	925
Gold (Au)	1100

Initial experiments were conducted on molten indium to assess the possibility of implementing EHD on molten metals in air. During these experiments an electrical discharge appeared before any deformation of the meniscus of molten indium, although indium has one of the lowest surface tension values of molten metals. This led to a search for materials other than metals which have lower surface tension, but still higher surface tensions than water to investigate the behaviour at intermediate values.

Glasses exhibit a wide range of properties, including surface tension, based on the glass composition. The search for “low” surface tension molten glasses, after observing that silicate glasses exhibit high surface tension as shown in Table 3.2 [49], suggested that very different glasses may be needed.

Table 3.2 Surface tension of some silicate glasses. S1, A5, A6 and A7 are different silicate glass compositions [49]

<b>Glass type</b> <b>Material</b>	<b>A5</b>	<b>A6</b>	<b>A7</b>	<b>S1</b>
SiO <sub>2</sub> %	72.4	71.5	71.5	40.9
Na <sub>2</sub> O %	13.3	8.5	12.9	15.3
K <sub>2</sub> O %	0	3.3	0	4.5
CaO %	9.2	13.5	12.0	8.4
MgO %	3.4	0.1	2.5	0
B <sub>2</sub> O <sub>3</sub> %	0	0	0	17.5
Al <sub>2</sub> O <sub>3</sub> %	1.1	0.2	0.2	7.7
Fe %	0	0	0	3.5
CoO %	0	0	0	0.6
Temperature (°C)	900	900	900	750
Surface tension (mN/m)	334	312	344	262

Another glass former that shows the potential to have low surface tension is boron trioxide B<sub>2</sub>O<sub>3</sub>. In fact, borate glasses generally have relatively low surface tension when compared with all other glasses [50,51].

Figure 3.1 shows different borate glass compositions and their surface tension as a function of temperature [51]. Boron trioxide as a glass former has a surface tension

range of 83-90 mN/m at 1120 – 1370 K which is much closer to the surface tension of water than that of other glasses.

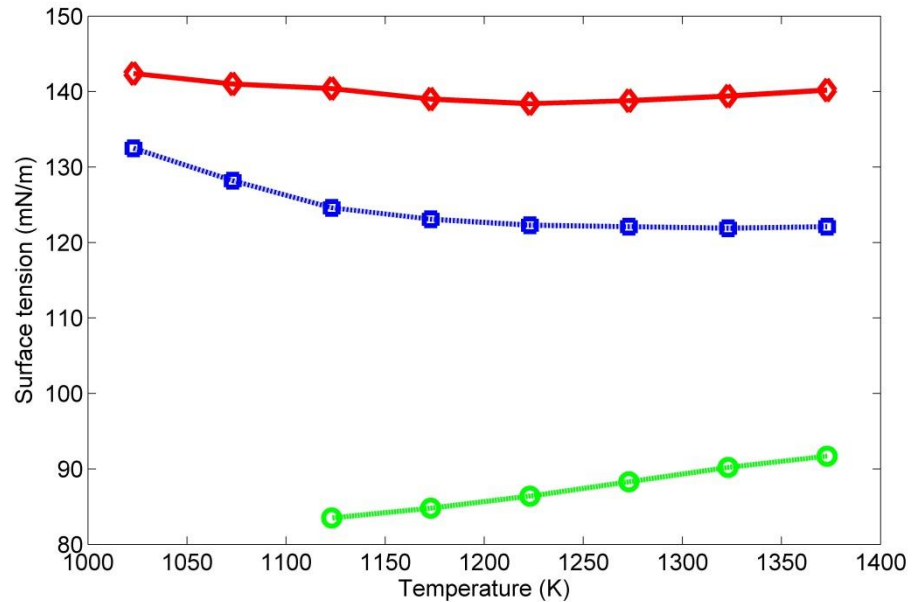


Figure 3.1 Surface tension of some borate glasses from [51], mol%: ○ = 100%B<sub>2</sub>O<sub>3</sub>, □ = 70%B<sub>2</sub>O<sub>3</sub>-30%PbO, ◇ = 70%B<sub>2</sub>O<sub>3</sub> - 30%Bi<sub>2</sub>O<sub>3</sub>,

Borate glasses have a variety of applications, particularly in medicine as a bioactive material [52,53,54]. Borate glass medical applications include wound healing [52] and bone tissue scaffolding [53,54].

Due to its variety of applications, and its low surface tension, boron trioxide was chosen, and depending on the experimental results other borate glasses may also be used.

### 3.3 Effect of temperature and separation gap on the electrical discharge

The concept of implementing EHD on borate glass is similar to the one used for ejecting water droplets, except for the use of high temperature. In order to keep the borate glass molten, the tapered capillary is surrounded by a heating element.

Due to the use of high temperatures, a possible concern is highlighted that the breakdown threshold of air at ambient pressure decreases when the temperature is increased.

Figure 3.2 contains experimental data and theoretical results showing the breakdown threshold of air and its variation with temperature [55].

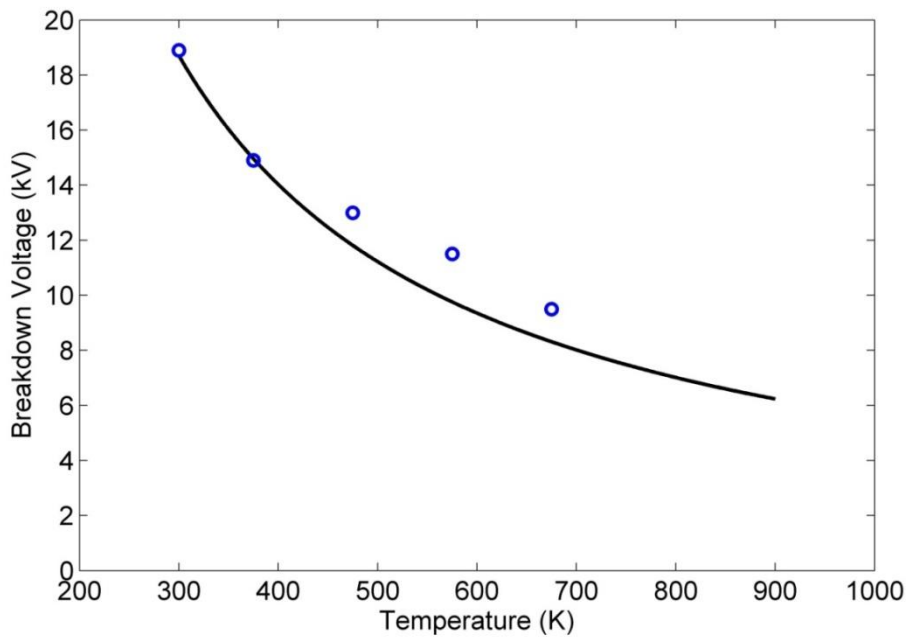


Figure 3.2 The breakdown threshold of air changes with temperature. Circles represent empirical results, and the solid black line represents theoretical results of the breakdown voltage ( $V = V_0 \frac{T_r}{T_g}$ ) where  $V_0$  is the breakdown threshold of the gas at room temperature,  $T_r$  is the room temperature in K and  $T_g$  gas temperature in K [55]

So care is required to avoid reaching the breakdown threshold of air while conducting experiments on molten glass. The aim is to operate at electric field levels that are sufficient to cause material ejection of glass just as was done with water but not to initiate electrical discharge.

The breakdown threshold of air at room temperature, as described by the Paschen curve, changes with the product of pressure and the air separation gap between the electrodes. The relationship between the pressure-gap product and the breakdown voltage threshold  $V_B$  of air can be calculated as follows [56,57]:

$$V_B = \frac{B (pd)}{\ln(pd) + \ln\left(\frac{A}{\ln\left(1 + \frac{1}{\gamma_i}\right)}\right)} \dots\dots\dots (3.1)$$

where  $p$  is the pressure of the gas,  $d$  is the gap distance between the electrodes,  $A$  and  $B$  are the Paschen curve coefficients (measured empirically) and  $\gamma_i$  is Townsend coefficient described further in Appendix 2.

Under atmospheric pressure, the Paschen curve can be used to calculate the breakdown threshold of air against the gap between the electrodes, as shown in Figure 3.3 for flat a anode and spherical cathode [58,59,60].

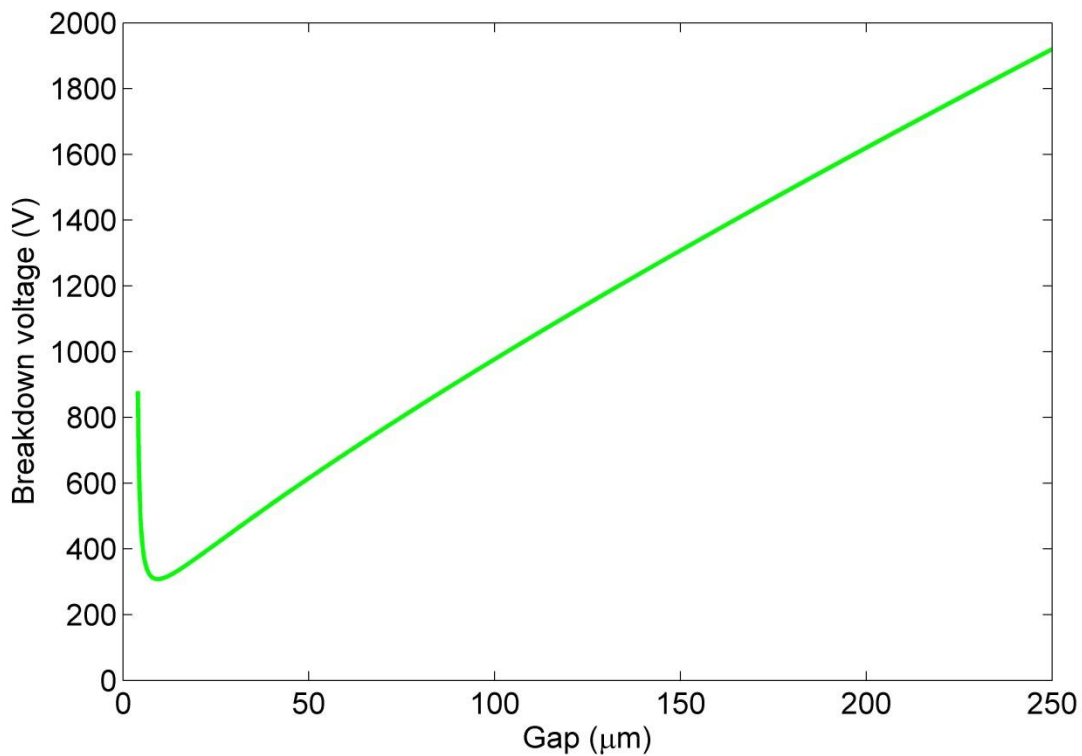


Figure 3.3 Paschen curve showing the relationship between the breakdown voltage of air at atmospheric pressure and the gap between the electrodes

Initially the breakdown voltage from the Paschen curve falls almost linearly with the gap between the electrodes until the gap is below  $10\ \mu m$ . This suggests a possible region of operation, allowing for high voltages to be applied to smaller gaps, as the electric field ( $E = \text{Voltage}/\text{gap}$ ) would be higher at this region in comparison with the region of the curve above  $10\ \mu m$ .

However, the Paschen curve has been revised by previous work, and the region of the curve below  $10\ \mu m$  electrode spacing has been studied in detail theoretically and experimentally [61,58,62,63]. The reason for preventing the discharge despite of the high electric field at this short distance is because in the very short distance between

the electrodes the number of electron collisions is not sufficient to form an avalanche. So the mechanism for electron transport in this region is different from the mechanism in the region above  $10\ \mu\text{m}$  in air at atmospheric pressure. Instead of an electron avalanche, field emission occurs in this region and electron emission in the form of electron leakage between the electrodes takes place due to the presence of a very high electric field in a continuous manner rather than as a catastrophic avalanche [63,62]. Figure 3.4 shows the field emission threshold as compared to the Paschen curve at short gaps between the electrodes [61,59,57]. Further details of the field emission equations are given in Appendix 2.

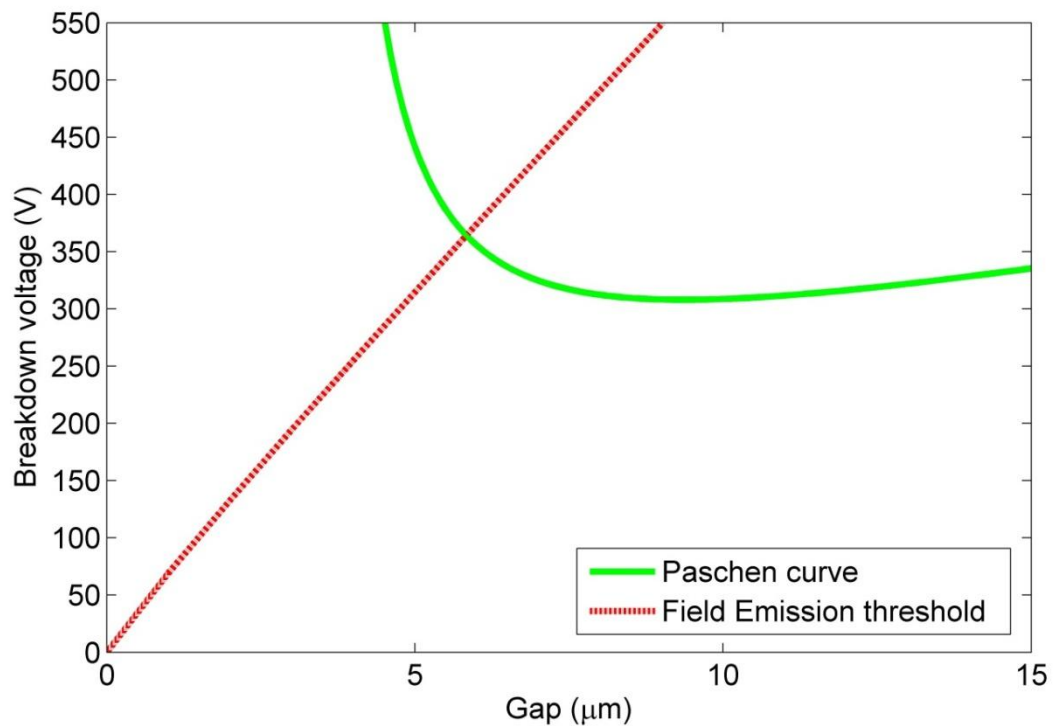


Figure 3.4 Paschen curve and Field emission threshold at short gaps between the electrodes



The comparison between the Paschen curve and the field emission region shows that the breakdown voltage in the region between  $5\ \mu\text{m}$  and  $15\ \mu\text{m}$  is almost constant in air at atmospheric pressure. In that region the electric field value will be very high as the voltage is constant but the gap is narrow. Although electron emission occurs between the electrodes, in this region EHD could potentially be implemented due to the very high electric field even though some current leakage will occur. Therefore operating EHD at small gaps was identified as a potential approach for conducting the experiments on glass.

### 3.4 Experiments on borate glass

Having shown a potential to implement EHD using boron trioxide ( $\text{B}_2\text{O}_3$ ), the material was bought from Sigma-Aldrich (purity 99.98%). The work in this section was conducted by Dr Matt Praeger, a research fellow in the project, who conducted the experiments on  $\text{B}_2\text{O}_3$ . Initial experiments on molten borate glass ( $\text{B}_2\text{O}_3$ ) showed that, although the surface tension of the glass is close to the surface tension of water, electrical discharge appeared when the gap between the electrodes was set to a distance larger than  $10\ \mu\text{m}$  [64] and molten glass was widely distributed across the substrate as a result of the electrical discharge. This is attributed to the low breakdown threshold of air due to the high temperature that was used in the experiments (around  $850\ ^\circ\text{C}$ ). Therefore, operating at small gaps was the next attempt.

For simplicity and better control of small gaps,  $25\ \mu\text{m}$  diameter gold wire was set inside an alumina tube, and a heating element was wound around the tube in order to

supply the heat required to melt the glass. The gold wire was dipped into a molten borate glass reservoir nearby, and the experiment was conducted to eject material from the molten glass that adhered to the tip of the gold wire, as shown in Figure 3.5.

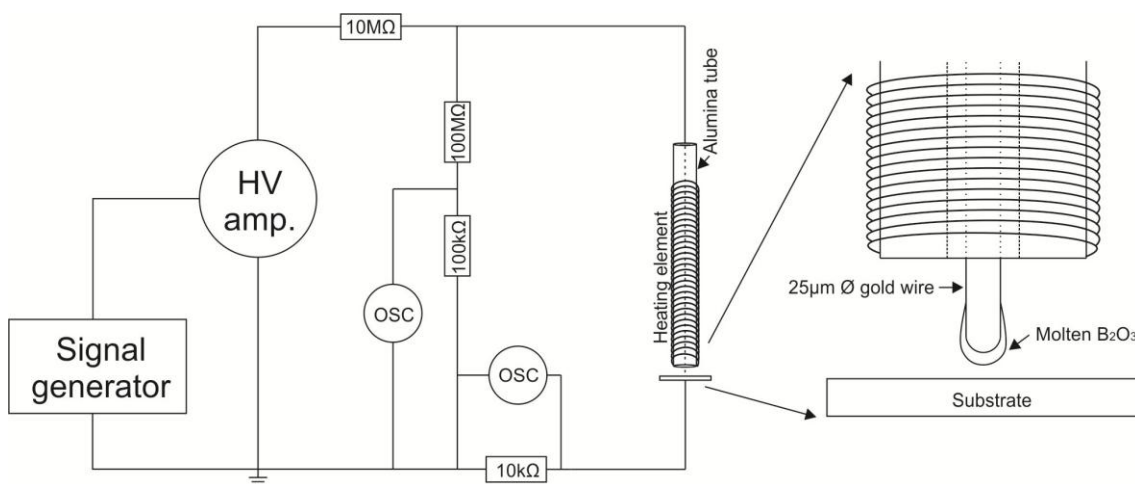


Figure 3.5 Schematic diagram of EHD setup on molten  $B_2O_3$

The substrate used was a silicon wafer with a 300 nm layer of silicon dioxide on the surface. The high voltage waveform was in the form of a triangle wave with a D.C. offset applied to the tip such that the applied voltage varied between 250 and 500 V (i.e. a triangle waveform of  $\pm 125$  V with a D.C. offset of +375 V). The D.C. offset continuously draws the molten borate glass towards the apex of the tip, which helps in resupplying the material to the tip when jetting occurs. The gap between the apex of the molten glass and the substrate was initially set to 50  $\mu m$ ; when the voltage supply was turned on, the gap was gradually reduced until it reached 10  $\mu m$ . Under these conditions material deposition on the substrate could be observed, indicating a glass ejection due to the high electric field at this small gap.

Analysing the deposited material on the substrate, strands of boron trioxide were seen with diameters in the region of 100 nm. A scanning electron microscope was used to obtain the micrographs, and an energy-dispersive x-ray EDX was used to analyse the materials of the deposition. The glass strands on the substrate appeared with overlapping pattern as shown in Figure 3.6.

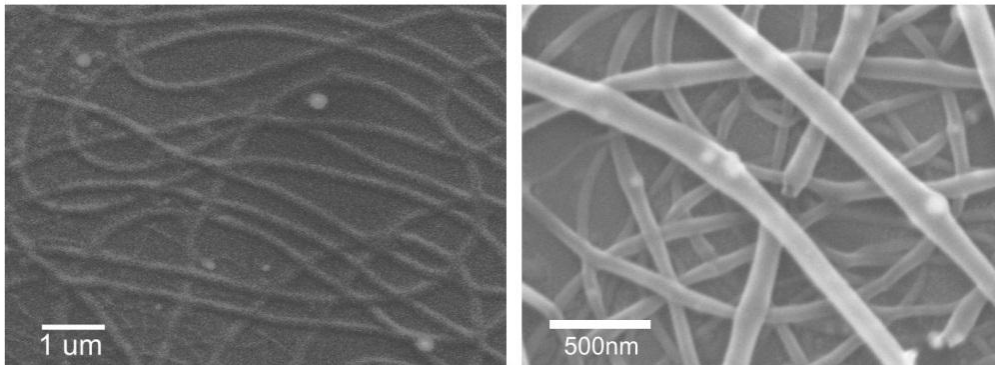


Figure 3.6 Samples of B<sub>2</sub>O<sub>3</sub> strands as they appeared on the substrate

Although molten glass ejection was successfully demonstrated using EHD, the challenges of conducting the experiment highlighted the difficulty of implementing EHD for higher surface tension materials.

An important observation from the presence of an electrical discharge was its ability to disintegrate material from the surface of the liquid meniscus, which led us to study the spark-stream technology, which then formed the major investigation of the following research.

### 3.5 Conclusion

The work on ejecting material from molten glasses and metals using EHD started by reviewing the surface tensions of these materials. It was found that metals have very high surface tension values compared to room temperature liquids and even molten glasses. In fact, initial experiments on molten indium were frustrated by the presence of an electrical discharge before any deformation of the molten indium meniscus could be observed. This led to directing the experiments toward glasses, and searching for low surface tension glasses.

Boron trioxide  $B_2O_3$ , a glass former, has low surface tension compared to other glasses that were surveyed, hence experiments were conducted using this material. As the experiments were conducted on molten glass in a hot environment, it was necessary to study the effect of temperature on electrical discharge, and also to study the conditions that cause an electrical discharge to happen in order to avoid it. As a result of this study, it was noticed that working with a small gap between the electrodes raises the breakdown threshold of air, and therefore EHD experiments were conducted in gaps of the order of  $10\ \mu m$ , and borate glass strands were successfully ejected.

This experience led to the study of electrical discharges as an alternative way of depositing materials.



## **Chapter 4**

### **4. Introduction to Spark-Stream technology**

#### **4.1 Introduction**

Electrical discharge has been known and experimentally demonstrated for over 200 years [65]. In fact, throughout history man has observed the enormous effect of lightning which is an electrical discharge, and many applications have been generated using electrical discharges.

Owing to the enormous temperatures that can be achieved from an electrical discharge, reaching 40,000 K – 50,000 K [66,67,68,69], electrical discharge is a promising candidate for eroding a wide range of materials, through melting and vaporising the discharge electrodes.

The proposed concept of spark-stream technology, as shown in Figure 4.1, is to generate nanoparticles by a spark discharge, and then manipulate the trajectories of the generated particles to follow a certain electric field path in order to achieve focussing of the particles into well-defined spots.

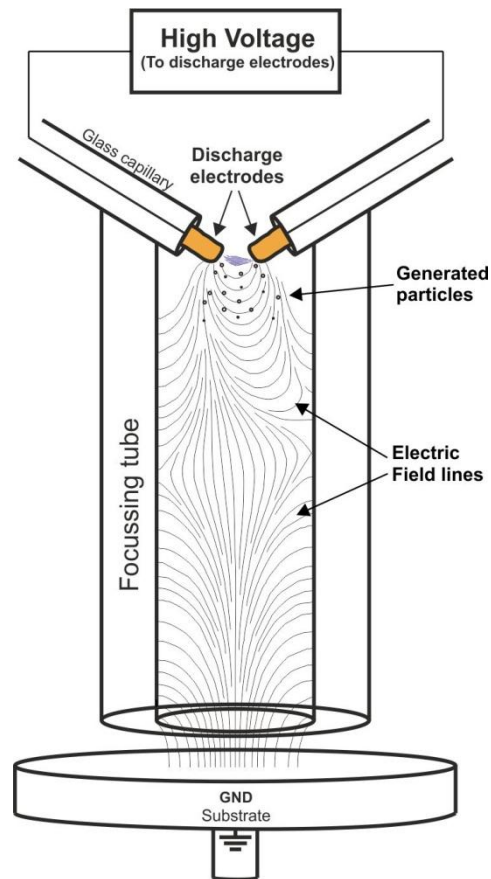


Figure 4.1 Concept of spark-stream technology

In this chapter, an introduction to the electrical discharge phenomenon is given, and the reason for high temperatures arising in the discharge, which leads to material erosion, is discussed. Particle formation and the concept of electrostatic focussing are also introduced in this chapter, including the process of forming nanoparticles from the vapour of the electrodes and from splashes from micro-pools on the surfaces of the electrodes.

This chapter is an introduction to the spark-stream technology, and in the next chapters the experimental demonstration of nanoparticle generation and the focussing mechanism of nanoparticles will be discussed.

## **4.2 Why electrical discharge**

As was shown in chapter 3, electrical discharge appeared as a challenge to implementing EHD jetting with high surface tension liquids. The occurrence of sparks highlighted the ability of electrical discharge to disintegrate particles from bulk materials.

A survey of electrical discharge applications shows that electrical discharge is the main driver of Electrical Discharge Machining (EDM) technology, which is a widely used approach to machine metals and ceramics [70,71,72]. The technology uses the ability of an electrical discharge to erode materials in order to engrave a work piece and shape it with different patterns [73,74,75]. The eroded material in EDM is washed away with a dielectric liquid, unlike the proposed spark-stream technology where the material eroded is controlled to follow specific trajectories, as shown in Figure 4.1.

Producing nanoparticles from electrical discharge has been reported in the past decade, and several materials have been demonstrated [76,77,78,79,80,81]. A number of studies were conducted to analyse some properties of the generated nanoparticles [78,79,80,81], yet to our knowledge no work has been done to control the direction of the generated nanoparticles for direct write purposes.

Other recent reports have studied depositing nanoparticles on masked substrates and, in this way, have achieved a similar focussing effect to the one reported in this research [82,83,84]. Using polymer-based masks on top of conductive substrates with patterns etched on the masks, it was possible to direct the nanoparticles towards the



conductive etched patterns, and deposit the particles to follow the shape of the masked patterns.

### **4.3 Electrical discharge phenomena**

An electrical discharge is generated when a high voltage is applied across a gap - in our case filled with air under room conditions - and the applied potential exceeds the breakdown threshold of the air. Current then flows through the gaseous plasma forming a conducting channel between the electrodes.

When a high electric field is applied across two electrodes, any free electrons between the electrodes will accelerate toward the anode. Initial free electrons are excited by photo-ionisation, where photons can be absorbed by a molecule, which gives up an electron and becomes a positive ion [85,86]. When the initially excited electrons move toward the anode, collisions with other molecules excite more electrons, and a cascading effect of electrons avalanche accelerates toward the anode, leaving positively charged ions moving toward the cathode. The bombardment of the cathode by positively charged ions excites more electrons from the surface of the cathode, maintaining the avalanche effect [85,86,87], see Figure 2.4.

This sudden flow of electrons and ions generates enormous heat and pressure that can exceed atmospheric conditions with studies reporting temperatures of the order of 40,000 K [67,68,69].

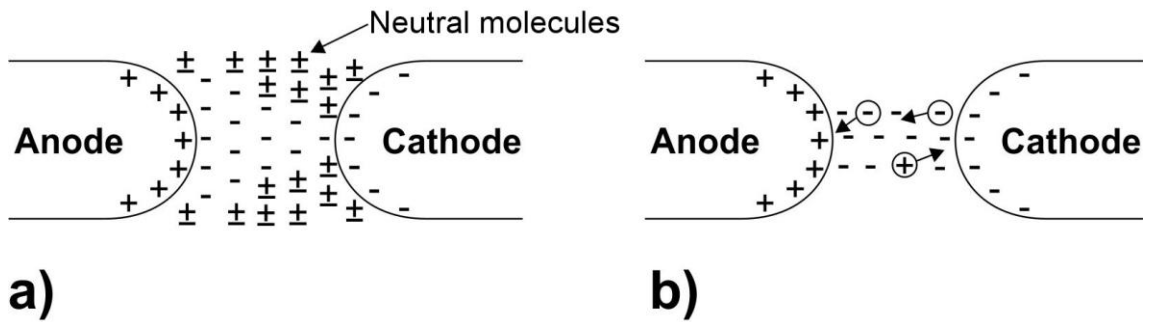


Figure 4.2 a) Electron avalanche cascading toward the anode, b) electrons and ions flow in the discharge channel

When the conducting channel is formed, the potential difference between the electrodes drops; this appears in the form of a sudden drop of voltage across the electrodes, hence a drop in the electric field. The flow of electrons and ions driven by the electric field eventually loses its energy. The potential difference between the electrodes recovers and raises the electric field until another breakdown occurs. This repetitive process appears in the oscillatory behaviour of the voltage across the discharging electrodes and is well reported in the literature [79,81] as shown in Figure 4.3.

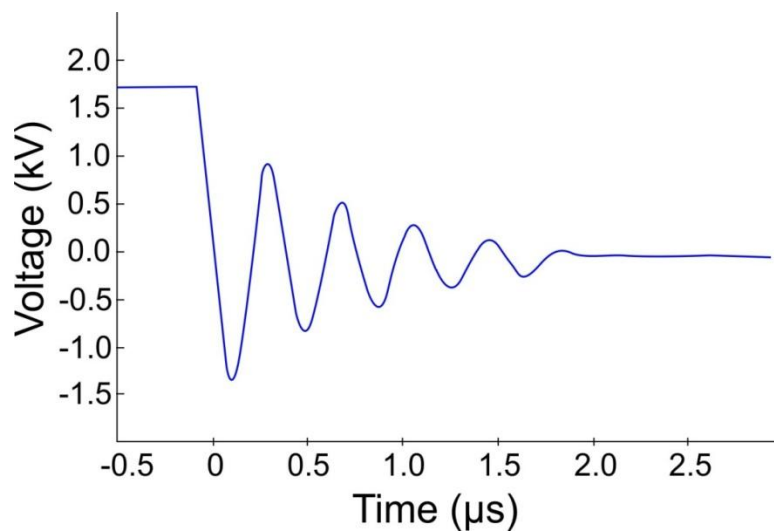


Figure 4.3 Oscillatory behaviour of the voltage across the discharge [79]

## **4.4 Mechanism of particle formation**

In spark discharge, two mechanisms of particle formation are discussed in the literature; one is based on the formation of particles from the vapour of the electrodes, and the other is from splashes of micro-pools around the discharge channel on the surface of the electrodes, as it will be described below.

### **4.4.1 From the vapour of the electrodes**

The main mechanism of forming nanoparticles in a spark discharge is reported to be due to the condensation of the vapour that is evaporated from the electrodes [77,79,80].

The heat generated in the discharge is enough to melt and/or vaporise the material in the electrodes, forming a plasma cloud of ionised atoms and free electrons in the discharge channel.

As some of these ionised atoms move away from the discharge channel following the electric field gradient, they cool down and combine with free electrons around the discharged channel and with other ionised or neutral atoms forming charged nanoparticles.

Also, because of the oscillatory behaviour of the discharge, when the electric field is low, some ions and electron combine forming neutral atoms as they lose their momentum. The produced neutral atoms in the diffusive environment collide with each other and with other ions and electrons so charged nanoparticles are formed.

#### 4.4.2 From molten micro-pools

Another reported mechanism to produce particles in a spark discharge is due to the strong pressure fluctuations at the moment of discharge [76,79,88]. Although temperatures in the centre of the discharge can vaporise the material of the electrodes forming craters on the surface, surrounding areas around these craters at the moment of the discharge can be molten, forming micro-pools of the electrode material, as shown in Figure 4.4. The extreme fluctuation of pressure due to the rapid heating at the moment of discharge ejects liquid material from the electrode micro-pools, forming spherical particles, which are normally larger than the particles produced from the vapour.

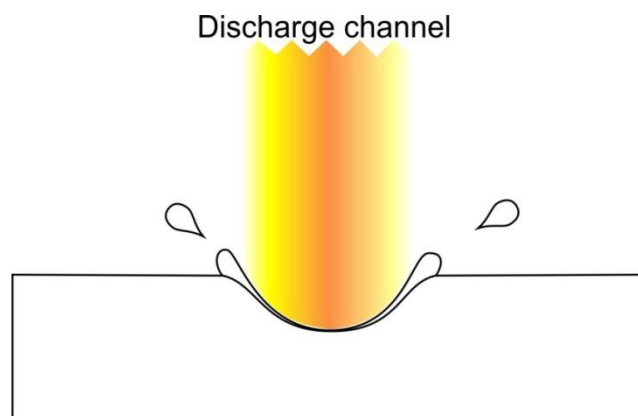


Figure 4.4 Effect of pressure fluctuations on the micro-pools in the electrodes

### 4.5 Introduction to electrostatic focussing of particles

Since J. J. Thomson demonstrated the ability to deflect cathode rays in vacuum tubes [89,90], the idea of controlling the trajectories of charged particles has been a major area of study. The concept is to use an electric field to deflect a beam of charged particles as shown in Figure 4.5. This concept has been in use for decades to control elec-

tron beams and ion beams in vacuum for many applications such as scanning electron microscopy and focused ion beam lithography [89,91,92].

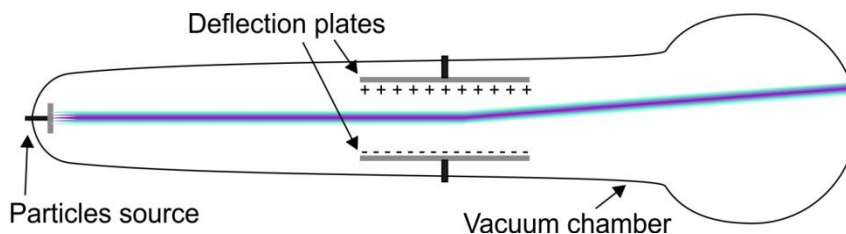


Figure 4.5 The deflection of charged particles concept

In the presence of gases or liquids, the electrostatic deflection of particles appears in many applications in particle filtration [93,94], nanoparticle positioning [95,96,97] and, in recent years, in electrophoretic ink (e-ink) display applications [98,99].

Focussing of nanoparticles generated from an electrical discharge has been reported in the past few years by guiding the charged nanoparticles to follow electric field paths on masked substrates [82,83,84]. The concept was to use insulating masks on grounded substrates, and by etching specific patterns on the mask, the etched grounded areas attract the charged nanoparticles toward its centre. This happens because the insulating masks build up a charge that converges the arriving charged particles, focussing them in the centre of the pattern [83,84].

## **4.6 Conclusion**

When an electrical discharge happens, a sudden flow of electrons and ions occurs. An electrical discharge can locally raise the temperature of electrodes to more than that required to melt and vaporise material from the electrodes.

An electrical discharge is a widely used phenomenon in many research and industrial techniques. Electrical Discharge Machining (EDM) technology uses electrical discharge to erode material from a work piece and shape it. Electrical discharge is also used to produce nanoparticles from a wide range of materials.

Charged particles in vacuum have been manipulated, and their trajectories have been studied. In the past few decades the study of charged nanoparticles in fluids was used in many applications. Recent reports used lithographic methods to deposit nanoparticles generated by electrical discharge in masked patterns in different gases.

Our proposed spark-stream technology uses electrical discharge to generate nanoparticles and then direct the particles to follow a desired path in order to focus the particles onto small spots. The produced nanoparticles are focussed in real time as they are generated, and the process begins directly from bulk material with minimal pre and pro-processing requirements.



## **Chapter 5**

### **5. Production of nanoparticles using Spark-Stream technology**

#### **5.1 Introduction**

Spark-stream technology is a process of producing nanoparticles using spark electrical discharge, and then focussing the stream of nanoparticles in pre-defined patterns. In this chapter, the production of nanoparticles will be discussed while in the next chapter the study will be on the focussing of the particle stream.

The setups used to produce metal, metal-oxide and glass particles using an electrical discharge are studied with sample graphs of the produced particles from different materials, with energy-dispersive x-ray (EDX) spectra showing the compositions of the deposited material.

Finally, some properties of the generated particles are discussed; the size of the particles, the charge polarity of the generated particles, and the electrical conductivity of the deposition. All these properties are experimentally studied using different characterisation methods.



## **5.2 Experiments on nanoparticle production**

Spark-stream setups discussed in this chapter have in common two electrodes of the deposition material, where a spark discharge is generated between the electrodes. In the case of metals, a high voltage is supplied to the electrodes directly and the discharge occurs in air, so materials like zinc (Zn) and silicon (Si) oxidise as the particles are formed. Glass, on the other hand, is melted inside capillaries to increase its electrical conductivity, and the tips of the molten glass protruding from the capillaries act as the discharging electrodes. The following subsections discuss each setup in detail.

### **5.2.1 Metal and metal-oxide nanoparticles**

Gold (Au) electrodes were used in most experiments due to this material's chemical stability in air. However, other experiments on different materials were conducted to demonstrate the ability of an electrical discharge to produce metal oxide nanoparticles from zinc (Zn) and silicon (Si) electrodes, as will be described later on.

The spark-stream setup consists of two gold electrodes located inside a focussing tube as shown in Figure 5.1.

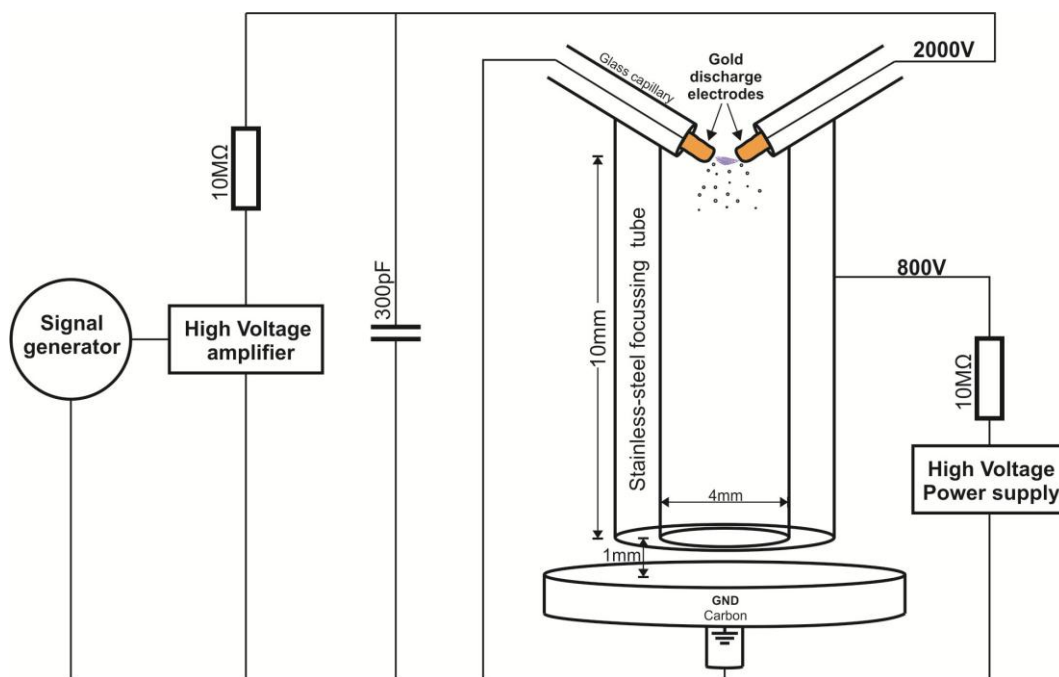


Figure 5.1 Schematic diagram of spark-stream apparatus

The gold electrodes are connected to a high voltage amplifier (from Trek Inc - provides up to  $\pm 10$  kV, 40 mA), and a capacitor capable of working at high voltages is connected in parallel to the high voltage line. The 10M $\Omega$  resistors are used to protect the high voltage sources to avoid drawing current that is beyond the supply's limit when a discharge occurs.

The voltage supplied to the discharge electrodes was in the form of a square wave (100ms period and 50 % duty cycle). When voltage is first supplied, the capacitor starts charging and storing energy. When the voltage across the electrodes is higher than the breakdown threshold of air, an electrical discharge happens, and the energy stored in the capacitor is released in the discharge channel, generating heat and pressure as described in the particle formation section.

The generated nanoparticles are collected on the grounded carbon substrate (SEM stub). In our experiments, the particles were clustered and observed on the substrate to form micro-scale islands, as shown in Figure 5.2.

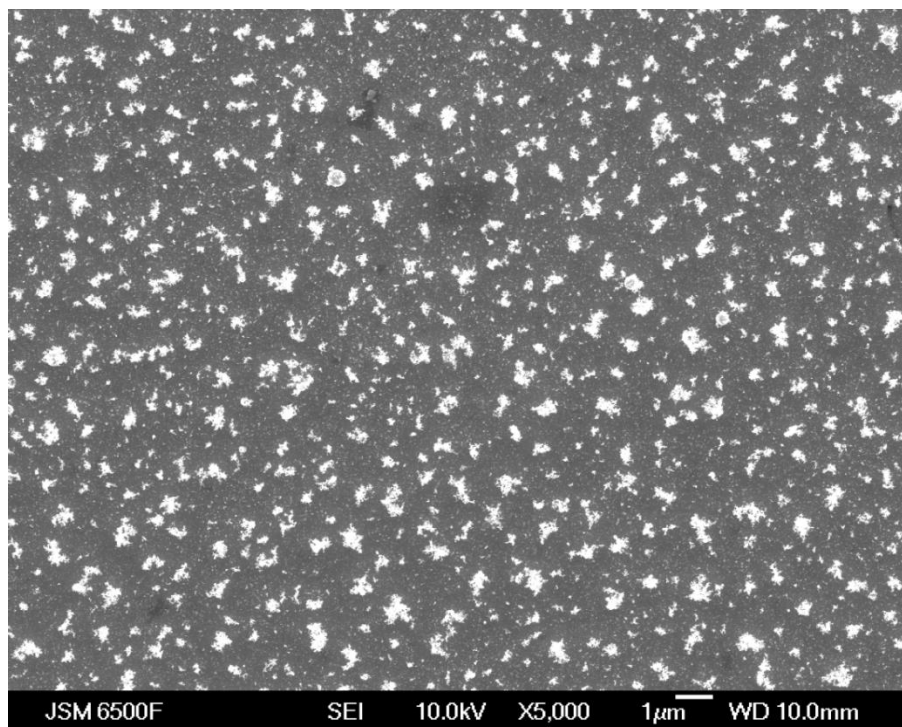


Figure 5.2 Scanning electron microscope (SEM) graph of clusters of gold particles deposited on a carbon substrate

This pattern of deposition is thought to be due to guidance by the electric field; the first particles deposited on the substrate enhance the electric field gradient around the particles, and guide other generated particles towards them (See Figure 5.3). The island-shape clusters were our first observation of particles following the electric field EF lines, which led to further study of nanoparticle focussing.

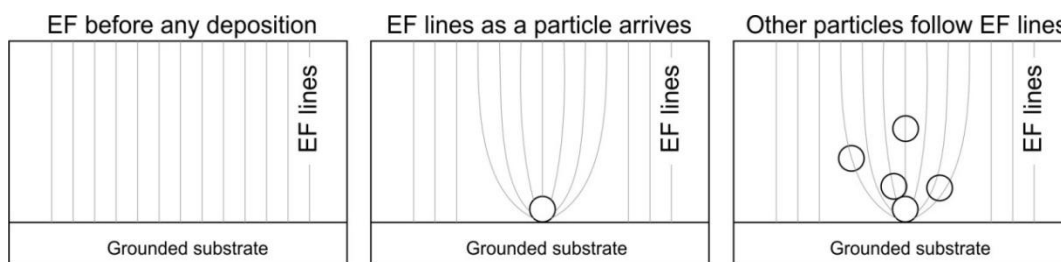


Figure 5.3 Clustering of particles following the electric field lines

When the deposition was analysed using a transmission electron microscope (TEM), it was possible to see finer nanoscale clusters of gold particles, as shown in Figure 5.4. Further details of the particle size will be discussed in section 5.3 on the properties of nanoparticles.

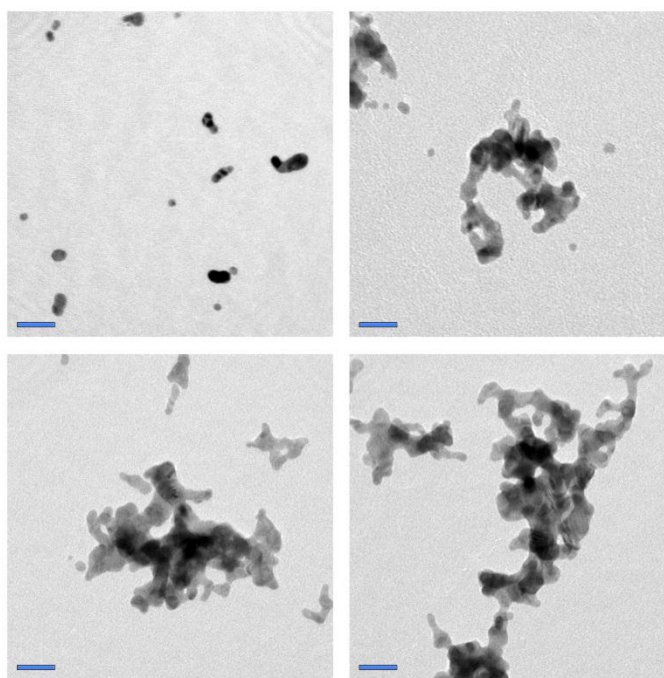


Figure 5.4 TEM graphs of fine clusters of gold nanoparticles (scale bar 20nm)

The same setup was used with other metals and semiconductors in air. Zinc (Zn) and Silicon (Si) were used, and the depositions were analysed using scanning electron mi-

croscopy (SEM) and energy-dispersive X-ray (EDX) in order to know the composition of the deposited particles (Figure 5.5). A strong presence of oxygen appears in the spectrum when the depositions are produced from zinc and silicon electrodes, suggesting that the zinc and silicon particles were oxidised in air as they were formed from vapour, as would be expected given the formation conditions.

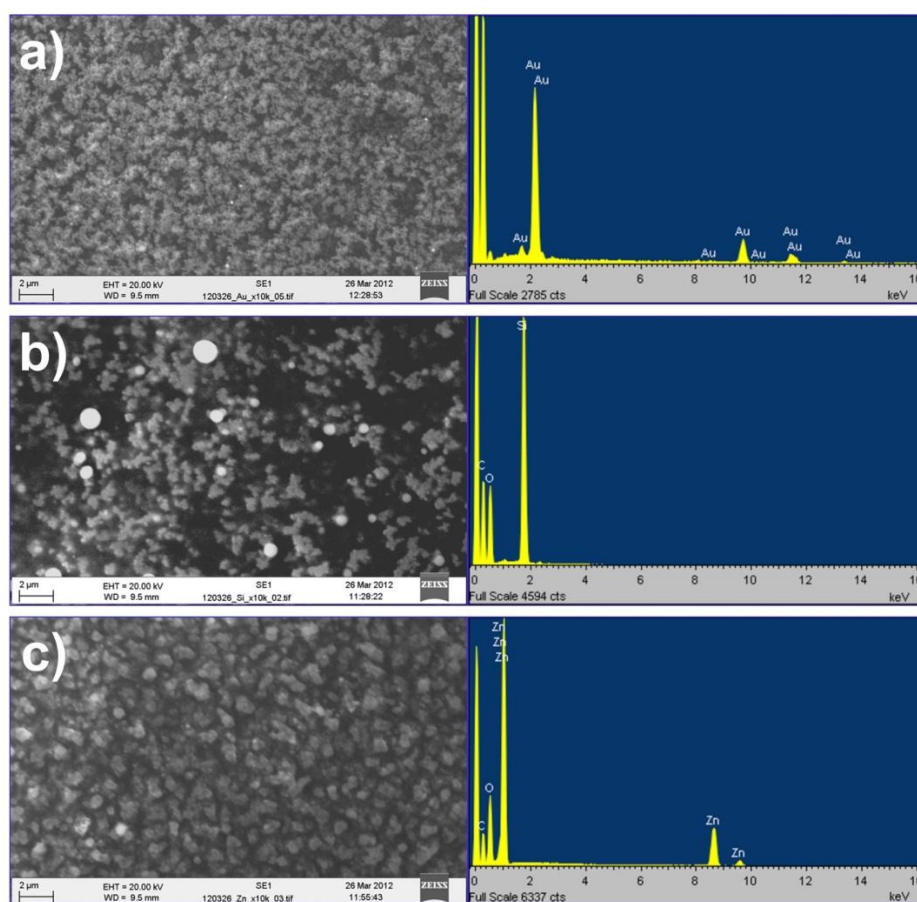


Figure 5.5 a) (left) SEM graph of particles deposited from gold electrodes in air, and (right) EDX spectrum showing gold composition, b) (left) SEM graph of particles deposited from silicon electrodes in air, and (right) EDX spectrum showing silicon and oxygen composition, c) (left) SEM graph of particles deposited from zinc electrodes in air, and (right) EDX spectrum showing zinc and oxygen composition.

The nanoscale cluster formation shown in the SEM images in Figure 5.5 is a common feature of nanoparticle deposition produced by electrical discharge. However, a few spherical microscale particles appear in the images of Figure 5.5, which can be generated from the molten part of the electrodes as described in section 4.4.2, where the temperature of the area around the discharge channel can be above the melting point of the material of the electrodes but below the boiling temperature, so the pressure fluctuations occurring at the moment of the discharge eject microscale droplets from the micro-pools as it was referred to in section 4.4.2.

### **5.2.2 Glass nano and microspheres**

Although glasses are considered to be electrical insulators in most ambient conditions, their electrical conductivity in fact increases significantly when they are molten [100,101].

Tellurite glasses have low melting points of around 700 K, compared with 1800 K for silicate glasses [101,102,103]. This makes tellurite glasses more convenient for experiments using metal-based heating elements that can only reach temperatures around 1300 K.

The electrical resistivity of a tellurite glass (75%TeO<sub>2</sub> – 20%ZnO – 5%Na<sub>2</sub>O) made in-house by Xian Feng (a senior researcher in the project) was measured experimentally; the results are shown in Figure 5.6.

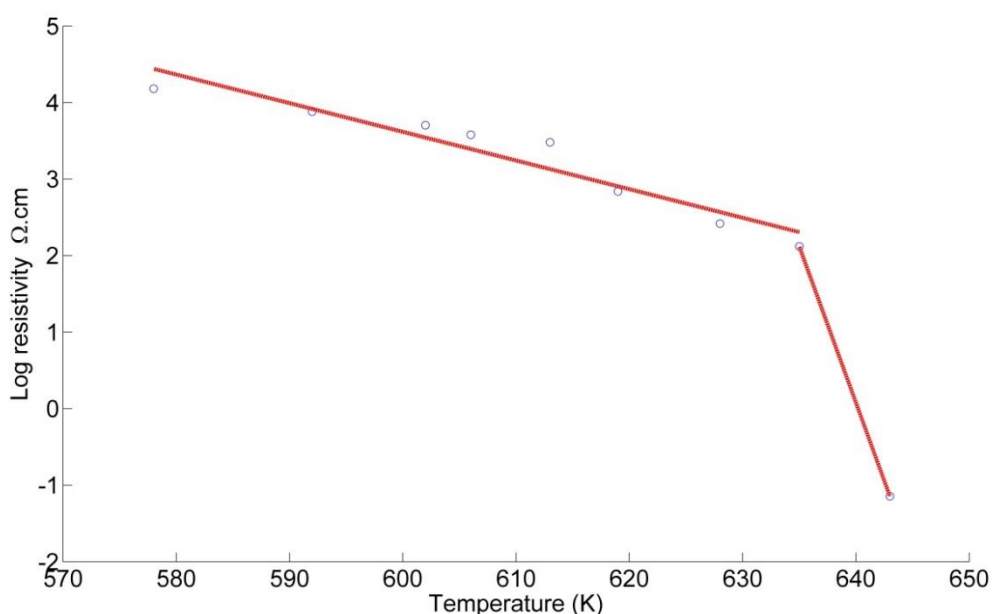


Figure 5.6 Electrical resistivity of tellurite glass made in-house (75%TeO<sub>2</sub> – 20%ZnO – 5%Na<sub>2</sub>O)

The setup for generating glass particles using electrical discharge is similar to the one used to generate metal nanoparticles, except for the electrodes, which are made of molten glass at 725 K.

The tellurite glass was grinded and placed inside silica glass capillaries. A heating element (80% Nickel - 20% Chromium wire) was coiled around the silica capillaries in order to melt the tellurite glass inside. The discharge electrodes were placed inside a silica glass tube which had its internal wall covered by a brass foil, as shown in Figure 5.7.

Owing to the presence of the heating element, which is needed to keep the glass in a conducting state, and to avoid opposing the field-assisted motion by the convective drift of hot air, the orientation of the setup was upside-down relative to the gold setup in order to be able to collect all the generated particles.

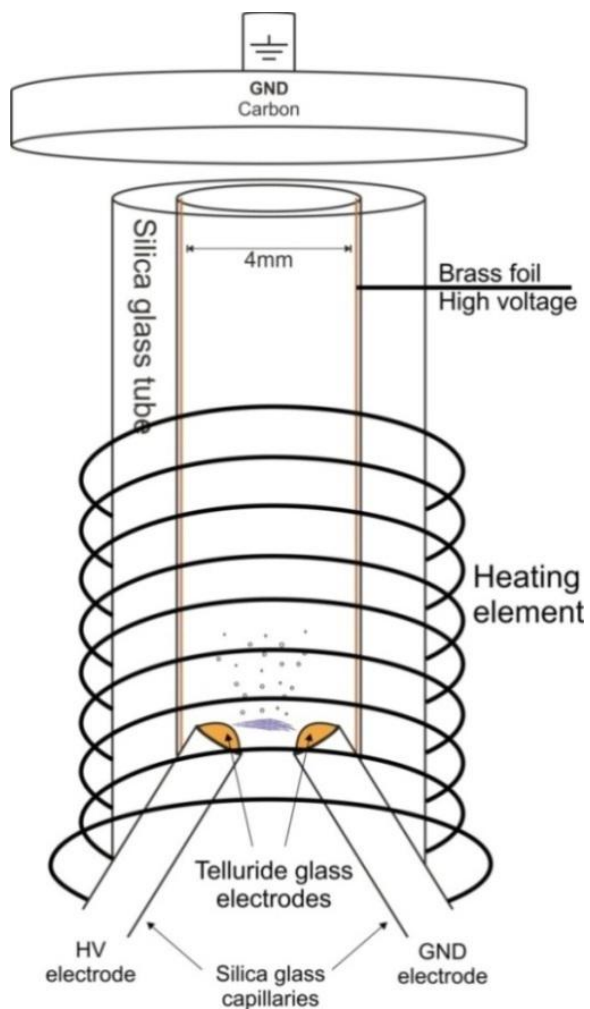


Figure 5.7 Spark-stream setup diagram for producing glass particles

Figure 5.8 is an SEM graph of the deposited glass particles on a silicon substrate.

The particles on the substrate appear in two forms; microscale spherical particles, and fine nanoscale clusters which appear as a ripple on the surface of the substrate. Further analysis of this behaviour is discussed in the next section 5.3.1.



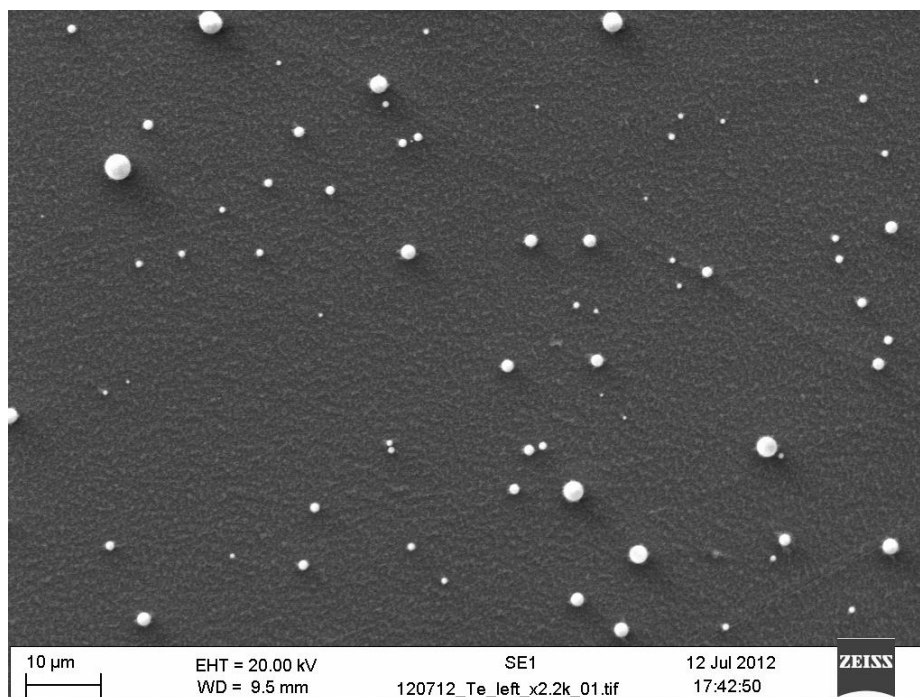


Figure 5.8 SEM micrograph of tellurite glass particles generated by electrical discharge

## 5.3 Properties of nanoparticles

### 5.3.1 Size of nanoparticles

We conducted most of the experiments using gold electrodes, therefore the properties of particles were studied mainly using gold nanoparticles. Using the TEM micrographs of gold nanoparticles, the size range of the particles was found to be in the range of 4 nm to 12 nm in diameter. This size range has also been reported in other studies that generated gold nanoparticles from electrical discharge using similar configurations [79,80].

The clusters shown in Figure 5.4 have also been previously reported and explained, where this large aggregation of nanoparticles appears only on the substrate and not in

the discharge region or on flight [79]. The aerosol of gold nanoparticles generated in similar configurations are reported [79,80], the generated particles were analysed using differential mobility analysis (DMA) during flight, and no large aggregations are reported, so the conclusion is that these particles aggregate only very close to, or on, the substrate.

A few larger spherical gold particles were also observed, with a size ranging from 100nm to around 1  $\mu\text{m}$ , as shown in Figure 5.9.

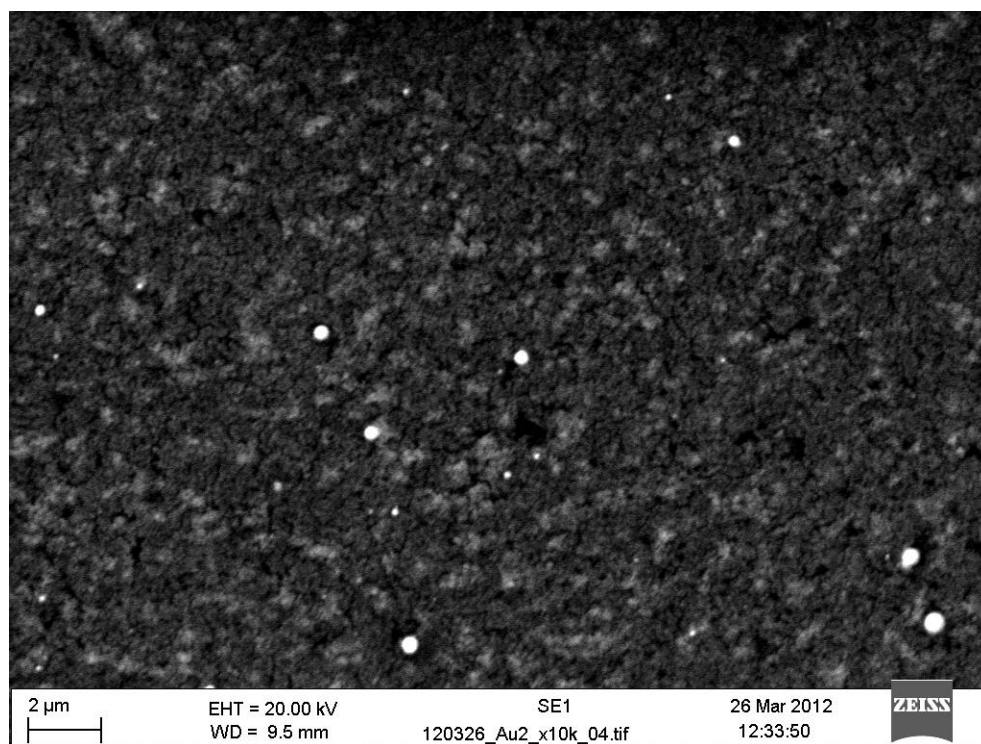


Figure 5.9 SEM micrograph of spherical gold particles generated by the same spark-stream setup

The presence of larger particles is reported to be due to high pressure fluctuations associated with the electrical discharge [76,79,80]. Although the temperatures at the discharge channels are sufficient to vaporise the material in the electrodes, the tempera-

ture away from the discharge centre would fall between the melting and boiling temperatures of the electrode material, leaving micro-scale pools of molten material [79].

As described in the particles formation section, the extreme pressure fluctuations disintegrate liquid material from the electrodes' micro-pools, and forms microscale spherical shape particles [76,79]. The effect of this phenomenon appears on the surface of the electrodes after the experiment, where a torus formation appears around smooth craters, as shown in Figure 5.10.

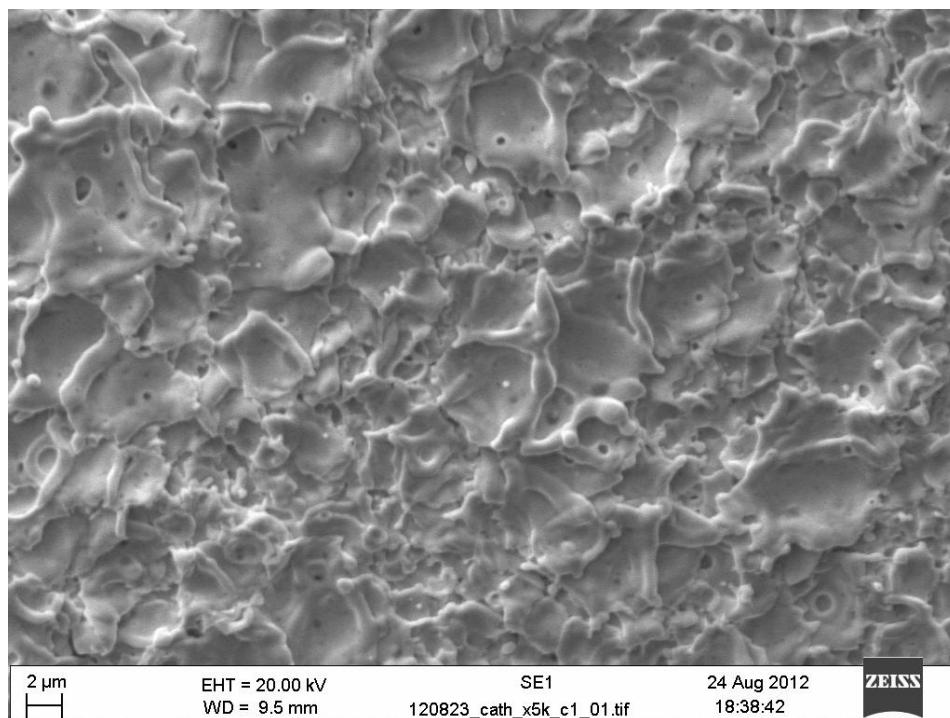


Figure 5.10 SEM graph of a gold electrode after an experiment, where the tori appear surrounding craters

The oxidised nanoparticles from the zinc and the silicon electrodes were not analysed using TEM, therefore there was no exact quantitative data on their size. However, SEM micrographs of the oxides show the clustering effect on the substrate, where submi-

cron branch growth is observed, similar to that described in Figure 5.3 in section 5.2.1.

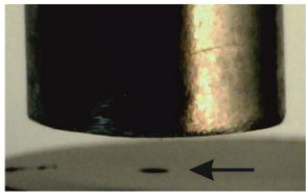
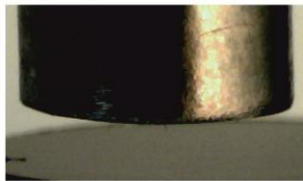
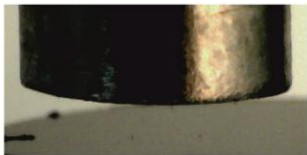
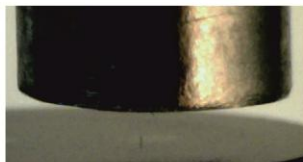
The tellurite glass particles shown in Figure 5.8 confirm the effect of strong pressure fluctuations in generating micro-scale particles. As the tellurite glass electrodes were molten to allow for electrical conduction, strong pressure fluctuations at the moment of the discharge initiated microscopic splashes of molten glass which formed large numbers of micro-scale glass spheres.

### **5.3.2 Charge polarity of nanoparticles**

In order to determine the dominant polarity of the charge on the nanoparticles, a series of experiments was conducted. By altering the polarity of the potentials applied to the electrodes and the metal focussing tube, one could observe the behaviour of the deposited material and infer some basic properties of the charge of the nanoparticles.

A potential of  $\pm 800$  V was applied to the stainless-steel tube (4 mm internal diameter (ID)) that surrounded the discharge gold electrodes, as shown in Figure 5.1 in section 5.2.1 above. The discharge voltage (between the gold wire electrodes) was either +2 kV to ground or -2 kV to ground. Regions of deposition on the substrate were examined using an optical microscope and an SEM. The results of this series of experiments using different voltage configurations appear in Table 5.1.

Table 5.1 Effect of the focussing tube voltage polarity on the deposition of nanoparticles.

Tube V. Electrodes V.	+800 volts	-800 volts
+2000 volts	<b>Case: 1</b> 	<b>Case: 2</b> 
-2000 volts	<b>Case: 3</b> 	<b>Case: 4</b> 

Pronounced deposition (arrowed) appeared using a positive discharge polarity with a positive voltage on the stainless-steel tube (case 1). Cases 2, 3 and 4 generated little deposition. In case 4 the deposition was slightly higher than cases 2 and 3, although this is difficult to discern in the images shown above.

These results suggest that positive and negative polarity nanoparticles are produced by the electrical discharge. However, when the discharge electrode and tube voltages are of the same polarity, more deposition is observed. Deposition using a positive voltage polarity (case 1) was much higher than all other cases, suggesting that many more positively charged nanoparticles are generated by the discharge. When the polarity of the tube and discharge electrodes are opposed, the majority of nanoparticles are attracted towards the tube walls and do not reach the substrate.

### 5.3.3 Electrical resistance of deposition

The patterned nature of the nanoparticle-based deposition, which forms island-shape clusters, highlighted the need to establish experimentally the electrical resistance of the deposited films. Gold nanoparticles were deposited between two aluminium electrodes on an insulating vinyl substrate. Because of the insulating substrate, nanoparticles tend to follow the electric field lines toward the aluminium electrodes, avoiding the insulating gap area. So in order to make sure the particles are distributed well within the gap between the electrodes, the aluminium electrodes and the gap between the electrodes were coated with a highly resistive carbon thin film as shown in Figure 5.11.

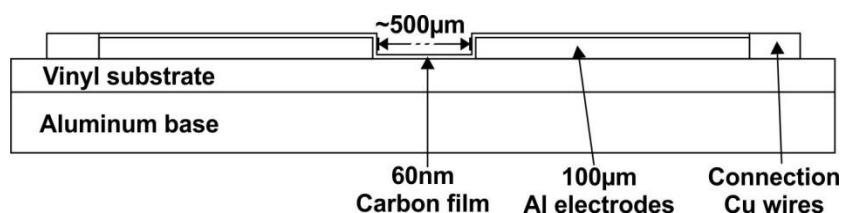


Figure 5.11 Schematic diagram of the substrate used for resistance measurement.

The resistance of the carbon thin film was measured before and after depositing gold nanoparticles. The nanoparticles were generated by 100ms high voltage pulses with 50% duty cycle. Each pulse is referred to as a shot, and the resistance measurement was conducted after a certain number of shots, by measuring the current-voltage I-V curves of the deposited material. Figure 5.12 shows the resistance of the deposition at different stages of accumulating gold nanoparticles between the aluminium electrodes. The circuit used to measure the I-V curves and a list of the I-V curves are shown in Appendix 3.

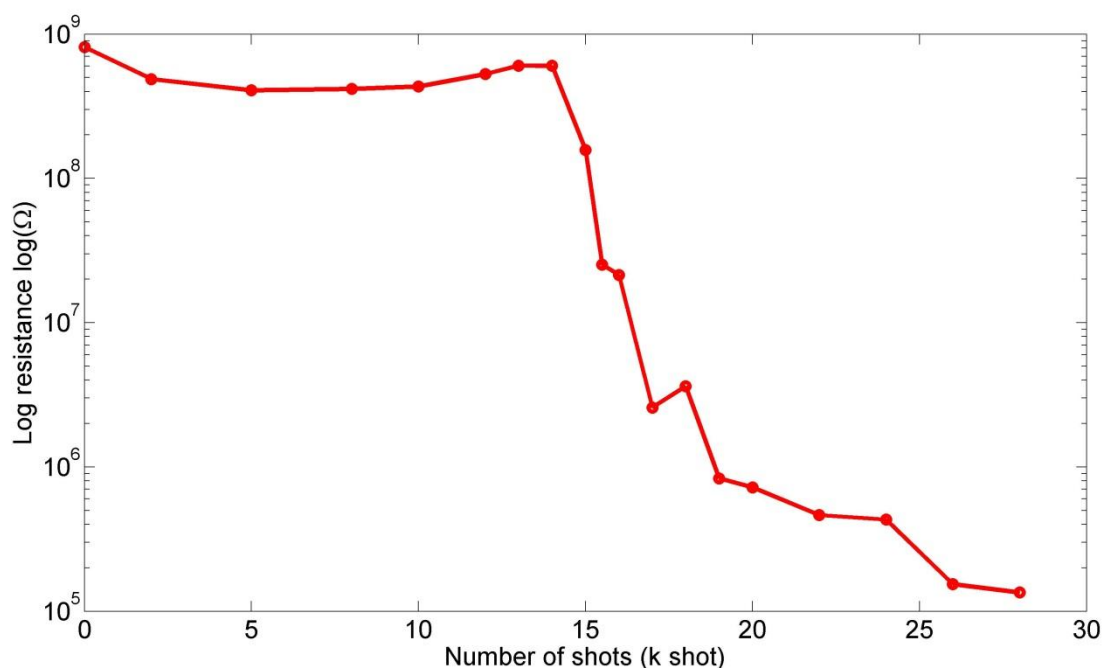


Figure 5.12 Resistance of gold nanoparticle deposition between two aluminium electrodes

The number of shots starts from zero, when the resistance shown is the resistance of the carbon thin film. As gold nanoparticles are deposited, the resistance of the bridge between the aluminium electrodes drops. However, a slight increase of the resistance appeared between 10-15 k shots, afterward a sharp drop of the resistance occurs from around 15 k shots onward.

The process of forming a conductive bridge between the aluminium electrodes starts by forming island-shape clusters. These gold clusters form short conductive paths that cause a slight drop of the resistance. However, when the gold deposition is dense enough to link at least one complete path of clusters between the aluminium electrodes, under which circumstances the conduction is referred to as percolation, a sudden drop of the resistance appears as shown at around 15 k shots. Further deposition

produces more 'percolating' conductive paths and drops the resistance further. This percolation behaviour is reported for other material nanoparticles, where a sudden drop of resistance appears at certain density of nanoparticles [104,105].

The slight increase in resistance before 15 k shots was unexplained and required further investigation. During the process of measuring the resistance of the carbon thin film, this slight increase of resistance was observed. To assess this behaviour, a carbon thin film similar to the one shown in Figure 5.11 was deposited, and its resistance was measured at different times for few hours as shown in Figure 5.13.

The increase of the resistance of the carbon thin film could explain the overall slight increase of resistance of the deposition before 15 k shots. This effect of the carbon film resistance becomes negligible when gold clusters form complete paths between the electrodes, and the percolation behaviour becomes dominant.



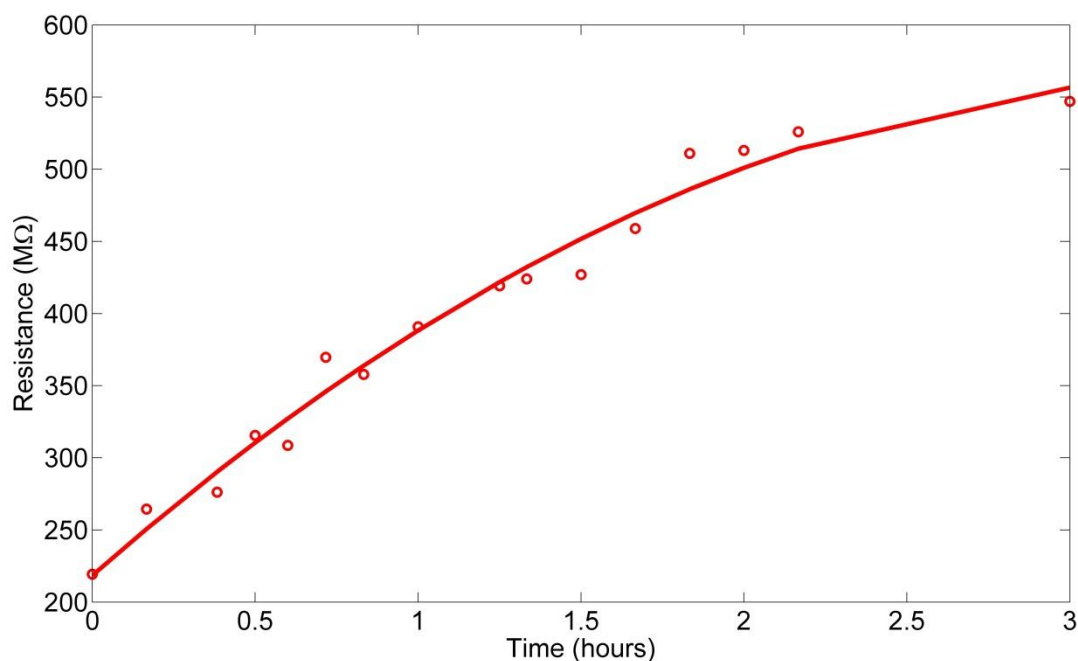


Figure 5.13 Resistance of carbon thin film changes with time.

The reason for the increase of the carbon film resistance with time could be the resistance measurement method itself. Although the current used to form the I-V curves to measure the resistance is less than  $1\ \mu\text{A}$ , it is possible that this current is sufficient to affect the behaviour of the 60nm carbon thin film. Nevertheless, as the resistance of the carbon thin film becomes less dominant when the percolation behaviour takes over, there was no further investigation of the carbon film resistance.

## 5.4 Conclusion

Nanoparticles are generated from bulk material in air using electrical discharge. Owing to the enormous temperature rise at the moment of discharge, the material of the elec-

trodes is vaporised, forming charged nanoparticles when the vapour condenses. Gold nanoparticles of the order of 10 nm diameter were produced. Experiments to produce nanoparticles of zinc and silicon oxide were also conducted. The same concept was used to generate glass particles using electrical discharge, where microscale glass spheres were produced from molten tellurite glass electrodes.

Some properties of the produced gold nanoparticles were analysed. The dominant charge polarity of the majority of the particles is positive. The electrical resistance of the deposited material was also measured, showing percolation conduction.

This chapter detailed the production of nanoparticles using spark electrical discharge, which is the first process of spark-stream technology, and the following chapter will discuss the focussing mechanism of the produced particles.



## **Chapter 6**

### **6. Focussing of nanoparticles**

#### **6.1 Introduction**

The concept of focussing nanoparticles generated by electrical discharge in a gas is the other part of studying the spark-stream technology. Nanoparticles are produced by an electrical discharge inside a focussing tube. This forms a stream of particles focussed as it moves toward the substrate.

In air, the nanoparticles do not follow ballistic trajectories. In the presence of an electric field, charged nanoparticles tend to move along the electric field lines. However, due to the presence of air and the charge of the particles, the particles deviate from following the field lines because of the diffusion and the particle interactions.

In this chapter nanoparticle focussing is introduced, and the forces involved in controlling the particle trajectories are analysed. The theories of diffusion and charged particle interaction are also discussed, highlighting many parameters that influence the focussing of nanoparticles in flight, including the dimensions of the focussing apparatus, the charge of the particles and the density of particle production.

To reduce the deposition spot size using this direct write approach, some of the parameters involved in controlling the focussing effect were manipulated, in particular scaling down the focussing apparatus, and reducing the density of particles produced, hence spot sizes of the order of  $20\text{ }\mu\text{m}$  were deposited.

## **6.2 Theory of electrostatic focussing**

### **6.2.1 Concept of focussing**

Previously reported observations during the early stages of developing the spark-stream technology showed the possibility of manipulating the nanoparticle trajectories. In particular, the island-shaped clusters that appeared while producing the nanoparticles were the first indication of electric field guidance. Also, the theory of particle formation from spark discharge suggests a strong presence of charge on the produced particles, which indicates that the particles can be influenced by electric field manipulation.

The aim of nanoparticle focussing is to guide the particles produced by the spark discharge to follow converging paths. The particle guidance is achieved by producing the particles inside a predefined electric field gradient, so the particles follow the electric field lines.

Using a simple metallic tube to surround the discharging electrodes in air, a voltage applied to the tube will create an electric field gradient with converging field lines at the bottom of the tube toward any grounded substrate, as shown in Figure 6.1.

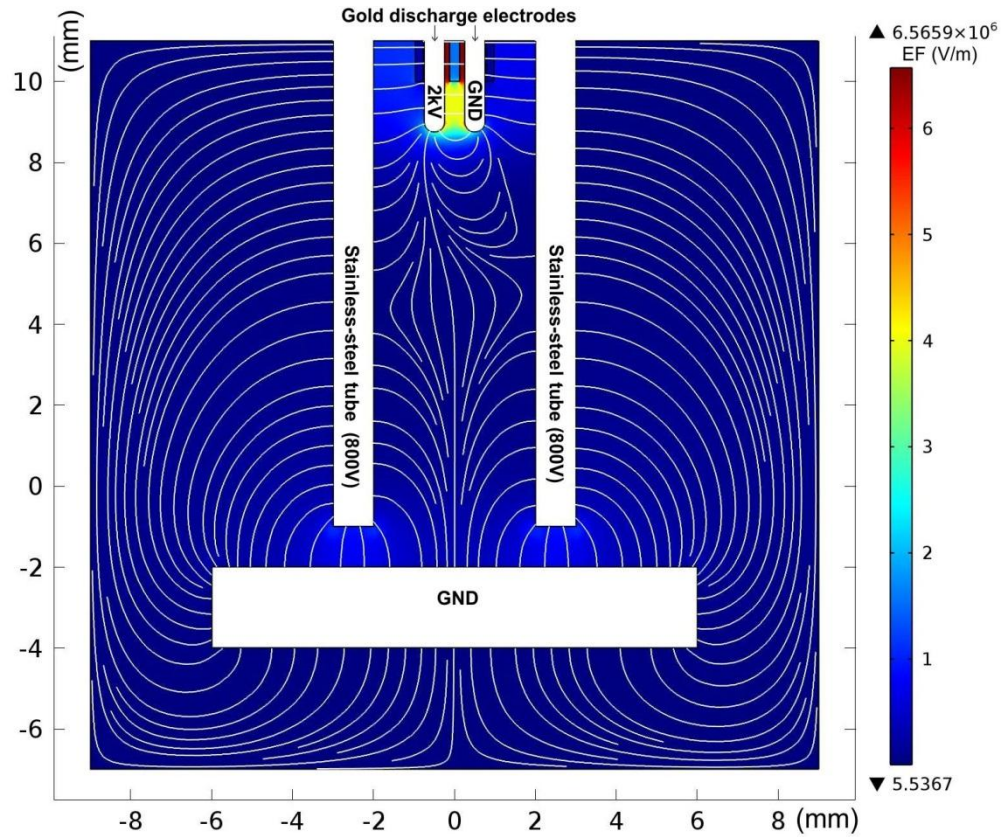


Figure 6.1 Electric field lines converging as a result of the voltage applied to the stainless tube.

In this configuration, voltage is applied to the gold electrodes to generate a spark electrical discharge, producing gold nanoparticles. This high voltage also creates an electric field gradient toward the grounded substrate. The voltage supplied to the stainless-steel tube is not sufficient to create a spark discharge. However, it is sufficient to create a convergence of the field lines near the bottom centre of the tube.

Nanoparticles generated in the tube in air under ambient room conditions will be affected mainly by 3 forces: the applied electric field force  $F_e$ , the charged particle inter-

action force  $F_i$  and the diffusion force  $F_d$  due to collisions with air molecules. See Figure 6.2.

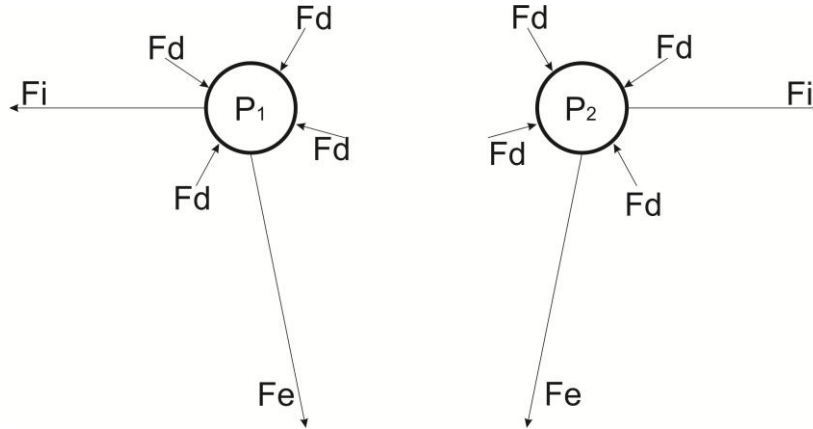


Figure 6.2 Forces on similar charged particles moving under an applied electric field in air.

The direction of the electric field force follows the gradient of the electric field, and the bulk of the field lines go from the discharging electrodes toward the grounded substrate converging at the bottom of the tube. As these particles are charged they will follow the electric field lines; however, a repulsion force is created due to the particle-particle interaction, so this repulsion force spreads the stream of particles and defocuses the beam. Also, because of the presence of air, the particles collide randomly with air molecules and a random diffusion force is created.

### 6.2.2 Diffusion of nanoparticle

The diffusion of nanoparticles in a gas was described in Einstein's study of Brownian motion [106], where the density profile of Brownian particles  $p(x, t)$  at point  $x$  in one dimension at a time  $t$  is:

$$p(x, t) = \frac{1}{\sqrt{4\pi Dt}} e^{-\frac{x^2}{4Dt}} \dots\dots (6.1)$$

where  $D$  is the diffusivity of a particle in gas taken from the Einstein–Stokes equation, which depends on the temperature  $T$  of the gas, the dynamic viscosity of the gas  $\eta$  and the radius of the particle  $r$  :

$$D = \frac{k_B T}{6\pi\eta r} \dots\dots (6.2)$$

The Einstein solution for Brownian motion describes the spatial distribution of particles in a gas with known temperature and viscosity. As an example, a 10nm particle in air at room conditions will be randomly moving and colliding with air molecules, and after 50ms, its displacement probability will be distributed as shown in Figure 6.3

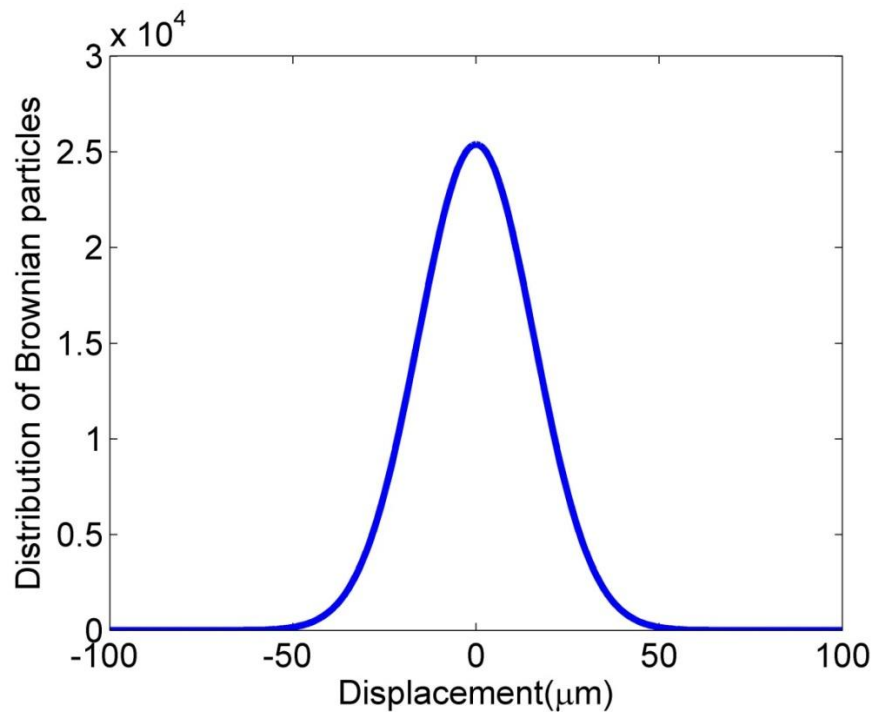


Figure 6.3 Distribution of Brownian particles due to diffusion in air.

To quantify the displacement distribution of the Gaussian profile, the full width at half maximum (FWHM) of the distribution is calculated ( $FWHM = 2\sqrt{4Dt}$ ) for the 10nm particle after 50ms, which is 44.4  $\mu\text{m}$ .



The FWHM of the distribution increases with time as shown in Figure 6.4.

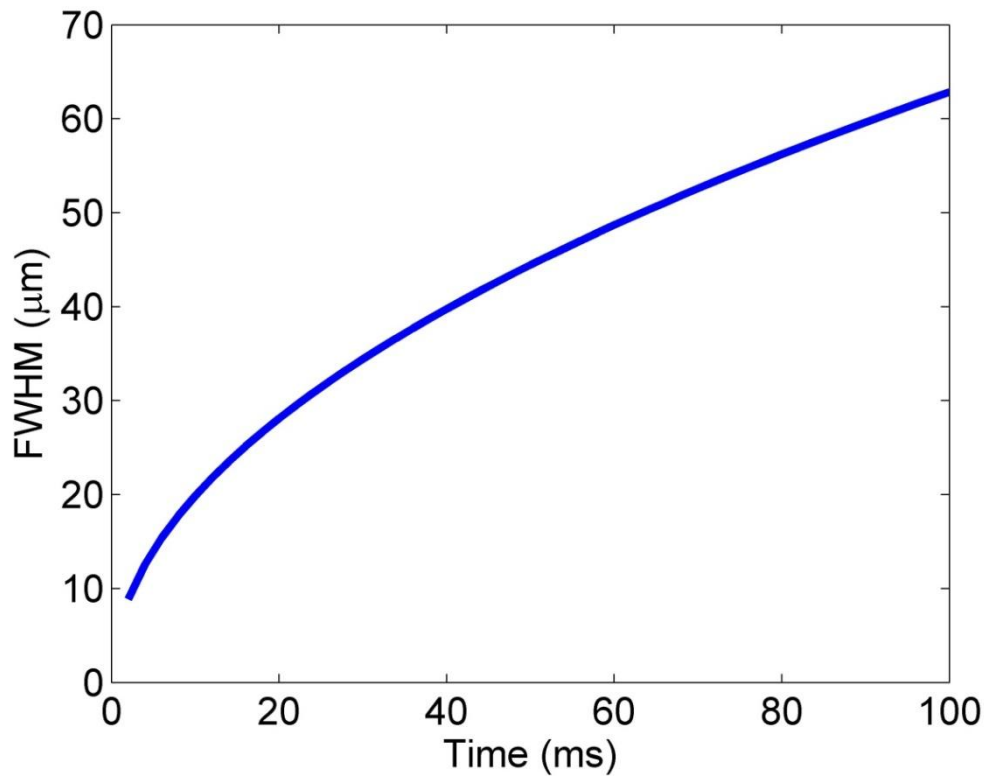


Figure 6.4 FWHM of the distribution of Brownian particles increasing with time.

This increase of the FWHM of the particle distribution with time means that, to reduce the effect of the diffusion and achieve better focussing, the transit time of the particles should be minimised.

### 6.2.3 Analysis of particle-particle interaction

The formation process of the particles by the discharge as described in section 4.4 suggests the presence of significant charge on the particles. The polarity of this charge was measured as described in section 5.3.2, and it was shown that the dominant

charge on the particles was positive. Similarly charged particles repel each other due to the Coulomb interaction force  $F_i$ :

$$F_i = k_c \frac{Q_1 Q_2}{S^2} \dots\dots\dots (6.3)$$

where  $k_c$  is Coulomb constant ( $8.89 \times 10^9$ ),  $Q_1$  and  $Q_2$  are the charges on the particles, and  $S$  is the separation between the particles. The velocity  $v$  of a particle moving under a force  $F$  in a fluid is described in Einstein-Stoke equation:

$$v = \frac{F}{6\pi\eta r} \dots\dots\dots (6.4)$$

where  $\eta$  is the dynamic viscosity of the gas and  $r$  is the radius of the particle. Substituting equation (6.3) into equation (6.4) for the force gives the velocity of the particles  $v_i$  resulting from the interaction:

$$v_i = \frac{k_c Q_1 Q_2}{6\pi\eta r S^2} \dots\dots\dots (6.5)$$

As the velocity of the particles in air represents a first order differential equation where  $v_i = \frac{dS}{dt}$ , therefore:

$$\frac{dS}{dt} = \frac{k_c Q_1 Q_2}{6\pi\eta r S^2} \dots\dots\dots (6.6)$$

Solving equation (6.6) for  $dS$  by separating the variables and integrating each side gives the separation of the particles at a particular time:

$$\begin{aligned} \int_{S_0}^S 6\pi\eta r s^2 dS &= \int_{t_0}^t k_c Q_1 Q_2 dt \\ \frac{6\pi\eta r (S^3 - S_0^3)}{3} &= k_c Q_1 Q_2 t + c \\ S^3 - S_0^3 &= \frac{k_c Q_1 Q_2 t + c}{2\pi\eta r} \end{aligned}$$

$$S = \sqrt[3]{\frac{k_c Q_1 Q_2 t + c}{2\pi\eta r}} + S_0^3 \dots\dots (6.7)$$

Applying initial conditions when  $t = 0$  ,  $S = S_0$ , we have  $c = 0$ , so equation (6.7) becomes:

$$S = \sqrt[3]{\frac{k_c Q_1 Q_2 t}{2\pi\eta r}} + S_0^3 \dots\dots (6.8)$$

Using equation (6.8), the separation between two charged particles can be calculated as the time changes. For example, Figure 6.5 shows a 10nm diameter particle with 60 elementary charges which is initially 10  $\mu\text{m}$  away from another particle that carries a similar charge. The trajectory of the particle driven by the electric field will drift with time due to the interaction force.

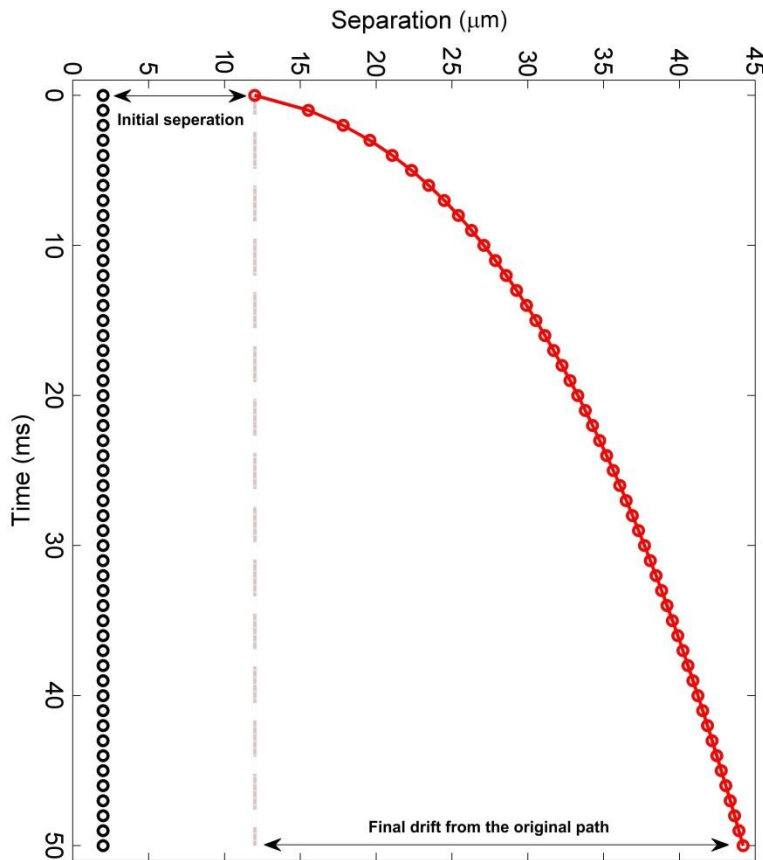


Figure 6.5 Particle drift due to charged particle interactions (60 elementary charges)

Analysing equation (6.8), the drift of a particle from its original path due to interaction forces is very influenced by the initial separation  $S_0$  of the particles, where the final drift is  $S - S_0$ .

An example of the influence of the initial separation ( $S_0$ ) on the final drift is shown in Figure 6.6 for a 10nm particle when the charge is 60 elementary charges and after 50ms in air.

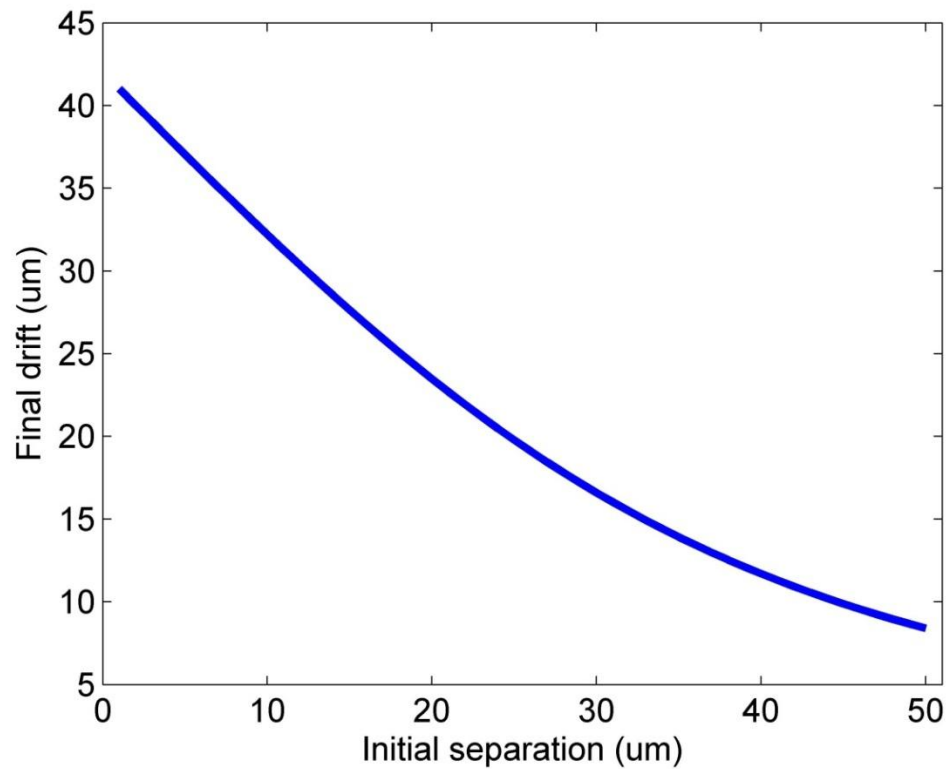


Figure 6.6 Effect of the initial separation on the final drift of a particle after 50ms in air and a charge of 60 elementary charges

The initial separation is determined by the density of particles in flight, or the number of particles generated by the discharge. From Figure 6.6, when the number of particles generated by the discharge is high, the interaction between the particles is strong, causing great deviation from the electric field lines, therefore increasing the defocussing. This shows that the deposition rate has an inverse relation to the focussing i.e. if a high deposition rate is required then the ability to focus the particle stream will be reduced.

### 6.2.4 Calculating the transit time of nanoparticles

As it appears in the diffusion calculation in equation (6.1) and particle interaction calculations in equation (6.8), the longer the transit time the more diffusion occurs and the more divergence happens due to charged-particle interactions. So studying the time that the nanoparticles take from the moment they are generated in the discharge to reach the substrate should allow for further control of the focussing of nanoparticles.

In the presence of a strong electric field, charged nanoparticles will not move in a ballistic manner but accelerate and decelerate based on the local electric field gradient in the system, and the dominant force on the nanoparticles is due to the electric field  $E$  and the charge of the particle  $Q$ , where the electric field force is ( $F = QE$ ). Therefore the velocity of particles moving in an electric field, as was used in equation (6.4) can be written as:

$$v = \frac{QE}{6\pi\eta r} \dots\dots (6.9)$$

Using the kinematic laws of motion, the distance  $d$  that an object travels with known velocity is:

$$d = \int v dt \dots\dots\dots (6.10)$$

Using a discrete form to solve the complete travel distance, by substituting equation (6.9) into equation (6.10) we calculate the transit time  $\Delta t$  between every two points in the space:

$$\Delta t = \frac{6n\pi\Delta d\eta r}{Q \sum_{i=1}^{i=n} E_i} \dots\dots\dots (6.11)$$

where  $n$  is the number of discrete values of the electric field within the distance  $\Delta d$ .

For nanoparticles generated in the spark-stream configuration shown in Figure 6.1, the transit time of the particles in air can be calculated for different charge ranges if the electric field values are known (see Figure 6.7) at different points in the focussing tube.

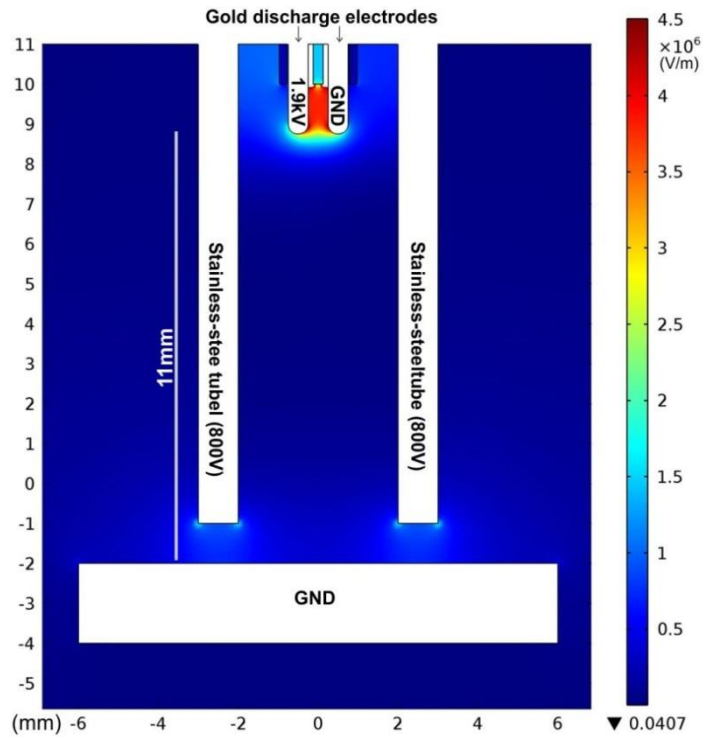


Figure 6.7 Electric field configuration for transit time calculations

As shown in Figure 6.7 below, the strong electric field on the gold electrodes generates a spark discharge and the field provides the force that is required to move the nanoparticles from the gold electrodes to the substrate. The simulation also includes a stainless-steel tube with 800V applied to it, which controls the electric field lines to follow converging paths. The electric field values of each point at the centre of the focussing tube are used to determine the transit time of the nanoparticles for a range of charge and different particle diameter values.

Figure 6.8 shows the transit time of nanoparticles of different sizes and charge values calculated using equation (6.11), where the electric field, shown in Figure 6.7, is determined from the distance between the discharge electrodes and the grounded substrate using Comsol Multiphysics simulation software.

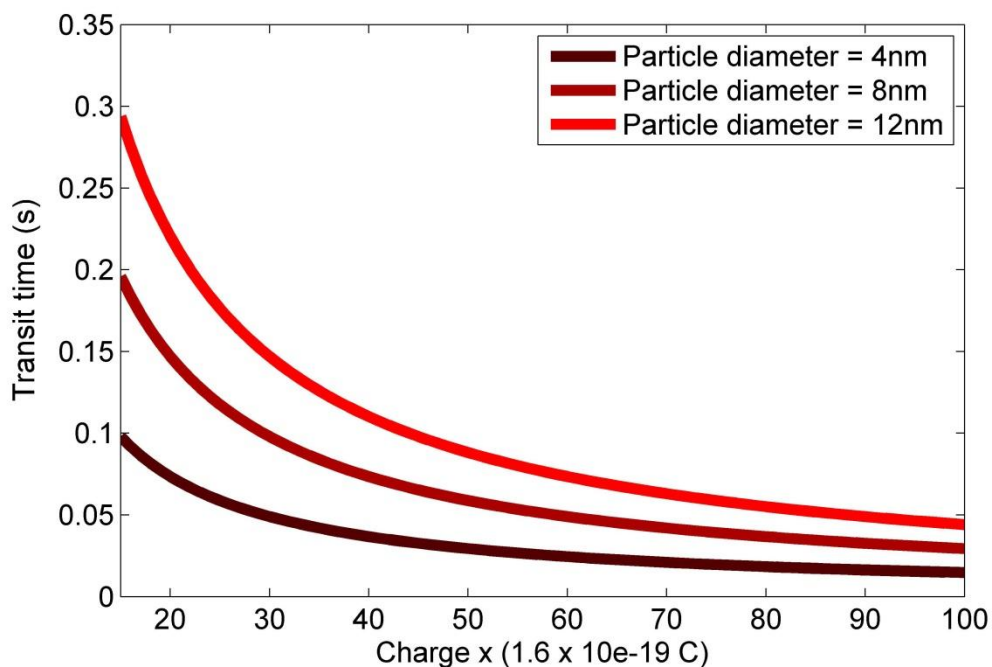


Figure 6.8 Transit time of nanoparticles with different diameters for a range of charge values

The size of the nanoparticles is estimated to be of the order of 10nm as discussed in section 5.3. However, as the charge of the particles is not actually known for our configurations, the arbitrary charge range used in Figure 6.8 requires experimental confirmation, which will be in the next section.

## **6.3 Focussing of nanoparticles experimentally**

A series of experiments was conducted to assess the effect of some of the parameters that affect the focussing of the particles, e.g. the dimensions of the focussing tube, the voltage applied to the tube and the density of particles produced. Each of these parameters was experimentally assessed, with the results leading to the focussing of gold nanoparticles produced by electrical discharge down to  $20\text{ }\mu\text{m}$  –  $50\text{ }\mu\text{m}$  spots, and the printing of different patterns controlled by software.

### **6.3.1 Effect of focussing tube voltage**

Initial experiments to demonstrate the focussing effect were carried out with and without a metallic focussing tube. The experiment was first conducted without a tube in order to show the normal spread of the nanoparticles on the substrate. High voltage pulses were applied between two  $25\text{ }\mu\text{m}$  diameter gold wires, and material was deposited over a wide area of the substrate as shown in Figure 6.9a. In a second experiment, a high voltage was applied to a  $300\text{ }\mu\text{m}$  internal diameter (ID) stainless-steel tube surrounding the gold discharge electrodes. This generated a small well-defined spot on the substrate; the diameter of the spot was approximately 15% of the internal diameter



of the tube, as shown in Figure 6.9b. This spot was generated from voltage pulses that are less than 3% of the number of pulses applied when no tube was used, which suggests that the nanoparticles that were spread across the space between the electrodes and the substrate are now confined to a small area because of the modified electric field.

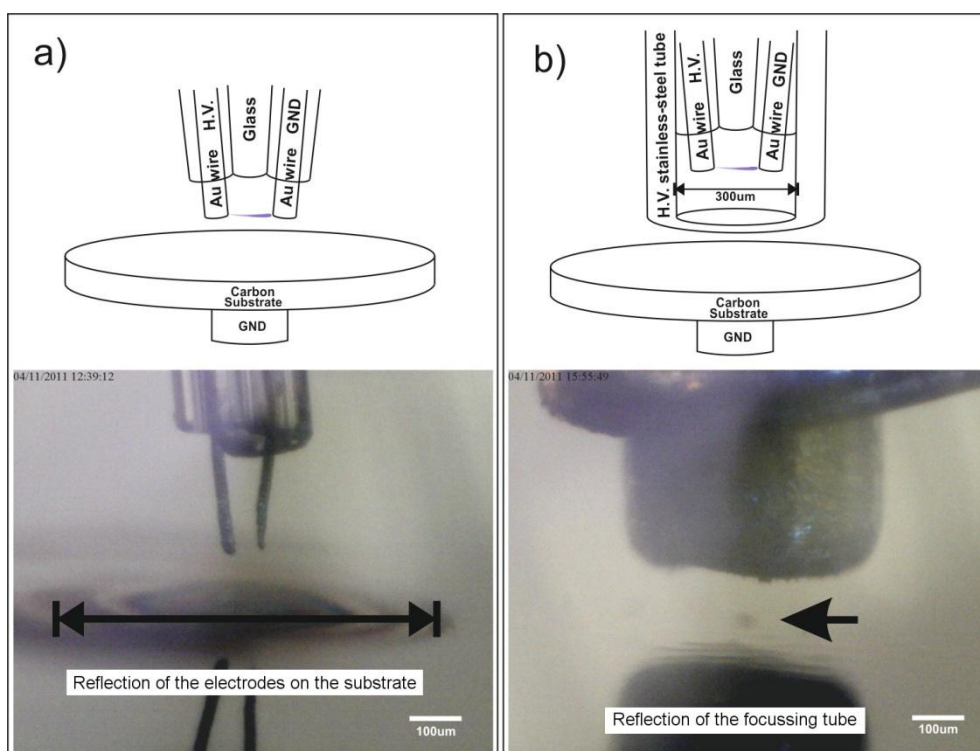


Figure 6.9 a) Deposition on substrate without using focussing tube. b) Deposition on substrate using focussing tube

To be able to analyse and quantify the effect of the focussing tube, a 4mm ID stainless-steel tube was used as shown in Figure 6.10. The voltage on the focussing tube was varied in order to see its effect on the deposited spot.

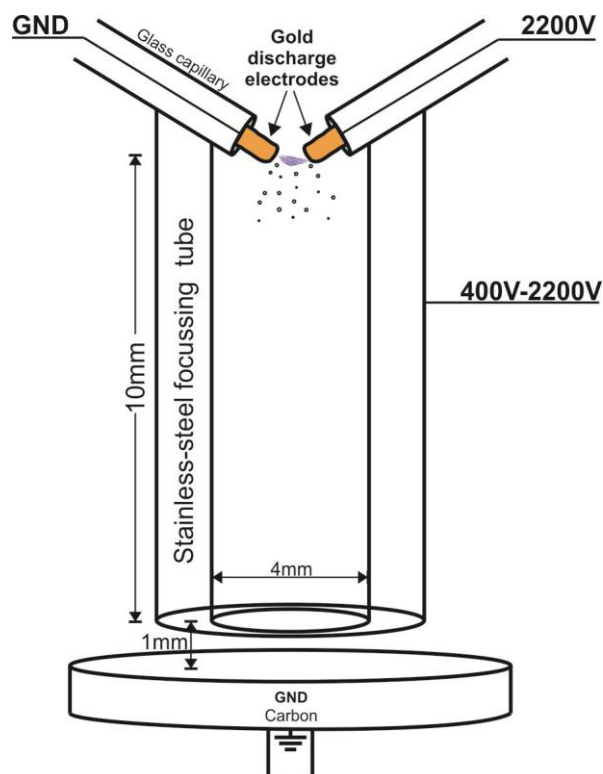


Figure 6.10 Schematic diagram of the tube voltage analysis apparatus

The discharge voltage was supplied from a high voltage amplifier in the form of 100ms square wave pulses with 50% duty cycle. The high voltage supply to the discharge electrodes was set in parallel with a 300 pF capacitor (not shown in Figure 6.10). Two 0.5mm diameter gold electrodes were used, and the gap between the electrodes was approximately 0.5mm. The voltage supplied to generate a spark discharge was +2.2kV and the experiment was performed in air. The voltage on the stainless-steel tube was varied from 400V to 2200V, supplied from a DC high voltage power supply.

Figure 6.11 shows spots of different sizes deposited on carbon substrates using different tube voltages; the spot size (arrowed) decreases as the voltage applied to the focussing tube increases.

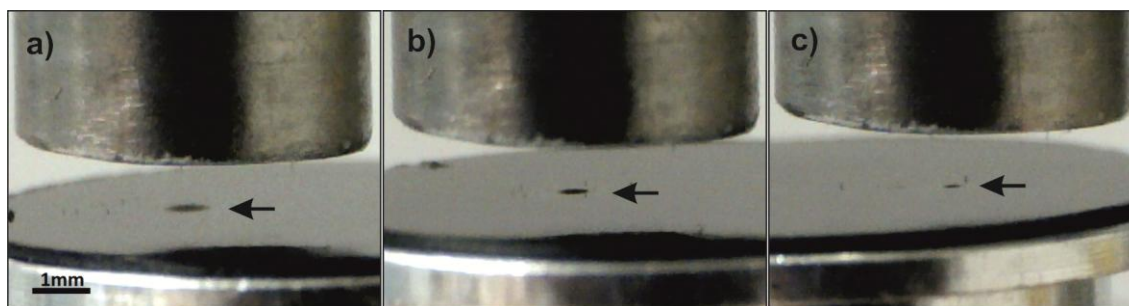


Figure 6.11 Deposited spots using a) 400V focussing tube, b) 1200V focussing tube, c) 1800V focussing tube

Optical micrographs of the deposited spots were analysed by evaluating the variation of the image grey level across each spot. The results of different spot intensity profiles are shown in Figure 6.12.

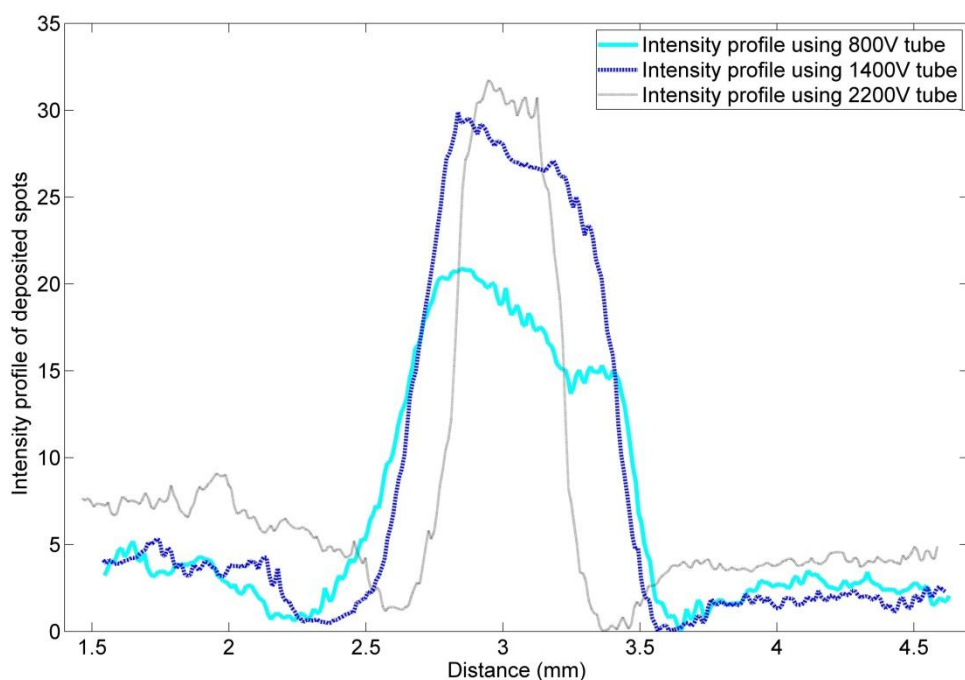


Figure 6.12 Intensity profiles of deposited spot images for different tube voltages

To illustrate the effect of the tube voltages on the size of the deposited spots, the full width at half maximum FWHM of the grey level profiles are plotted against the voltage

applied to the tube, see Figure 6.13. The right hand axis shows the FWHM spot size as a percentage of the diameter of the focussing tube; error bars reflect the ripple level in the grey level profile of the spots.

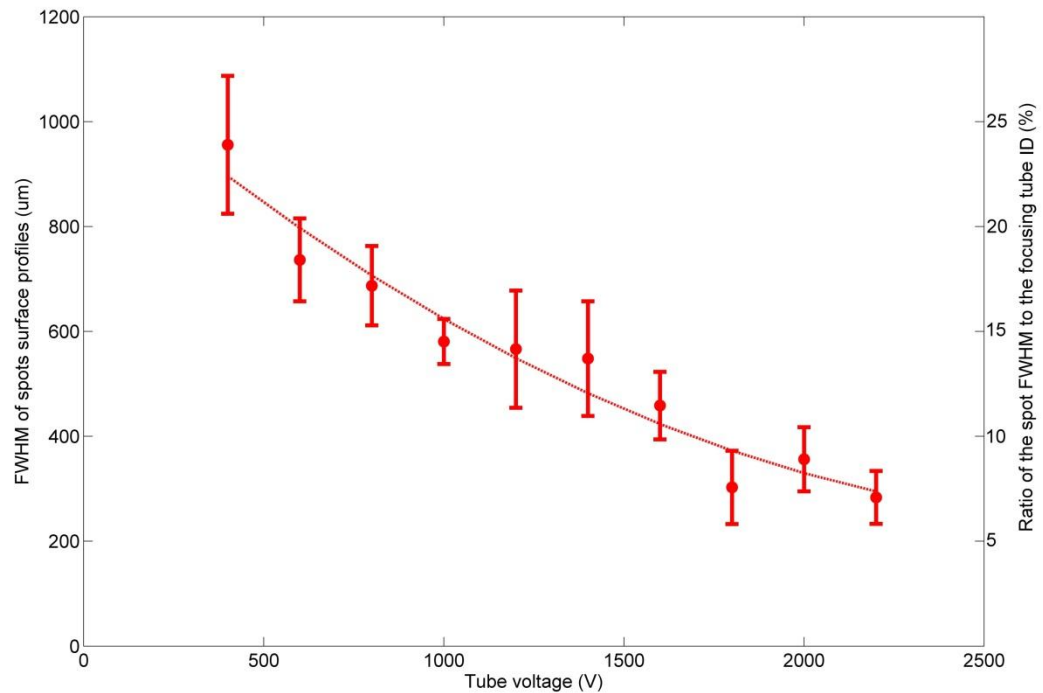


Figure 6.13 FWHM of the deposited spots intensity profiles

Voltages higher than 2200V were on the verge of causing a discharge between the focussing tube and the grounded gold electrode, so the voltage supply range was stopped at that level.

The results in Figure 6.13 show one of the major advantages of the spark-stream focussing technology, which is the ability to deposit spots that are smaller than the depositing nozzle (the focussing tube in this case). In the configurations used above, the spot diameter that was achieved was around 10% of the focussing tube diameter.

### 6.3.2 Measuring transit time and particle charge experimentally

The transit time calculations discussed in section 6.2.4 used a hypothetical charge range to calculate the range of transit time for the particles to travel from the discharging electrodes until reaching the substrate.

Looking at equation (6.11) for measuring the transit time:  $\Delta t = \frac{6n\pi\Delta d\eta r}{Q \sum_{i=1}^n E_i}$ , the variables of the equation are available except for the charge and the transit time, so a method was needed to find at least one of the two missing variables, transit time or charge, in order to complete the calculation.

The transit time range calculated in section 6.2.4 suggests a possibility to measure the transit time using a mechanical apparatus. The idea is to use a spinning substrate with a known angular velocity, and synchronise the nanoparticle generation to one position of the rotation. The deposited nanoparticles are then analysed based on their position on the substrate, which can then be translated into the time domain.

To measure the transit time of the nanoparticles, the spinning substrate was placed 1mm under the stainless-steel focussing tube (10mm long), and high voltage pulses were triggered at one specific rotational position of the substrate as shown in Figure 6.14.

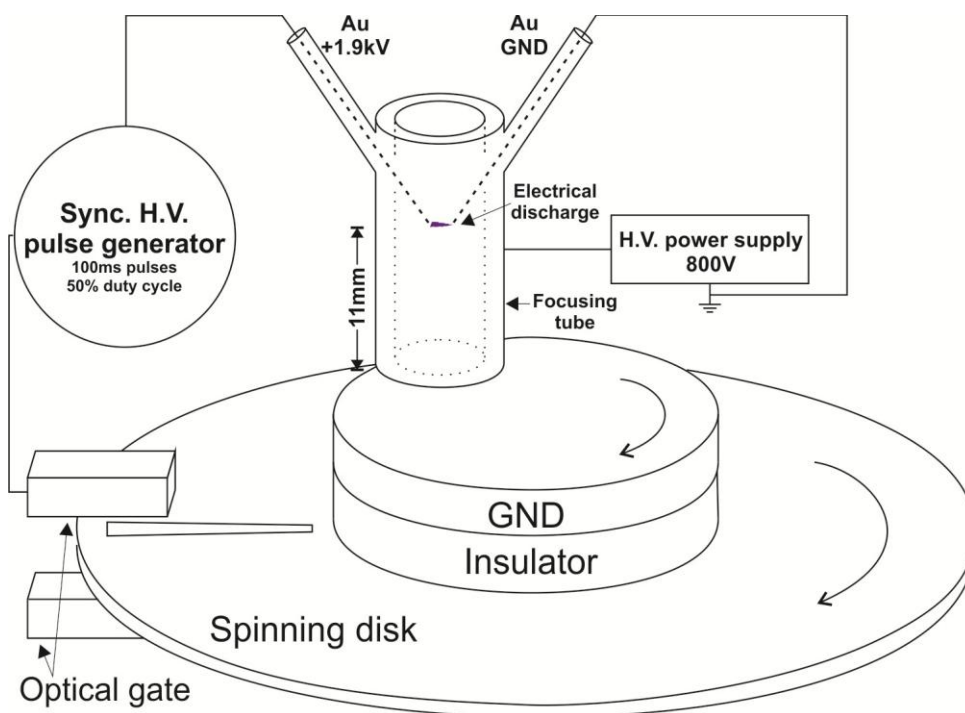


Figure 6.14 Schematic diagram of transit time measurement apparatus

The time taken to complete one rotation of the substrate was set to 210ms, which was measured after trying other longer times/slower rotation, where around 200ms for one spin was found to give a well distributed deposition on the substrate. The HV pulse width was 50ms, the discharge voltage was set to 1.9kV, and the tube voltage was 800V. A single 50ms pulse was triggered at the beginning of each complete substrate rotation and 3000 rotations were triggered, this was sufficient to deposit enough material on the substrate to conduct the analysis.

By analysing the deposition pattern using an SEM, as shown in Figure 6.15, it was found that the deposition starts at around 20ms after the discharge trigger, with the

highest density of deposition appearing at around 55ms. Thereafter, the deposition diminishes until the end of the spinning cycle.

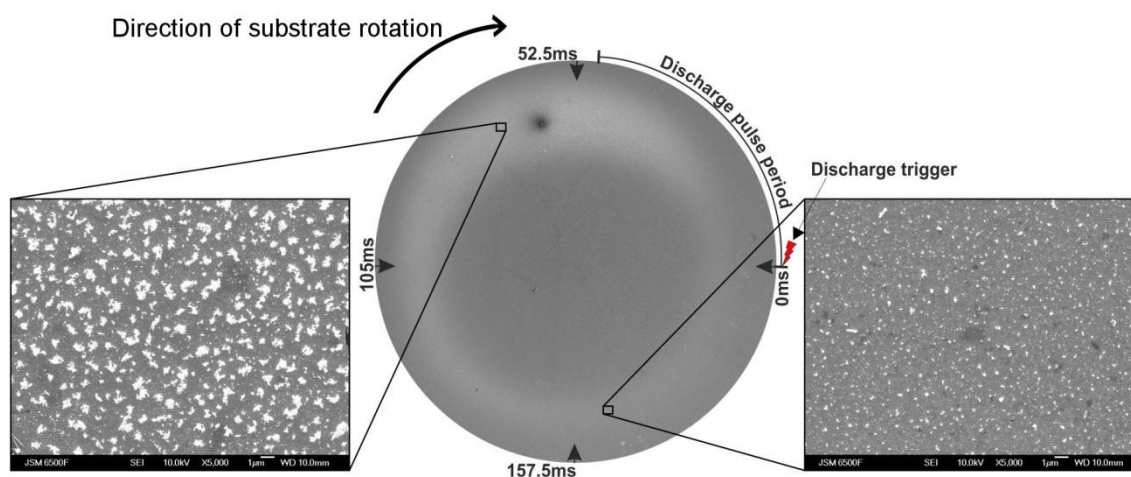


Figure 6.15 SEM graphs of the deposited gold nanoparticles on a pulse-synchronised spinning substrate.

The dark spot at the top of the deposition ring is a contamination that occurred after the experiment.

To analyse the transit time of the nanoparticles, high resolution SEM micrographs were obtained at different positions within the deposition pattern shown in Figure 6.15. The number of particles in each micrograph was computed assuming an average primary particle diameter of 10nm, and from these the density of the deposited nanoparticles was measured and shown in Figure 6.16 (dashed lines). The grey level of the deposition ring shown in Figure 6.15 (middle graph) is used to confirm the distribution of the density of particles, where high a density of particles appears brighter, see Figure 6.16.

The range of transit times shown in Figure 6.16 can be used to estimate the charges of the nanoparticles using equation (6.11) for calculating the transit time.

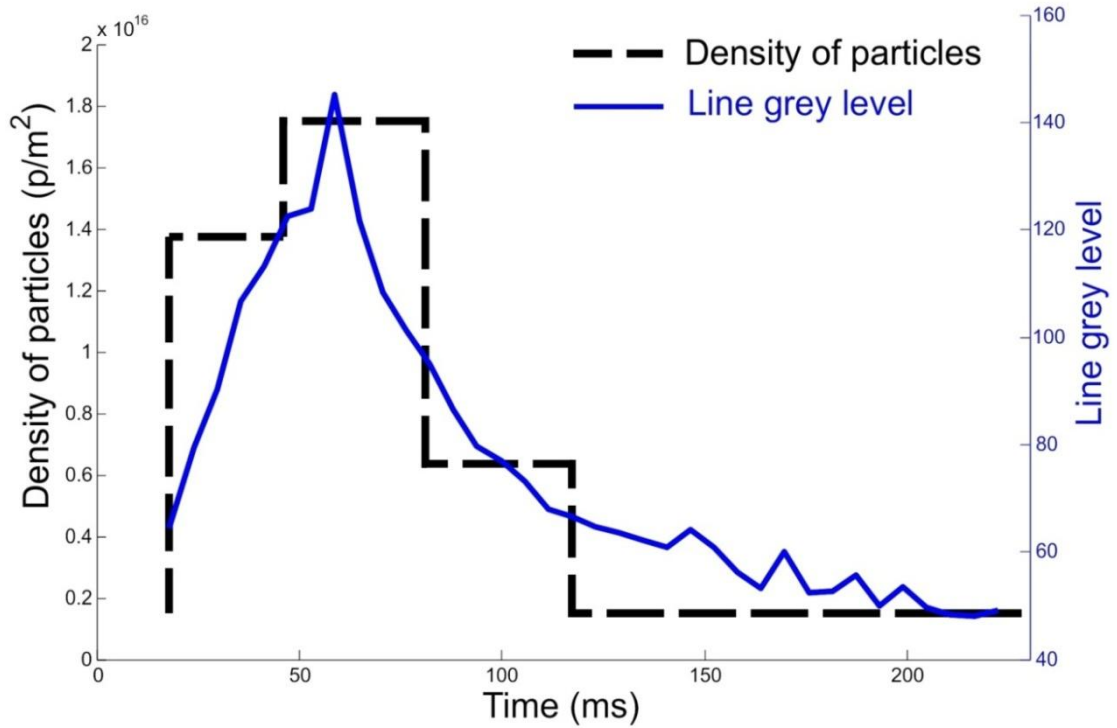


Figure 6.16 Density of particles as a function of transit time.

The distribution of charge for each assumed particle size can be estimated by applying the experimental distribution of transit time to the transit time equation (6.11) using the density profile of the particles. Using these experimental data and the electric field calculations shown in Figure 6.7, the charge of the particles becomes the only unknown, and it can be determined for different particle sizes. Figure 6.17 shows a histogram of the charge of the nanoparticles based on their size using the theoretical and experimental results of this study.



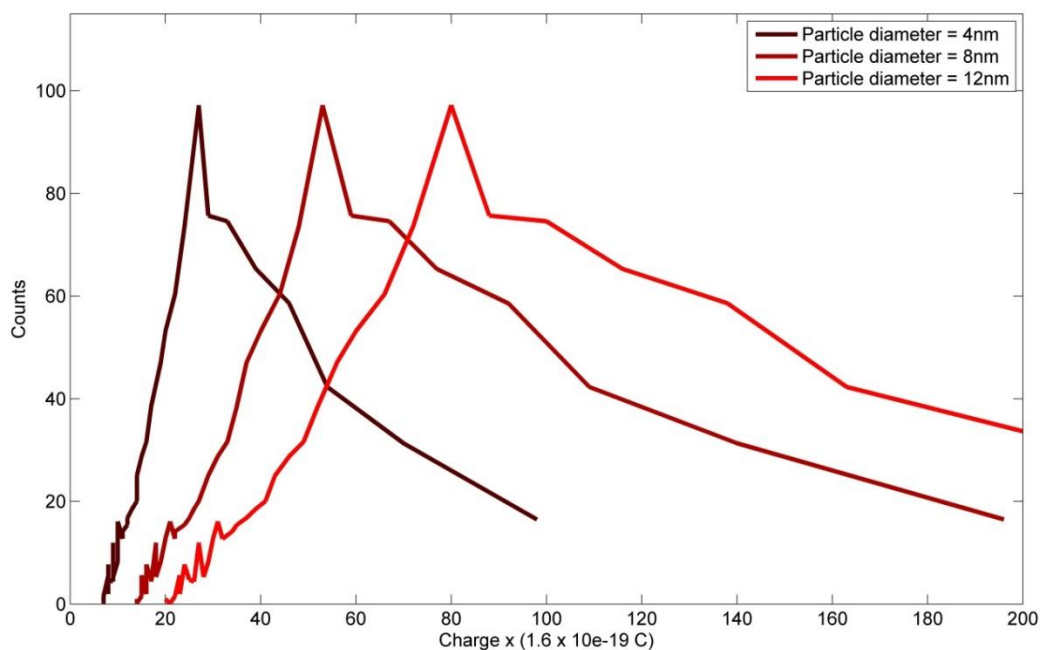


Figure 6.17 Histogram of the elementary charges for each particle size.

To assess the validity of the estimated charge, the highest theoretical charge that a particle could carry can be calculated from the Rayleigh charge limit.

The Rayleigh limit as discussed in section 2.2 describes the maximum charge a liquid droplet can hold before it becomes unstable [36].

The Rayleigh charge limit depends on the surface tension of the liquid and the radius of the droplet as described in equation (2.3) in chapter 2.

When the particles are in the formation stage, and gold vapour is condensing to form nanoparticles in the liquid state, the maximum charge that a gold droplet would be able to carry can be calculated using Rayleigh limit.

The surface tension of molten gold is reported to be approximately 1100mN/m [107,48], and the Rayleigh charge limit for that surface tension can be calculated for different droplet diameters as shown in Figure 6.18.

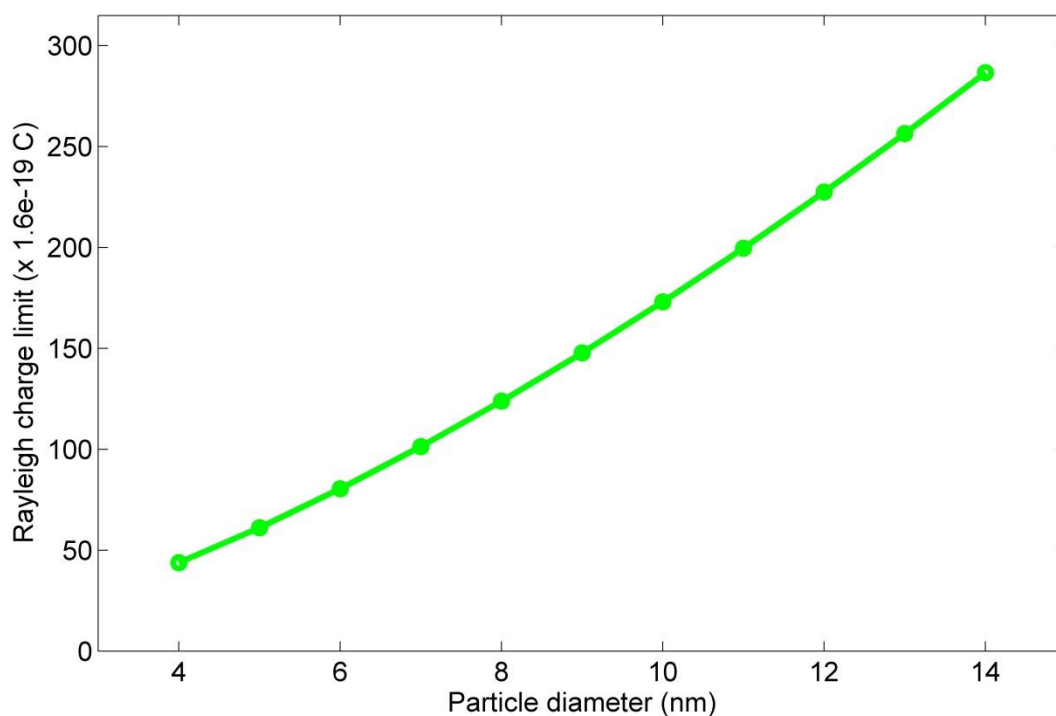


Figure 6.18 Maximum charge of particles for different particle diameter.

Comparing the theoretical charge limit shown in Figure 6.18 with the estimated charge for each particle size shown in Figure 6.17, for the 4nm, 8nm and 12nm particle sizes, the Rayleigh charge limit is 44, 124 and 228 elementary charges, respectively. This shows that the peaks of the charge histogram shown in Figure 6.17 for each size are well within the Rayleigh charge limit.

### **6.3.3 Effect of diffusion and particle interaction investigated experimentally**

The effect of the diffusion and particle interaction was assessed experimentally using different sets of experiments. The transit time experiment that showed a range of 20ms-200ms travel time and described in section 6.3.2 demonstrates the effect of diffusion on the particles. This transit time in vacuum is  $40 \mu s$  calculated for 10nm gold particles using classical laws of motion knowing the acceleration from the electric field force for the same configuration of charge and electric field used in the transit time experiment. The difference between the two time regimes is due to the damping factor from the diffusion of particles in air.

On the other hand, the effect of the particle-particle interaction can be assessed experimentally by varying the density of the generated particles, which would change the initial separation  $S_0$  between the particles and therefore affect the focussing behaviour and spot size.

The first set of experiments was conducted to assess the effect of the spark frequency on the spot size. The spark frequency refers to the charging and discharging of the capacitor across the discharge electrodes. The capacitor charges up when the high voltage is first turned on and the voltage across it ramps up; when the voltage reaches the breakdown threshold of air a discharge occurs, and the charge stored in the capacitor is discharged (Figure 6.19).

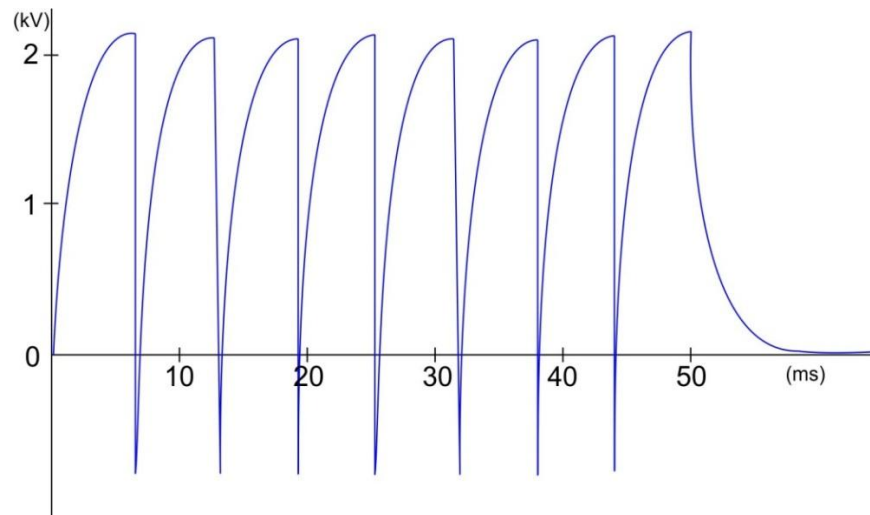


Figure 6.19 Voltage across the capacitor as it charges and discharges.

When the frequency is increased, the rate of deposition increases as the erosion of the electrodes increases [79], which leads to a higher density of particles.

Experimentally, varying the spark discharge frequency increased the deposition spot diameter as shown in Figure 6.20.

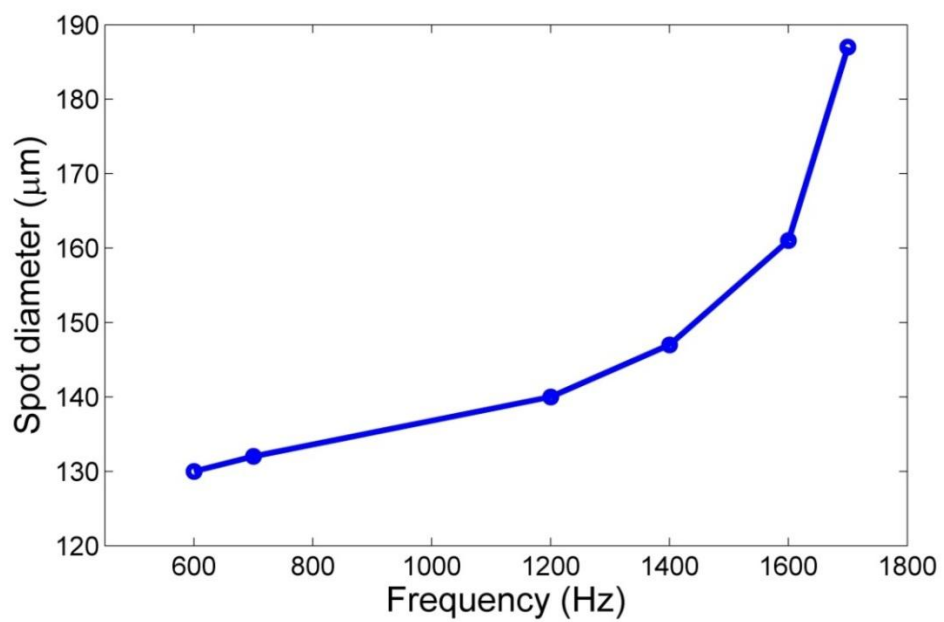


Figure 6.20 The effect of the spark frequency on the deposition spot diameter.

The configurations for this set of experiments were 1.2 kV between the discharge electrodes supplied for 5 seconds, electrodes were 500  $\mu\text{m}$  diameter gold wires separated by 500  $\mu\text{m}$ , 45 pF capacitor was used and 700 V DC was connected to an 800  $\mu\text{m}$  diameter stainless-steel focussing tube.

During the experiments the spark frequency was the only parameter that was varied. By increasing the spark frequency, the density of produced particles increases. This could explain the increase of the deposition spot diameter when the density of particles increases the particle-particle interaction increases, which raises the defocussing effect and increases the diameter of the deposited spot.

Another approach reported to increase the density of particles is by increasing the value of the capacitor across the discharge, which leads to an increase in the energy stored in the capacitor and fed to the discharge [79]. This raises the erosion rate of the electrodes and therefore increases the density of particles in the space.

A number of experiments were conducted to assess the effect of the capacitor value on the spot diameter. Figure 6.21 shows the increase of spot size as the capacitor value increases for different tube voltages using 4mm diameter focussing tube, a fixed spark frequency and a fixed discharge voltage.

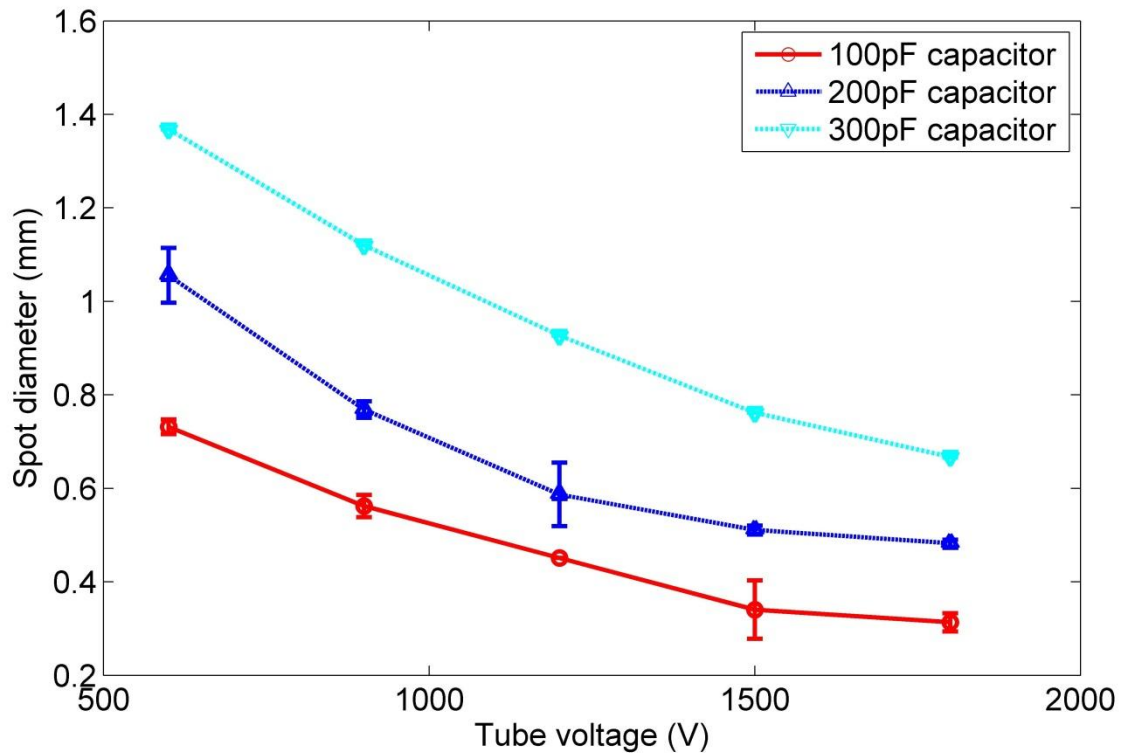


Figure 6.21 The effect of the capacitor value on the spot diameter.

The effect of the particles interaction, particularly the initial separation between the particles or the density of the particles on flight suggests that to achieve higher focussing results the density of the particles in flight should be lowered. This shows a trade-off between the deposition rate and the focussing of the nanoparticles.

## 6.4 Microstructure and patterns deposition

In order to be able to print microstructures, and shape high resolution patterns, the spot diameter has to be reduced. The previous theoretical and experimental analyses show that many parameters are involved in reducing the spot diameter. Scaling down

the focussing tube dimensions will narrow the electric field trajectories as the internal diameter of the focussing tube is reduced, and it will also reduce the transit time of the particles as the length of the tube is shortened, hence the diffusion and the particle interaction effects will be reduced.

To test these observations, a 3mm long and 0.8mm ID tube was used to deposit sets of spots from gold electrodes using different capacitor values with different focussing tube voltages. The results of these experiments, with the other results from experiments using a 4 mm ID tube are shown in Figure 6.22.

To be able to print simple patterns, the substrate was placed on motorized translation stages for X, Y and Z axes, and using a 0.5mm ID tube (1.5 mm long), 100 pF capacitor, 350 V on the

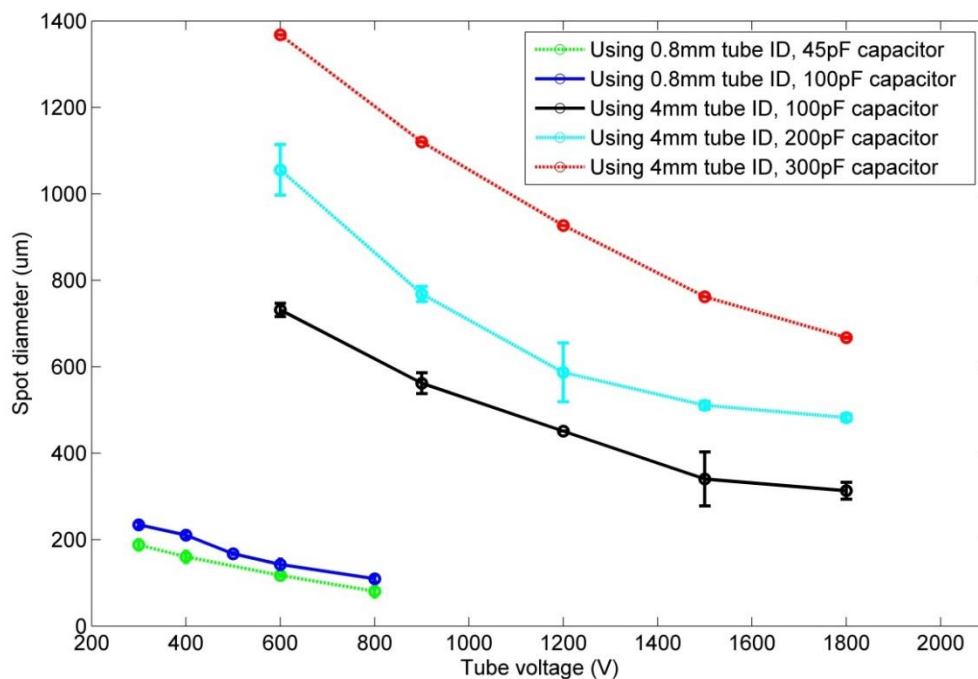


Figure 6.22 Effect of scaling down the focussing tube on the spot diameter

focussing tube and 650 V for the discharge using 25  $\mu\text{m}$  gold wire electrodes, it was possible to form a simple gold deposition pattern of parallel lines as shown in Figure 6.23.

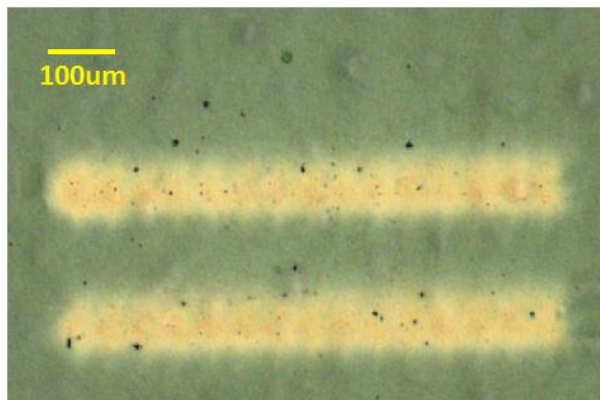


Figure 6.23 Gold deposition of parallel lines printed using a 0.5mm focussing tube with 350 V applied to it.

To scale down the deposited feature further and implement direct writing of different patterns, motorised translation stages were used with a software programmed to read bit-map images and instruct the stages to deposit patterns following the coordinates from the software. A tube diameter of 0.5 mm and length of 1.1 mm was used. Voltages were 500 V on the focussing tube and 600 V for the discharge electrodes, and the capacitor value was 100 pF. Figure 6.24a shows the software coordinates of a pattern (ORC), and Figure 6.24b shows the pattern as printed.



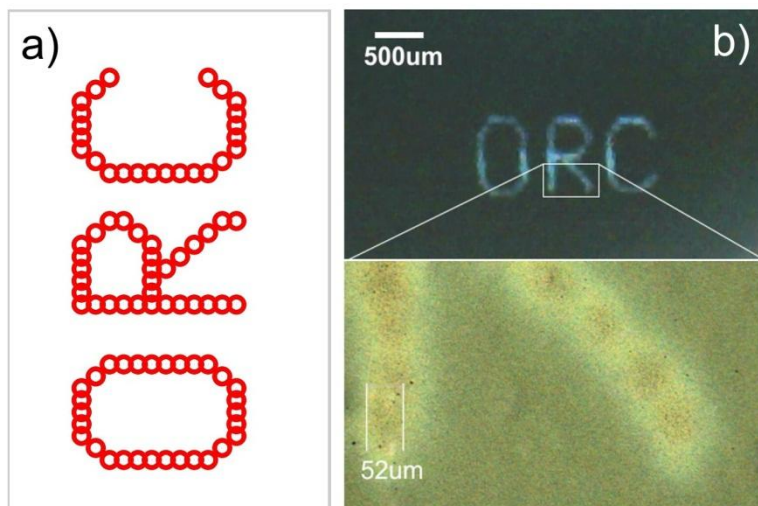


Figure 6.24 a) pattern coordinates sent to the stages, b) pattern printed using a 0.5 mm ID focussing tube (1.5 mm long) with 500 V applied to it.

Further experiments were conducted using the same apparatus concept but with focussing tube dimensions scaled down. It was possible to deposit 31  $\mu\text{m}$  diameter spots using a 350  $\mu\text{m}$  ID focussing tube ( $\sim 1.5$  mm long), with a 30 pF capacitor and 700 V on the tube. Also spots with diameters below 20  $\mu\text{m}$  were demonstrated as shown in Figure 6.25 using 25  $\mu\text{m}$  diameter gold wire electrodes inside a 210  $\mu\text{m}$  ID focussing tube ( $\sim 1$  mm long) with a 45 pF capacitor and 600 V on the tube.

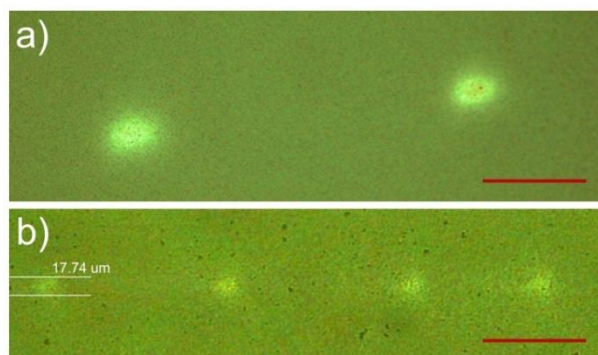


Figure 6.25 a) gold deposition using 0.35 mm ID focussing tube ( $\sim 1.5$  mm long), b) deposition using 0.21 mm focussing tube ( $\sim 1$  mm long), (100  $\mu\text{m}$  scale bars)

Details of the printing configurations for these experiments and other previously described ones are summarised in Table 6.1.

Table 6.1 Summary of the configurations used to deposit microscale spots.

Spot dia.	Tube dia.	Tube leng.	Cap. value	Tube volt.	Discharge volt.
668 $\mu\text{m}$	4mm	10mm	300pF	1800 V	2200 V
483 $\mu\text{m}$	4mm	10mm	200pF	1800 V	2200 V
313 $\mu\text{m}$	4mm	10mm	100pF	1800 V	2200 V
110 $\mu\text{m}$	0.8mm	3mm	100pF	800 V	1000 V
81 $\mu\text{m}$	0.8mm	3mm	45pF	800 V	1200 V
52 $\mu\text{m}$	0.5mm	1.5mm	100pF	500 V	600 V
31 $\mu\text{m}$	0.35mm	~1.5mm	30pF	700 V	1200 V
18 $\mu\text{m}$	0.21mm	~1mm	45pF	600 V	1200 V

Scaling down the apparatus further than the listed above was very challenging. However, other possible configurations could be used to scale down the spots, which will be described in the Further Developments chapter. Studies have confirmed the possibility to focus nanoparticles generated by electrical discharge to reach submicron scales [83,84]. This has been demonstrated by pre-patterned masks using lithographical methods as shown in Figure 6.26. This highlights the possibility to achieve submicron spots using spark-stream technology for direct write purposes.

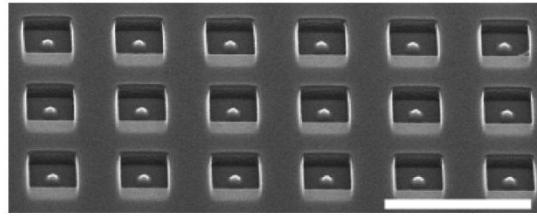


Figure 6.26 Copper nanoparticles are focussed inside photoresist PR pre-patterned mask from ref. [84] (scale bar is  $1.5\ \mu\text{m}$ )

## 6.5 Conclusion

Using spark-stream direct write technology, it was possible to deposit gold nanoparticles in air to form spots of the order of  $20\ \mu\text{m}$  using a  $210\ \mu\text{m}$  ID focussing tube ( $\sim 1\text{mm}$  long).

This was achieved by studying the parameters involved in the focussing mechanism of the nanoparticles generated by electrical discharge in air. Parameters including the dimensions of the focussing apparatus, where the length of the focussing tube affects the transit time of the particles, and the diameter of the focussing tube affects the convergence of the nanoparticles. The transit time is of great importance from the theoretical analysis of the forces involved in controlling the nanoparticles trajectories, namely the diffusion of the particles and the interaction between charged particles.

The study of these two phenomena led to a better understanding of the parameters affecting the particles' trajectories in order to control their effect and focus nanoparticles to micro-scale structures.

Direct write of different patterns was demonstrated using spark-stream technology. Computer software was programmed to coordinate motorised translation stages to read bit-map images and deposit gold nanoparticles following the patterns in the image.

The focussing concept of nanoparticles can be scaled down further to achieve nanoscale deposition, as has been demonstrated in studies used pre-patterned masks to implement focussing. This strongly suggests the ability of spark-stream technology to direct write nanoscale patterns by reducing the dimensions of our focussing apparatus further, and by implementing other focussing configurations, as will be described in the further developments chapter.



## **Chapter 7**

### **7. Further developments**

#### **7.1 Introduction**

Direct write technologies investigated in this research have been used to deposit glass and metal under ambient conditions. However many aspects of these technologies require further study.

Although EHD was limited to a low surface tension glass (borate glass), further manipulation of the experimental conditions might allow one to use other higher surface tension glasses. This might be achieved by suppressing the electrical discharge using a different gas instead of air, or by working in air but at slightly lower pressure using small gaps as will be described in this chapter.

In spark-stream technology, the focussing configuration has been simplified by using a single metallic focussing tube. However, other configurations could be used to increase the focussing effect and/or produce smaller spots by further manipulating the electric field lines. Also, as electrical discharge is mainly used to produce nanoparticles of various metals, using other materials in spark-stream technology would be an important investigation for future work.

Since it is a method to deposit nanoparticles in confined areas, spark-stream technology could be used to incorporate metal nanoparticles inside glass fibres, as will be discussed in this chapter.

## 7.2 Further development on EHD

Although EHD was conducted successfully on molten boron trioxide glass, the fact that electrical discharge interrupts the EHD process for higher surface tension materials highlights the need to suppress the electrical discharge in order to operate at the higher voltages required to print higher surface tension materials.

Using gases other than air could increase the electrical breakdown threshold. Sulphur hexafluoride  $\text{SF}_6$ , for instance, has a very high breakdown threshold when compared to air or nitrogen [108,109]; in fact, adding only 1% of  $\text{SF}_6$  to nitrogen increases the breakdown voltage by 30%, as shown in Figure 7.1 [108].

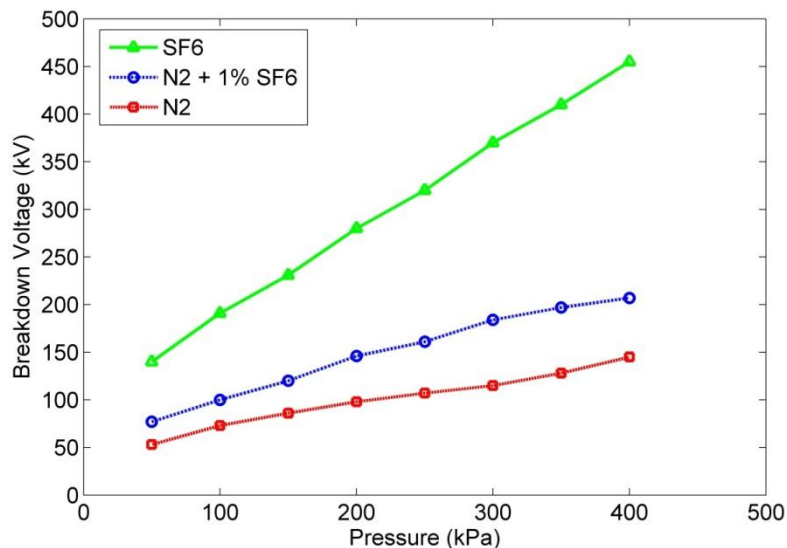


Figure 7.1 A comparison between the breakdown voltages for nitrogen, sulphur hexafluoride  $\text{SF}_6$  and a mix of 1% of  $\text{SF}_6$  with  $\text{N}_2$  [108]

Another approach to avoid electrical discharge while conducting EHD experiments with higher surface tension liquids is to operate at pressures lower than atmospheric with small gaps.

As was shown in sections 3.3 and 3.4, operating EHD at small gaps below  $10\ \mu\text{m}$  produced jetting borate glass strands. The Paschen curve describes the relationship between the breakdown voltage of a gas and the gap-pressure product. The curve shows that lowering the pressure of the air to only 10% of the ambient pressure at small gaps allows operation at significantly higher breakdown voltages, as shown in Figure 7.2.

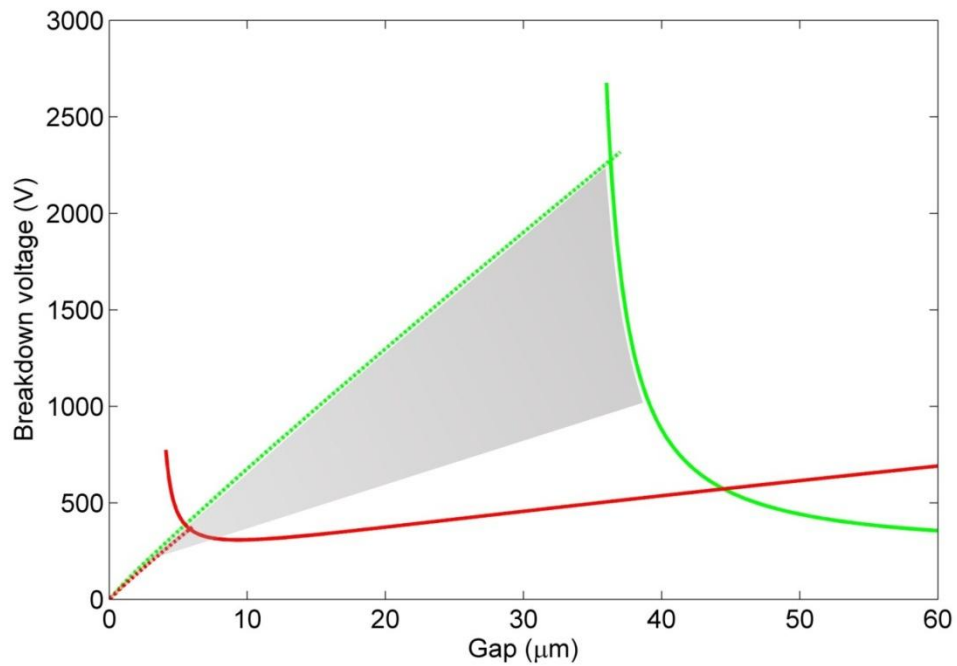


Figure 7.2 Paschen curve (—) and Field emission threshold (---) under ambient pressure are compared to Paschen curve (—) and Field emission threshold (---) at 10 kPa pressure for short gaps between the electrodes. Shaded area represents a potential experimental region.



The solid green line in Figure 7.2 represents the breakdown threshold of air at medium vacuum (10 kPa) as calculated from Paschen equation, and the dashed green line represents the field emission threshold at the same pressure. This shows that the electric field in the triangular shaded area between the green and red lines could be advantageous to implement EHD experiments, either to work on larger gaps for convenience, or to work in small gaps but at higher voltages in order to conduct experiments on higher surface tension materials.

To assess the effect of these predictions, the electric field is calculated from the voltage of the field emission threshold divided by the gap values at medium vacuum pressure, and the result is then compared to the electric field from the Paschen breakdown voltage over the gap values under ambient pressure as shown in Figure 7.3.

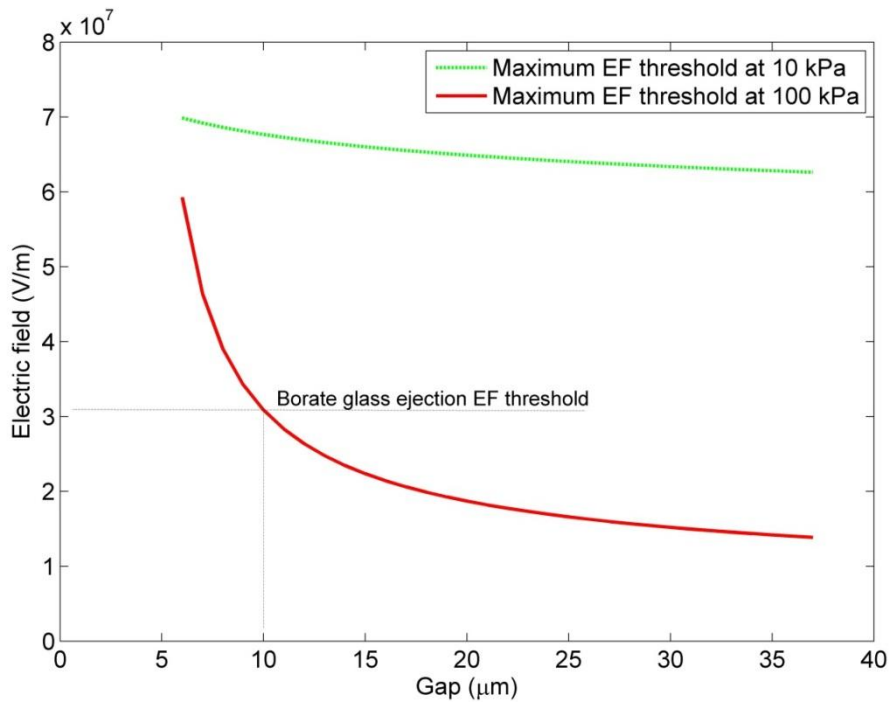


Figure 7.3 Electric field calculated for the potential operating gaps at 10 kPa and at 100 kPa.

From the experimental results on boron trioxide at ambient pressure, molten glass ejection happened when the gap was around  $10\text{ }\mu\text{m}$ , so the electric field at that point is  $31\text{ MV/m}$ . At the same gap value for  $10\text{ kPa}$  pressure, the maximum electric field that could be used in an EHD experiment is around  $67\text{ MV/m}$  which is more than double the electric field value at ambient pressure. This high electric field is proportional to the square root of the surface tension as described in section 2.3 ( $V_o \propto \sqrt{\gamma}$ ); this could enable materials with surface tension values as high as  $370\text{ mN/m}$  to be printed which includes many glasses like tellurite and silicate glasses. From this analysis, when operating at small gaps, a relevantly small reduction in the pressure could allow for the use of much higher surface tension materials in EHD experiments.

### **7.3 Other spark-stream focussing configurations**

In spark-stream technology, the configuration used to focus the nanoparticles was a simple focussing tube that manipulates the electric field lines in order to converge them as they move towards the substrate. However, other configurations could be used to manipulate the electric field lines in order to achieve additional focussing.

An example of another focussing configuration that was investigated briefly is the use of different potentials at different axial positions to focus the particles, as shown in Figure 7.4.

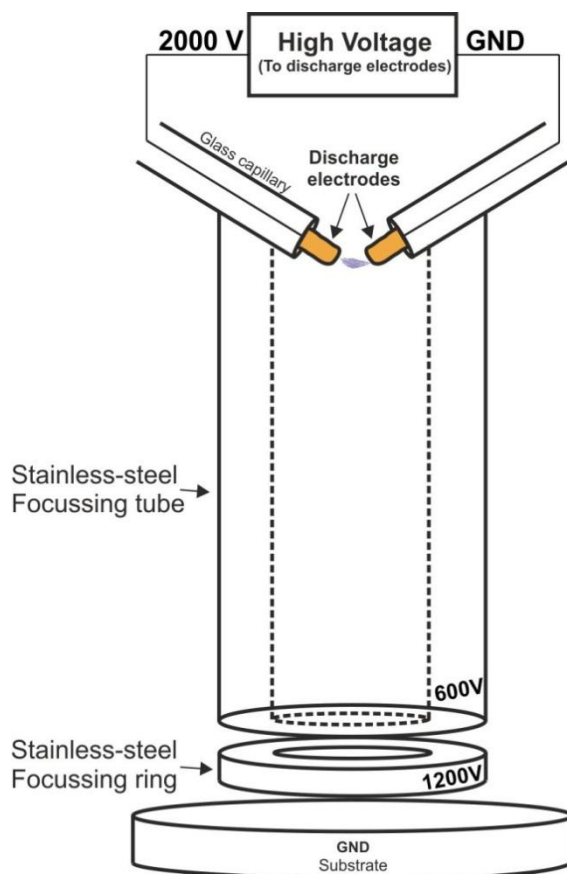


Figure 7.4 Illustration of the tube-ring focussing configuration

The potential applied to the focussing tube can now be different from the potential applied to the ring below it. The idea of this configuration is that the use of a lower potential at the tube will minimise the particle interaction defocussing effect.

Since nanoparticles interact and repel in flight, and this repulsion is influenced by the separation between the particles as described in section 6.2.3, if the particles were to be more widely-separated whilst they move from the electrodes to the substrate, and then rapidly converge under the influence of the field lines just before the substrate, the defocussing effect of the particle-particle interaction will be reduced as the separation between the particles is relatively large most of time.

To verify this hypothetical analysis, a few experiments were conducted using a 4mm internal diameter stainless-steel ring under the focussing tube as shown in Figure 7.5.

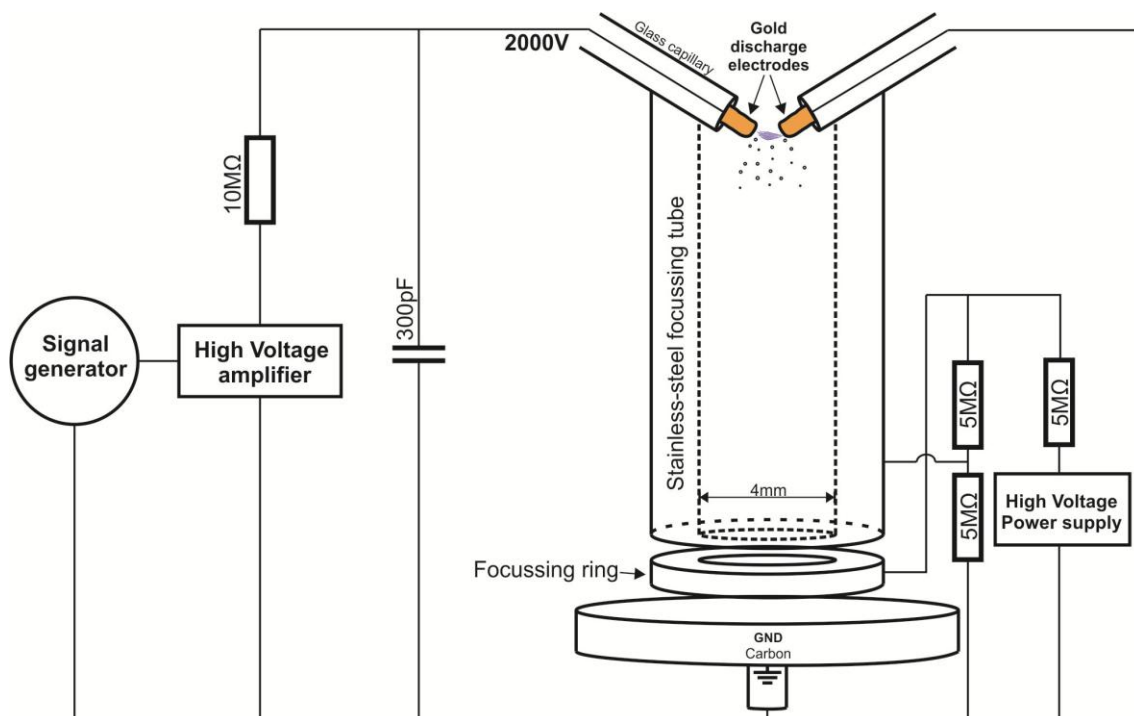


Figure 7.5 Schematic diagram of the tube-ring focussing configuration

The voltage applied to the focussing tube was set to be half the voltage applied to the focussing ring. Both voltages were varied and the deposition spot diameter was analysed. As shown in Figure 7.6, when compared to the spot diameter from only a single focussing tube using similar voltage and capacitance configurations, the spot diameters using the tube-ring configuration are smaller.

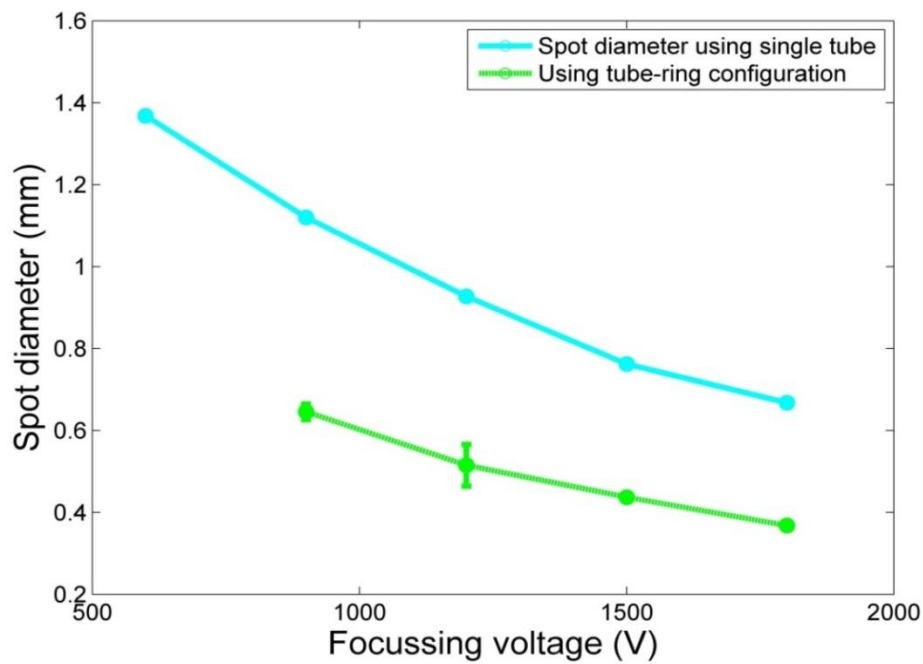


Figure 7.6 Spot size comparison between single tube and tube-ring focussing configurations

The focussing voltage in Figure 7.6 is the ring voltage in the case of the tube-ring configuration, while the tube voltage is set to half the ring voltage. In the case of a single focussing tube configuration the potential applied to the tube is the same along its entire length.

The aim of this set of experiments is to demonstrate the potential of using different focussing configurations to increase the focussing effect further. Other configurations, for instance a sequence of rings with different focussing voltages could enable the manipulation of the field gradient as shown in Figure 7.7, and give further control over the focussing of the particles.

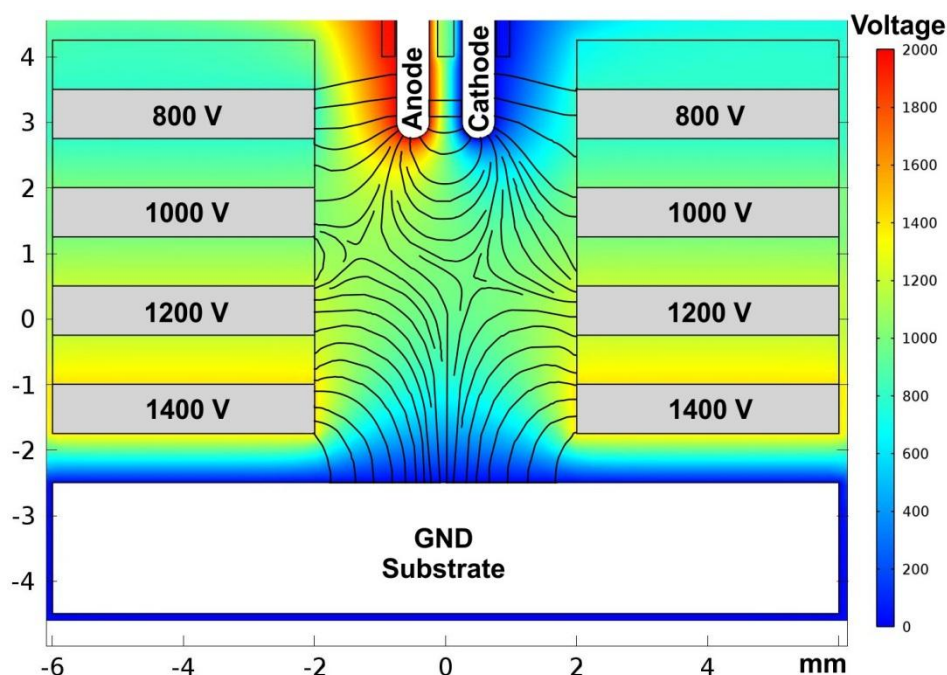


Figure 7.7 Electric potential gradient and electric field lines of the ring-sequence focusing configuration

## 7.4 Electrodes of different materials

One of the major features of using electrical discharge in spark-stream technology is its ability to erode metals with different melting temperatures, so a wide range of materials could be a potential future development area.

Generating nanoparticles from silver [110,111], copper [112], silicon [113,81,114], palladium [111], platinum [110,111] and carbon [115,116] using electrical discharge has been well reported in the literature. However, in order to avoid oxidation of the nanoparticles as they are produced from vapour, gases other than air must be used. Alternatively, an appropriate choice of the gas around the discharge could be used to deliberately produce nitrates [117] or oxides of metals [116].

Bimetallic nanoparticles could be also produced using spark-stream technology. By using different electrode materials as shown in Figure 7.8, Ag-Pt nanoparticles were readily produced by electrical discharge [110].

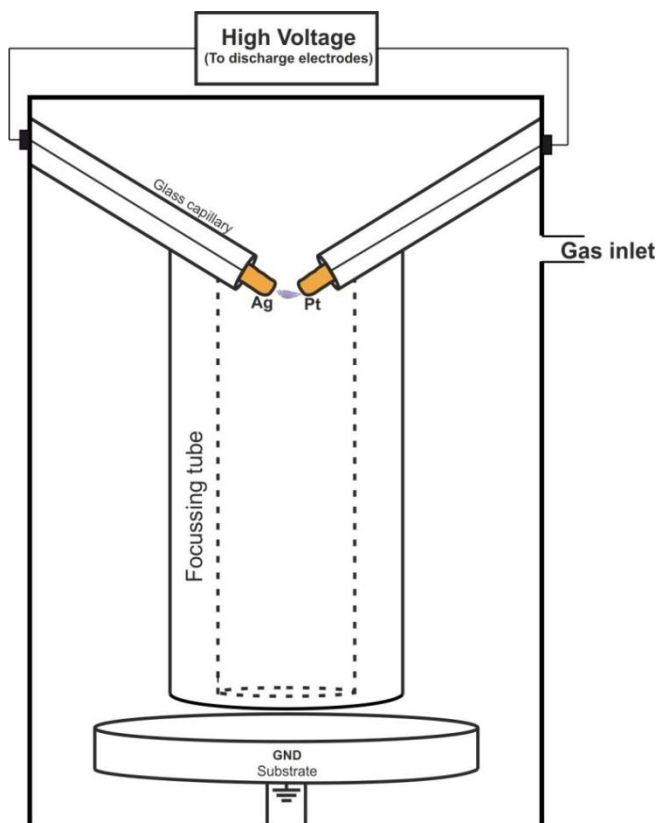


Figure 7.8 Spark-stream apparatus to produce bimetallic nanoparticles

Manipulating the material of the electrodes as well as the gas around the discharge can thus produce a diverse range of nanoparticles that are difficult to produce by other means.

Although nanoparticles of different materials produced by electrical discharge are believed to acquire an electric charge and hence follow the field line, the particles' tendency to follow the field lines would vary depending on the size of the particles and the charge they acquire. Therefore, a focussing comparison between nanoparticles of different materials produced using spark-stream technology could be of great interest.

## **7.5 Incorporating nanoparticles inside hollow fibres**

Spark-stream technology produces a stream of nanoparticles that could be inserted in small geometry structures. This fact highlights the potential to use spark-stream technology to incorporate nanoparticles inside the core of a glass fibre.

Incorporating metal nanoparticles inside glass fibre produces an optical nonlinearity which can be employed in the development of optical waveguides and switches [118,119,120]. Also metal nanoparticles are widely used for chemical and biological sensing [121,122,123], which raises the need for a robust and scalable method to incorporate metal nanoparticles inside glass fibres.

Incorporating metal nanoparticles inside glass fibres is normally done through complex modified chemical vapour deposition (MCVD) techniques [119,124]. Another method reported is to splice two fibres which have nanoparticles deposited on their tips [118]. However, the complexity of these methods limits their use and applications.

Using the spark-stream technology concept, nanoparticles might be directly written inside a glass fibre while it is being drawn, as shown in Figure 7.9.



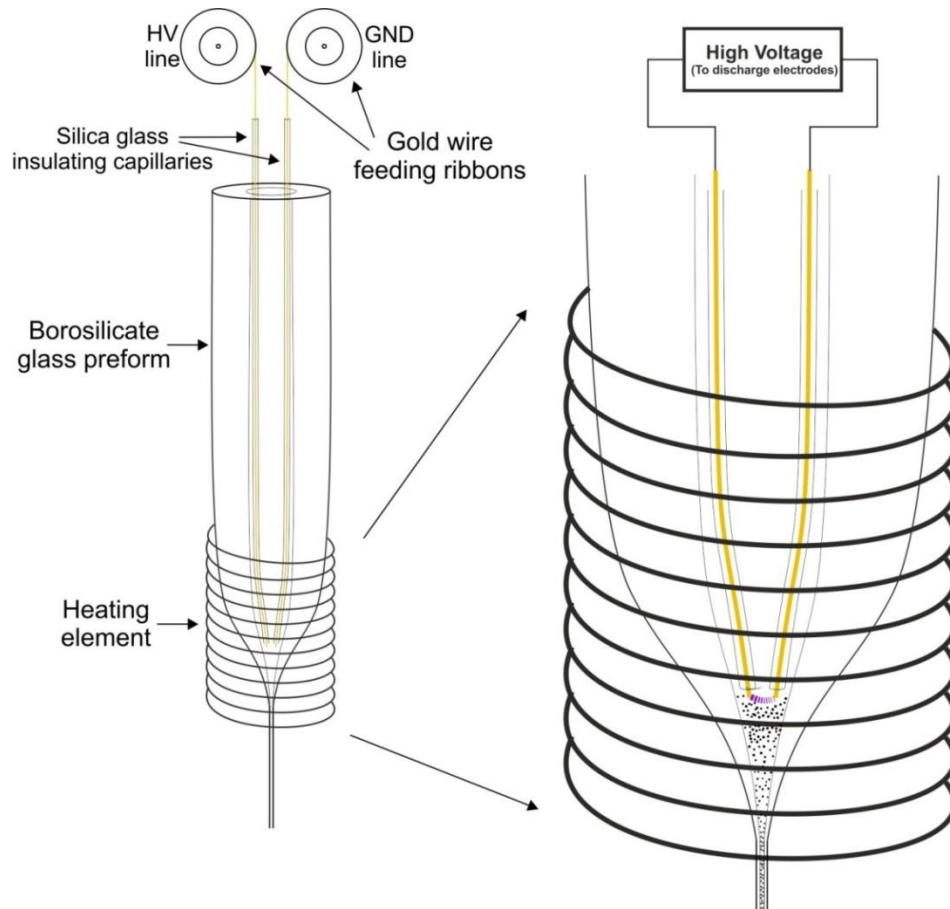


Figure 7.9 Setup for incorporating gold nanoparticles inside a glass fibre using the spark-stream technology concept

In this illustration, gold nanoparticles are generated from a spark discharge between two gold wires fed inside the core of a hollow glass preform as it is being drawn. The produced nanoparticles are densely incorporated at the tapered part of the glass preform, and as the glass stretches the nanoparticles are distributed within the core of fibre in real time.

A match between the nanoparticles material and the glass in use has to be considered, particularly the thermal properties. In this example, as gold nanoparticles are pro-

duced, the softening point of the glass preform used has to be lower than the melting point of the gold nanoparticles in order to avoid melting the particles after they are deposited.

## 7.6 Conclusion

Investigating EHD and spark-stream technologies further shows the potential to overcome challenges that appeared during the research. Working in medium vacuum at small gaps has a great potential to conduct EHD using higher electric field values in order to deposit materials of higher surface tension values than borate glass, like tellurite and some silicate glasses. Theoretical analysis of the electric field at 10 kPa pressure in air suggests that it would be possible to conduct experiments at more than double the electric field value of air under ambient pressure using a 10  $\mu\text{m}$  gap.

Using different focussing configurations in spark-stream technology has the potential to increase the focussing effect. A tube-ring configuration consisting of a metallic ring under the focussing tube showed a reduction of around 40% of the spot size when the voltage of the ring was double the voltage of the tube. This initial demonstration shows a promising potential to investigate other focussing configurations, like a sequence of rings, for instance.

Different materials can be used in the spark-stream technology, and further study of the focussing effect of different materials will be an area of future investigation.

Finally, as spark-stream technology is a direct write deposition method and is able to produce metal nanoparticles in small areas, incorporating nanoparticles inside a hollow fibre could be done using the technology by discharging two metal wires inside a glass preform as it is being drawn, generating nanoparticles of the metal and depositing it at the inner walls of the fibre core.

---

## List of publications and conferences

- Saleh E, Praeger M, Vaughan A S, Stewart W, Loh W H, 2012, *The direct writing and focusing of nanoparticles generated by an electrical discharge*, Journal of Nanoparticle Research, 14:1220
- Saleh E, Praeger M, Vaughan A S, Stewart W, Loh W H, 2013, *Transit time and charge of gold nanoparticles generated by electrical discharge in ambient air conditions*, Journal of Nanoparticle Research, (Submitted, full manuscript can be found in Appendix 4)
- Praeger M, Saleh E, Vaughan A, Stewart W, Loh W, 2012, *Fabrication of nanoscale glass fibers by electrospinning*, Applied Physics Letters, 100:063114
- Saleh E, Praeger M, Vaughan A S, Stewart W, Loh W H, 2012, *GlassJet printer for metals and glasses*, ORC Industrial day, Southampton, UK (Poster)
- Praeger M, Saleh E, Vaughan A, Stewart W, Loh W, 2012, *Direct write techniques for nano or micro-fabrication of high melting point materials*, Annual EPSRC Conference on Manufacturing the Future, Loughborough, UK
- Praeger M, Saleh E, Vaughan A, Stewart W, Loh W, 2012, *Electrospinning of glass nanofibres*, IOP conference on Electrospinning, Principles, Possibilities and Practice, London, UK



# Appendices

## Appendix 1: EHD onset voltage equations

Equations used to calculate the EHD onset voltage shown in Figure 1.1 are as follows:

### - Xiong's equation:

The onset voltage  $V_0$  required to eject material in EHD from Xiong's equation is calculated as follows:

$$V_0 = \sqrt{\frac{\gamma r_1}{\varepsilon_0 \tan(\alpha)}} \ln \left( 2 + 2 \frac{d}{r_1} - \sqrt{\left( 2 \frac{d}{r_1} + 1 \right) \left( 3 + 2 \frac{d}{r_1} \right)} \right) \dots\dots (A1.1)$$

where  $\gamma$  is the surface tension of the liquid,  $r_1$  is the radius of the emitting capillary,  $\varepsilon_0$  is the permittivity of free space,  $\alpha$  is Taylor cone angle and  $d$  is the distance between the tip of the liquid meniscus and the substrate.

The equation is derived from the equilibrium between the surface tension stress and the electric field stress, which occurs just before the EHD jetting:

$$\frac{2\gamma}{r_1 \tan(\alpha)} = \frac{\varepsilon_0 E^2}{2} \dots\dots (A1.2)$$

hence:

$$E = 2 \sqrt{\frac{\gamma}{r_1 \varepsilon_0 \tan(\alpha)}} \dots\dots (A1.3)$$

The electric field at the tip of the liquid cone just before a jetting occurs is calculated as follows:

$$E = \frac{2V_0}{r_1 \ln \left( 2 + 2\frac{d}{r_1} - \sqrt{\left(2\frac{d}{r_1} + 1\right)\left(3 + 2\frac{d}{r_1}\right)} \right)} \dots\dots (A1.4)$$

Substituting equations (A1.3) and (A1.4) for the electric field  $E$  gives the onset voltage:

$$V_0 = \sqrt{\frac{\gamma r_1}{\varepsilon_0 \tan(\alpha)}} \ln \left( 2 + 2\frac{d}{r_1} - \sqrt{\left(2\frac{d}{r_1} + 1\right)\left(3 + 2\frac{d}{r_1}\right)} \right)$$

#### - Si's equation:

The onset voltage from Si's equation as described by Krpoun [40] was used to show the trend of the  $V_0$  as a function of the surface tension, and to compare the results with other onset voltage calculations:

$$V_0 = \sqrt{\frac{\gamma R_c}{\varepsilon_0}} \frac{\ln \left[ \frac{R_c + 2d + 2\sqrt{d(d+R_c)}}{R_c} \right]}{\sqrt{1 + \frac{R_c}{d}}} \dots\dots (A1.5)$$

where  $\gamma$  is the surface tension of the liquid,  $R_c$  is the radius of the emitting capillary,  $\varepsilon_0$  is the permittivity of free space and  $d$  is the distance between the tip of the liquid meniscus and the substrate.

## Appendix 2: Paschen curve and field emission equations

Details of Paschen curve and field emission graphs shown in Figure 3.3, Figure 3.4 and Figure 7.2 are as follows:

### - Paschen curve equation:

Paschen curve shown in section 3.3 describes the breakdown voltage  $V_B$  of gases:

$$V_B = \frac{B (pd)}{\ln(pd) + \ln\left(\frac{A}{\ln\left(1 + \frac{1}{\gamma_i}\right)}\right)}$$

As discussed in section 3.3,  $p$  is the pressure of the gas and  $d$  is the gap distance between the electrodes.  $A$  and  $B$  are Paschen curve coefficients, determined experimentally, and depend on the molecular properties of the gas. For air,  $A = 13.4$  and  $B = 329$  [58]. Townsend's second ionization coefficient  $\gamma_i$  describes the number of electrons  $n_{sec}$  ejected per incident ion  $n_{ion}$ ; and is determined as ( $\gamma_i = 0.01$ ) [57,60]:

$$\gamma_i = \frac{n_{sec}}{n_{ion}} \dots\dots (A2.1)$$

### - Field emission equation:

The field emission breakdown voltage shown in Figure 3.4 and Figure 7.2 is calculated as follows [57]:

$$V_b = \frac{d(D_{FN} + Bp)}{\ln(KApd)} \dots\dots (A2.2)$$



where  $K$  is a fitting constant which is experimentally determined ( $K = 10^7$ ) [57], and  $D_{FN}$  is the electric field threshold required for field emission and is a function of the cathode material and surface properties as follows:

$$D_{FN} = (6.85 \times 10^7) \frac{\phi^{1.5}}{\beta} \dots\dots (A2.3)$$

where  $\phi$  is the work function of the cathode material (assumed  $\phi = 4 \text{ eV}$ ) and  $\beta$  is the geometric enhancement factor determined by Go ( $\beta = 50$ ) [57].

### Appendix 3: Au nanoparticle deposition resistance

The circuit used to measure the resistance of the gold nanoparticle deposition was built in-house as shown in Figure A3.1.

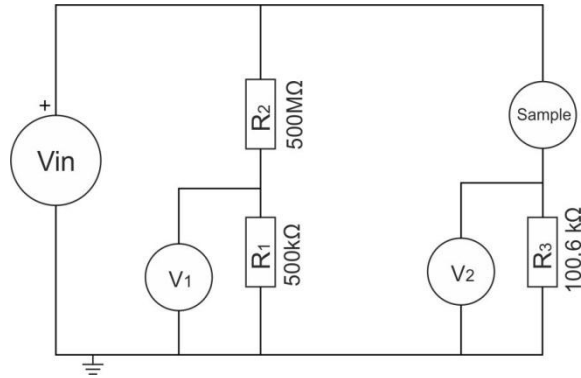


Figure A3.1 Deposition resistance measurement circuit diagram

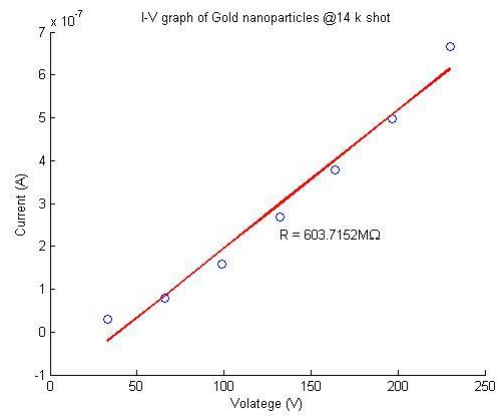
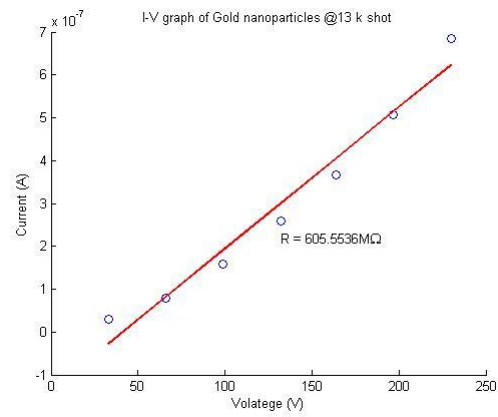
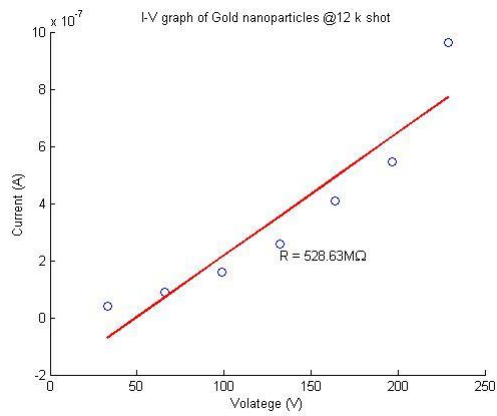
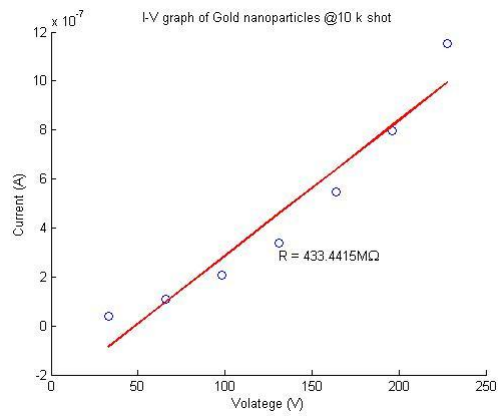
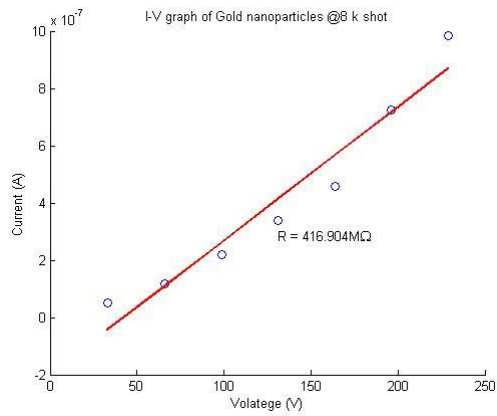
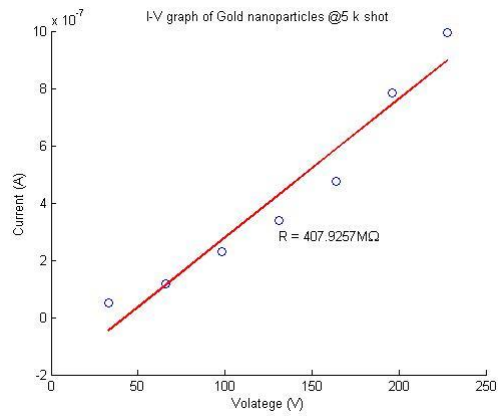
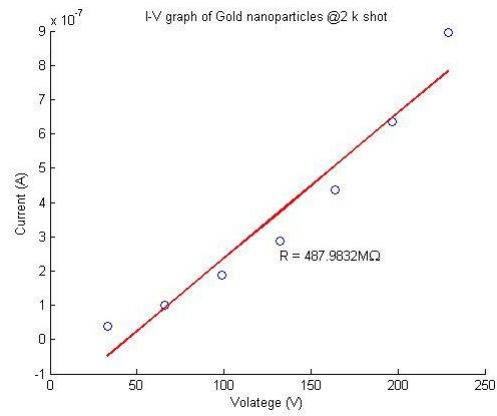
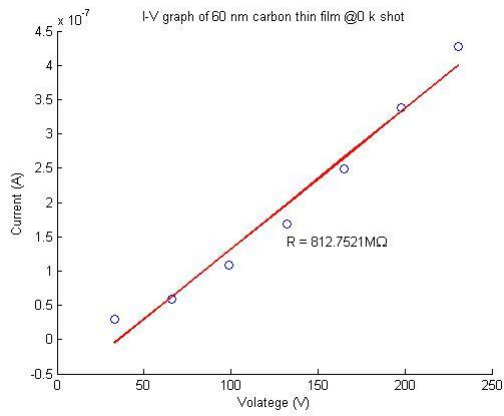
The voltage  $V_s$  across the sample (nanoparticle deposition) is measured by subtracting the voltage  $V_2$  from the voltage across the potential divider ( $R_1$  and  $R_2$ ):

$$V_s = V_1 \left( \frac{R_2}{R_1} \right) - V_2 \dots\dots (A3.1)$$

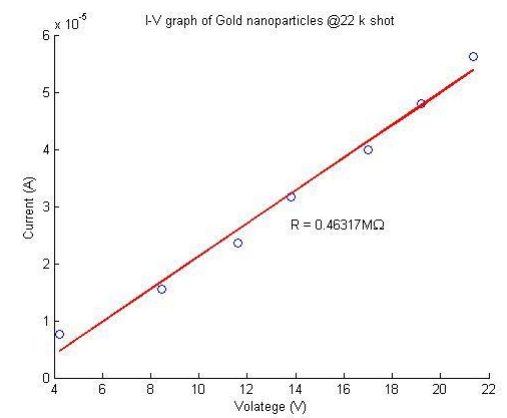
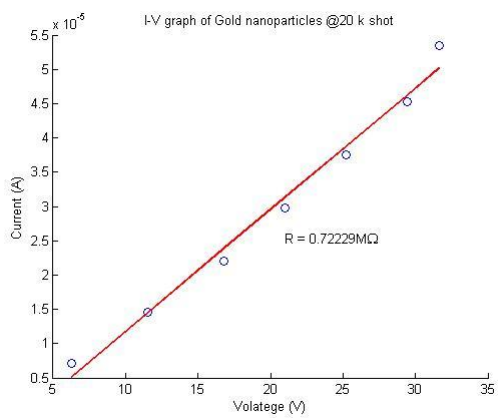
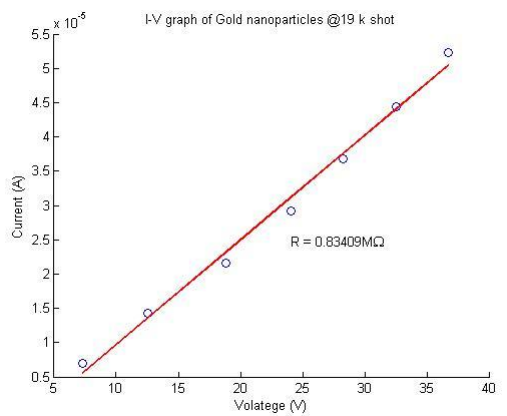
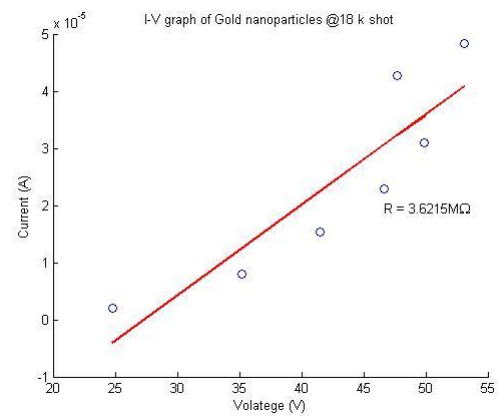
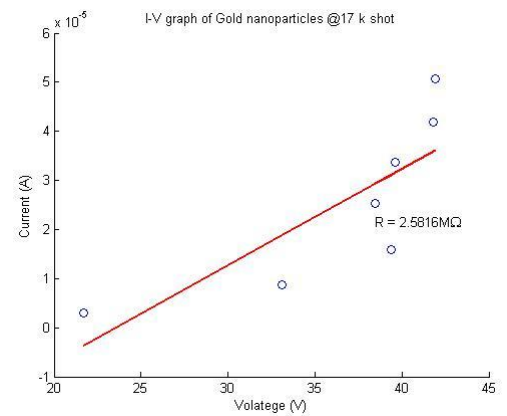
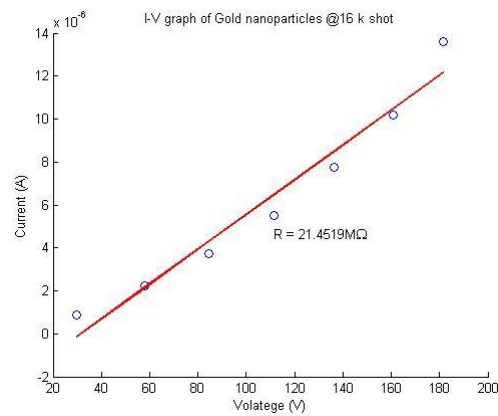
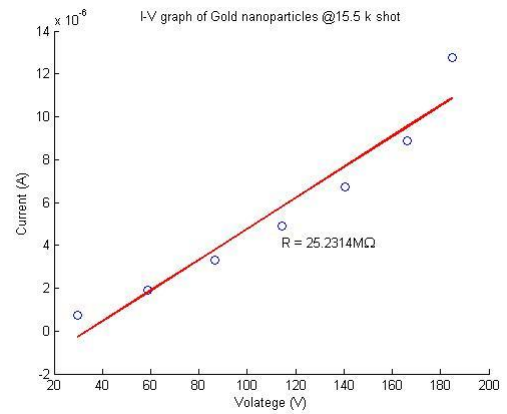
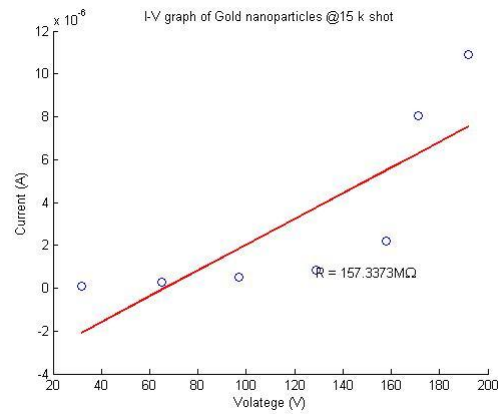
The current passes through the sample  $I_s$  is:

$$I_s = \frac{V_2}{R_3} \dots\dots (A3.2)$$

The process of measuring the resistance of the deposition was done by taking a number of measurements of  $V_s$  and  $I_s$  for each number of shots and form a current-voltage (I-V) curve. Figure A3.2 below shows the I-V curves of the deposition after each group of shots.



## Appendices



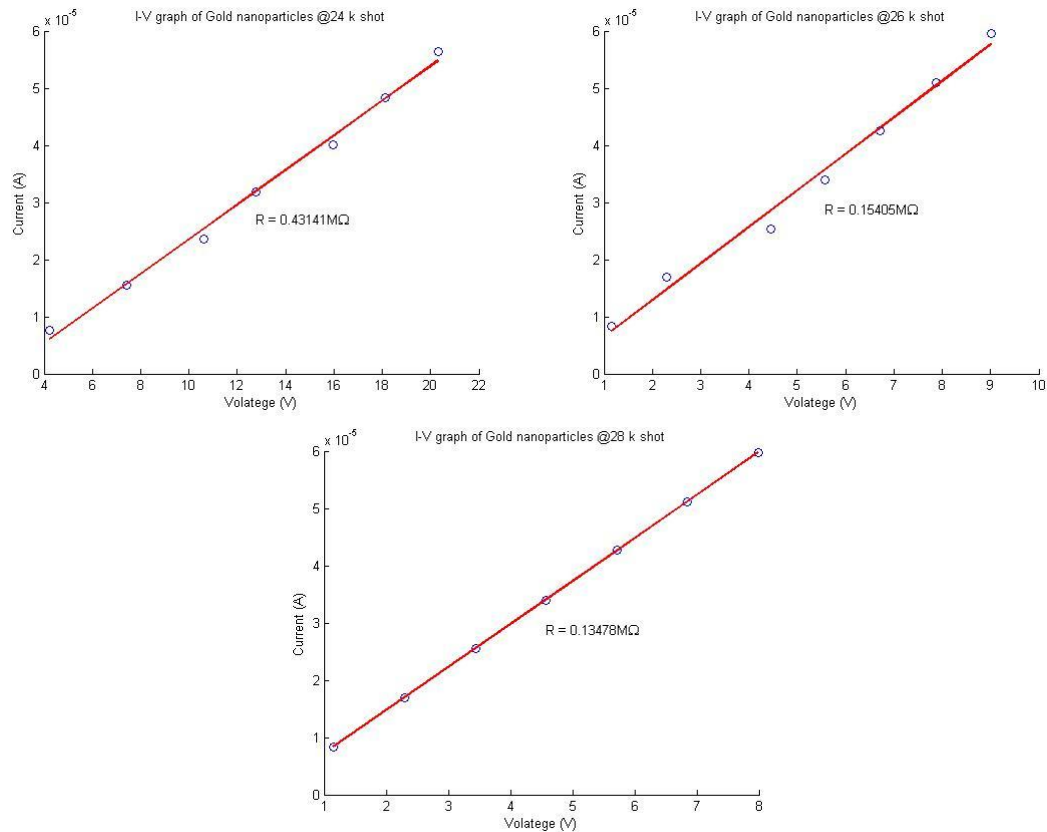


Figure A3.2 I-V curves of the gold nanoparticle deposition as it changes with the number of shots represented in each graph

The resistance shown in Figure 5.12 in section 5.3.3 is calculated as the mean value of resistance from each I-V curve. When the resistance starts dropping at around 15 k shot, the I-V curves showed a chaotic behaviour. This could be due to a rearrangement of the nanoparticle positions as the measurement was taking place.

## **Appendix 4: Submitted paper (to journal of nanoparticle research JNR)**

### **Transit time and charge of gold nanoparticles generated by electrical discharge in ambient air conditions.**

E. Saleh<sup>1\*</sup>, M. Praeger<sup>1</sup>, A. Vaughan<sup>2</sup>, W. Stewart<sup>1</sup>, and W. H. Loh<sup>1</sup>

1 Optoelectronics Research Centre, University of Southampton, SO17 1BJ, U.K.

2 Electronics and Computer Science, University of Southampton, SO17 1BJ, U.K.

\* [ems2g09@soton.ac.uk](mailto:ems2g09@soton.ac.uk)

#### **Abstract**

In this study, we determine the transit time of charged nanoparticles moving in air under the influence of an electric field. Using the theory of Brownian motion and classical laws of motion, we calculate the transit time of charged nanoparticles moving in a strong electric field in air at room conditions. We also measure the transit time experimentally using a spinning disk apparatus, where nanoparticles generated by an electrical discharge reach a spinning substrate at different positions, which represent different transit times.

Using this method, it was found that the transit time of 10nm gold nanoparticles is distributed in a range of 20-210ms for 11mm travel distance, with a peak of transit time at around 55ms.

Using the experimental results and the theory for transit time the charge range of nanoparticles is estimated. This charge and the transit time are major parameters that influence the electrostatic focusing of nanoparticles in direct write applications, which is the main motivation of this study.

## 1. Introduction

Focusing nanoparticles using electrostatic techniques in air requires knowledge of the time of flight of the particles (transit time), and the charge carried by these particles [1-3]. Optical techniques have been reported to measure the velocity and time of flight of micro and nano-scale particles moving in fluids [1, 4, 5]. However, in the presence of a strong electric field, and for nano-scale particles, measuring the behaviour of nanoparticles in flight is a challenging task that requires direct optical detection of the nanoparticles [1, 2, 6].

Nanoparticles moving in a fluid and driven by an electric field have their motion damped by collisions with the fluid molecules. In air at ambient conditions, the particle mean free path is around 70nm [7], which is larger than the dimensions of the nanoparticles but small compared with the propagation distances usually involved, and motion is thus field-driven-diffusion-based.

In this study, we use a spinning substrate with a known angular velocity, and synchronise the nanoparticle generation to one position of the rotation. The deposited nanoparticles are then analysed based on their position on the substrate, which can be translated into the time domain. The deposited nanoparticles give an accurate distribution of transit time, where the position of the particles on the substrate indicates the transit time.

The electrical charge on the nanoparticles is determined by comparing the theory for the transit time with the experimental results. The theoretical analysis of the transit time is based on the study of Brownian motion and the classical laws of motion, where the velocity of particles in a fluid is calculated from Einstein's solution of Brownian motion, and the transit time is derived from the calculated velocity using classical laws of motion.

## 2. Motivation:

Nanoparticle focusing in ambient conditions is reported using lithographical techniques [8-10] as well as direct writing techniques [11]. The focusing is achieved by manipulating the particle trajectories to follow converging electric field lines. However, countering this focusing in air, the nanoparticles diffuse due to collisions with air molecules and cause a spreading effect. Also similarly charged particles mutually repel and diverge from following the electric field lines.

The diffusion of nanoparticles in a gas was described in Einstein's study of Brownian motion [12], where the density profile of Brownian particles ( $p(x, t)$ ) on point ( $x$ ) in one dimension at a time ( $t$ ) is:

$$p(x, t) = \frac{1}{\sqrt{4\pi Dt}} e^{-\frac{x^2}{4Dt}} \dots\dots\dots (1)$$

where ( $D$ ) is the diffusivity of a particle in gas, which depends on the temperature ( $T$ ) of the gas, the dynamic viscosity of the gas ( $\eta$ ) and the radius of the particle ( $r$ ):

$$D = \frac{k_B T}{6\pi\eta r} \dots\dots\dots (2)$$

On the other hand, the interaction between charged nanoparticles whilst in transit is not just dependent on the transit time, but also on the charge ( $Q_x$ ) of the particles [13], where the force ( $F_i$ ) between two charged particles is:

$$F_i = k_C \frac{Q_1 Q_2}{s^2} \dots\dots\dots (3)$$

where ( $k_C$ ) is the coulomb constant, ( $Q_1$ ) and ( $Q_2$ ) are the particle charges, and ( $s$ ) is the separation between the particles ( $s \neq 0$ ). From Einstein's solution of Brownian motion, the velocity ( $v$ ) of a particle moving under a force ( $F$ ) in a fluid is:



$$v = \frac{F}{6\pi\eta r} \dots\dots\dots (4)$$

Substituting equation (3) with (4) for the force ( $F_i$ ) gives the velocity of the particles ( $v_i$ ) due to interaction:

$$v_i = \frac{k_B Q_1 Q_2}{6\pi\eta r s^2} \dots\dots\dots (5)$$

As the velocity of particles in air represents a first order differential equation where  $v_i = \frac{ds}{dt}$ , solving equation (5) for ( $ds$ ) gives:

$$s = \sqrt[3]{\frac{k_B Q_1 Q_2 t}{2\pi\eta r} + s_0^3} \dots\dots\dots (6)$$

where ( $s_0$ ) is the initial separation between the particles at time ( $t = 0$ ).

As shown in equation (1) and equation (6) for the particle diffusion and particle interaction, respectively, the longer the transit time the more diffusion occurs and the more divergence happens due to charged-particles interaction. So studying the transit time and the charge of the particles will allow for further control over the focusing of nanoparticles.

### 3. Particle formation in an electrical discharge:

Although not the primary subject of this investigation we note that an electrical discharge is generated in ambient conditions when high voltage is applied between two electrodes, and the applied potential exceeds the breakdown threshold of the gas in the gap between the electrodes, which is in our case is filled with air. When the voltage is high enough to breakdown the air, current suddenly flows within the gas forming a conducting channel.

The sudden flow of electrons and ions generates enormous heat and pressure that can exceed the atmospheric conditions by more than 3 orders of magnitude [14-17], which is sufficient to melt and vaporise the material of the electrodes.

The main mechanism of forming nanoparticles in a spark discharge is reported to be due to the condensation of the vapour of the electrodes [18, 19], as the vapour cools down, charged nanoparticles are formed and follow the electric field gradient.

#### 4. Transit time theoretical analysis:

Nanoparticles produced in an electrical discharge diffuse in air as they follow the electric field gradient whilst continuously exchanging momentum with the air molecules. Einstein studied the theory of diffusion in his analysis of Brownian motion, and related the velocity of particles ( $v$ ) to the force ( $F$ ) applied on the particle, the dynamic viscosity ( $\eta$ ) of the fluid and the radius ( $r$ ) of the particle as shown in equation (4).

In the presence of a strong electric field and under these diffusive conditions, charged nanoparticles will not move ballistically but accelerate and decelerate based on the local electric field gradient in the system. The dominant force on the nanoparticles is due to the electric field ( $E$ ) and the charge of the particle ( $Q$ ), which is the electric field force  $F = QE$ . Therefore the velocity of particles moving in an electric field can be written as:

$$v = \frac{QE}{6\pi\eta r} \dots\dots\dots (7)$$

Using the kinematic laws of motion, the distance ( $d$ ) that an object travels with known velocity is:

$$d = \int v \, dt \dots\dots\dots (8)$$

Using a discrete form to solve the complete travel distance, by substituting equation (7) in (8) we can

calculate the transit time ( $\Delta t$ ) between every two points in the space:

$$\Delta t = \frac{6n\pi\Delta d\eta r}{Q \sum_{i=1}^{i=n} E_i} \dots\dots\dots (9)$$

where ( $n$ ) is the number of discrete values of the electric field within the distance ( $\Delta d$ ).

## 5. Transit time of nanoparticles generated by electrical discharge:

For nanoparticles generated using an electrical discharge and reported for ion induced focusing and direct writing purposes [8-11] the transit time can be computed using equation (9) for the configuration shown in figure 1.

The strong electric field on the gold electrodes generates a spark discharge and the field provides the force that is required to move the nanoparticles from the gold electrodes to the substrate. The simulation also includes a stainless-steel tube with 800V applied to it, which controls the electric field trajectories and confines them to follow converging paths. The electric field value of each point in the particles trajectory is used to determine the transit time of the nanoparticles providing values for the charge ( $Q$ ) and the radius of the particles ( $r$ ).

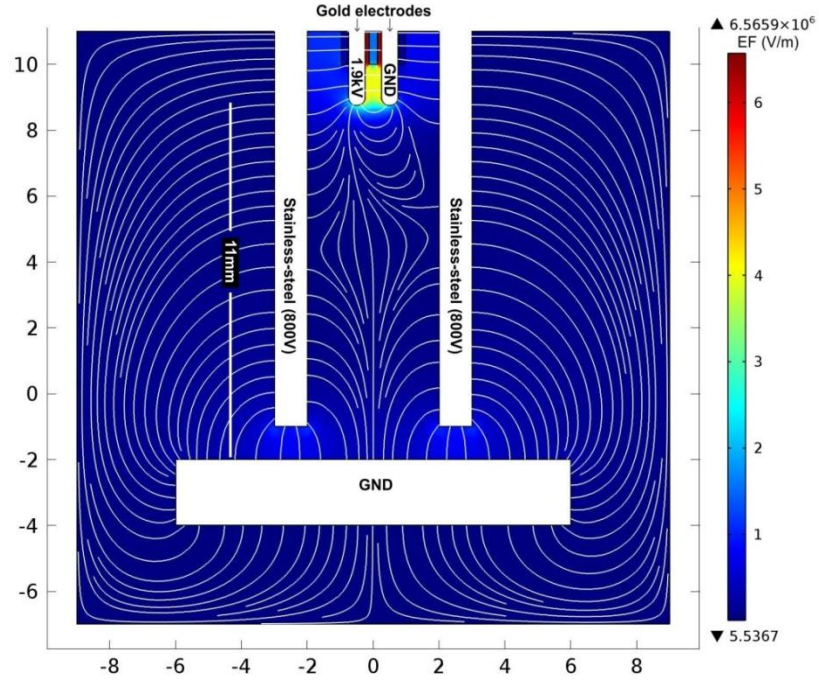


**Figure 1** Electric field configuration.

Figure 2 shows the transit time of nanoparticles of different sizes, and the effect of the charge of the particles on the transit time derived using equation (9), where the electric field is determined for the distance between the discharge electrodes and the grounded substrate using Comsol Multiphysics simulation software shown in figure 1.

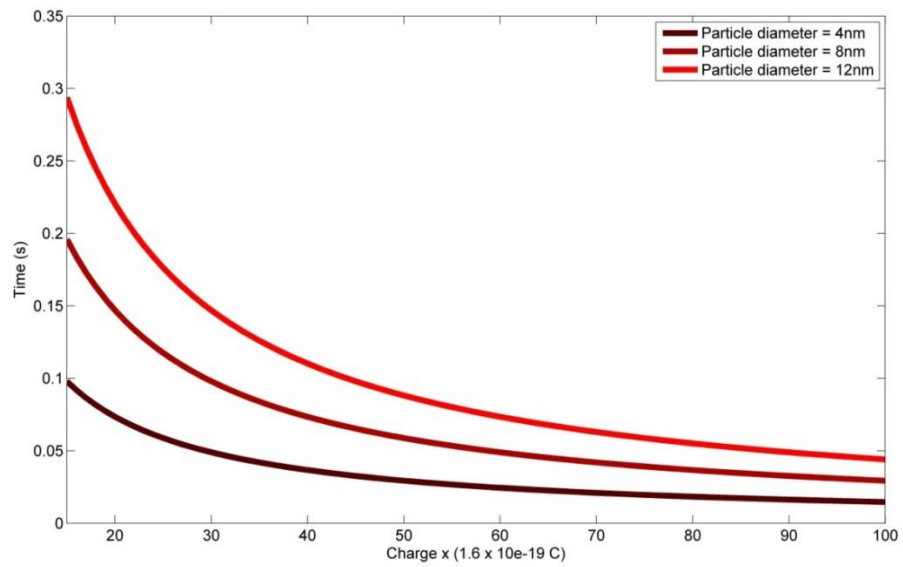


**Figure 2** Transit time of nanoparticles with different diameters for a range of charge values.

## 6. Experimental analysis and results:

To measure the transit time of the nanoparticles for the configuration shown in figure 1, a spinning substrate is placed 1mm under the stainless-steel focusing tube (10mm long), and a high voltage (HV) pulse is synchronised to be triggered at one rotational position of the substrate as shown in figure 3.

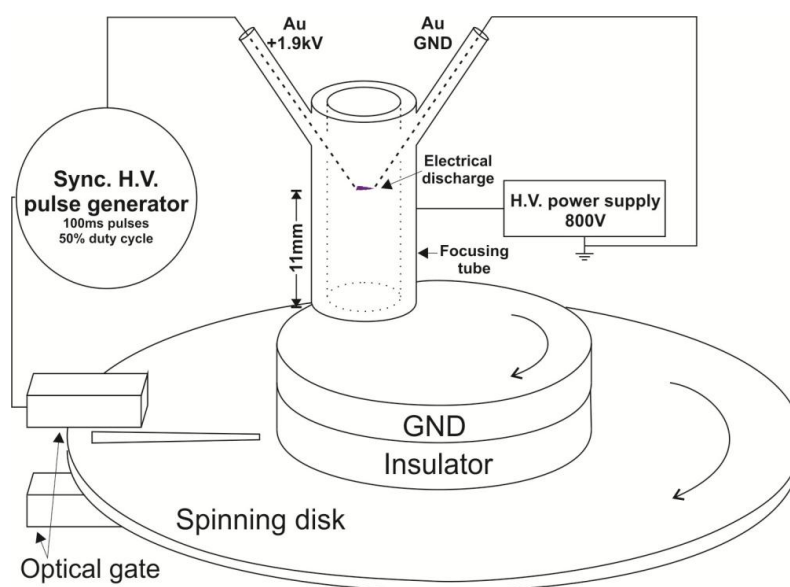


**Figure 3** schematic diagram of nanoparticles transient time measurement apparatus.

The time taken to complete one rotation of the substrate is set to 210ms, and the HV pulse width is 50ms. By analysing the deposition pattern (figure 4), it was found that the deposition starts at around 20ms after the discharge trigger, with the highest density of deposition appearing at around 55ms. Thereafter, the deposition diminishes until the end of the spinning cycle as shown in figure 4. The dark spot at the top of the deposition ring is contamination that occurred after the experiment.

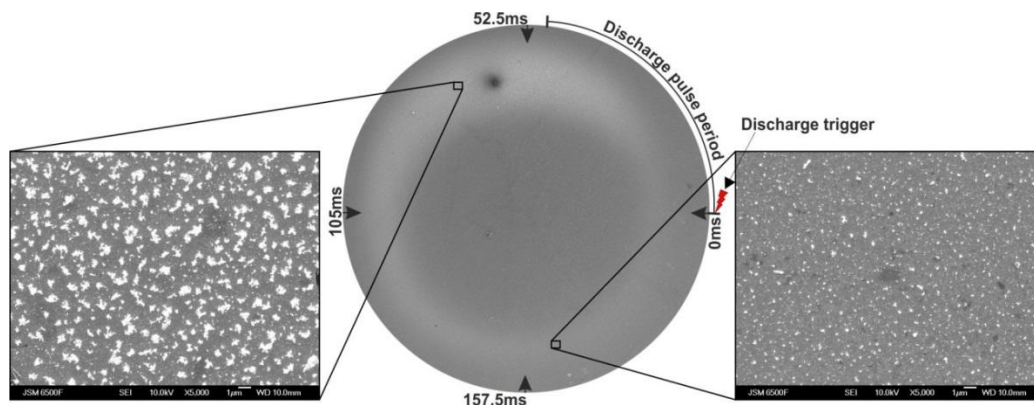


**Figure 4** SEM graphs of the deposited gold nanoparticles on a pulse-synchronised spinning substrate.

The deposited nanoparticles generated by an electrical discharge were analysed using a transmission electron microscope (TEM) and a scanning electron microscope (SEM), from which, the diameter of the nanoparticles is in the order of 10nm with strong clustering effect, as shown in figure 5. This diameter range agrees with previous reports for electrical discharge generated nanoparticles produced under similar conditions [18, 19].

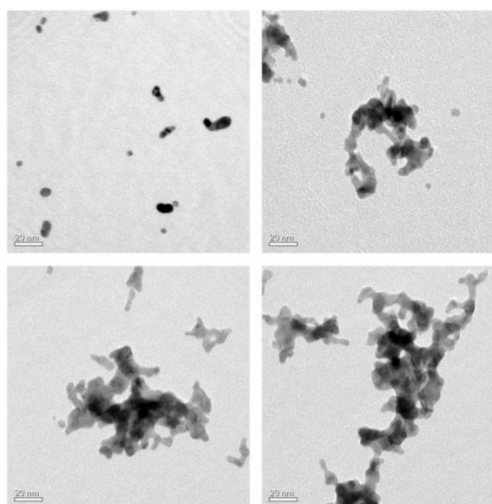


**Figure 5** TEM graphs of the generated particles.

To analyse the transit time of the nanoparticles, high resolution SEM micrographs were obtained at different positions within the deposition pattern shown in figure 4. The number of particles in each micro-

graph was computed assuming an average primary particle diameter of 10nm, and from these the density of the deposited nanoparticles was estimated. As an independent measure the grey level of the deposition ring shown in figure 4 (middle graph) is used to confirm the distribution of the density of particles, where a high density of particles appears brighter (see figure 6). The distributions from these measures are seen to agree quite well.

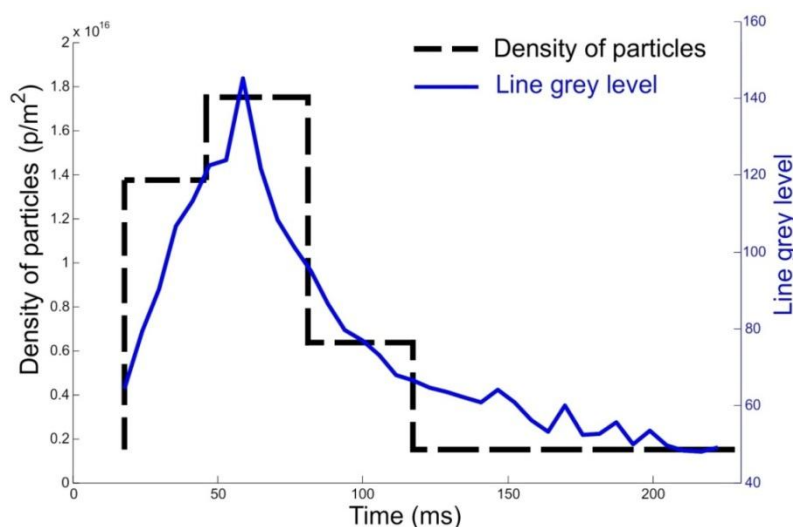


**Figure 6** Density of particles against transit time.

The range of transit times shown in figure 6 can be used to estimate the charge on the nanoparticles using equation (9) providing an estimation of particle diameters. The distribution of charge for each assumed particle size can be estimated by applying the experimental distribution of transit time using the density profile of particles. Figure 7 shows a histogram of the charge of nanoparticles based on their size using the theoretical and experimental results of this study.

To assess the validity of the estimated charge, the highest theoretical charge that a particle could carry can be calculated from the Rayleigh charge limit.

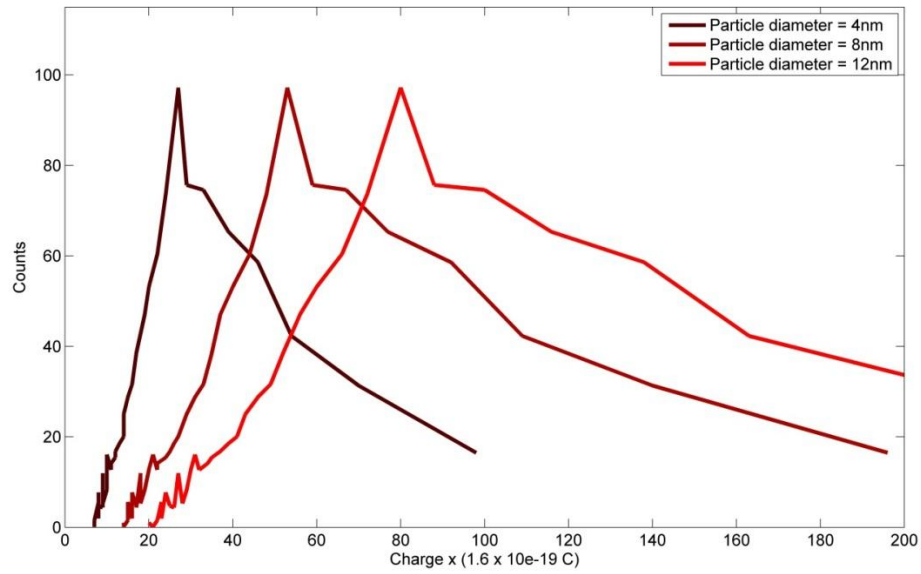


**Figure 7** Histogram of the elementary charges for each particle size.

The Rayleigh limit describes the maximum charge a liquid droplet can hold before it becomes unstable [20]. A high charge concentrated in a liquid drop generates an electrostatic force repelling the atoms or molecules of the liquid. This repulsion force works against the bonding force between the liquid molecules represented in the surface tension of that liquid ( $\gamma$ ). When the electrostatic force due to the charge is higher than the surface tension force in a liquid drop, instability of the liquid droplet occurs causing a burst of material from the liquid droplet.

Rayleigh charge limit ( $Q_r$ ) depends on the surface tension of the liquid ( $\gamma$ ) and the radius ( $r$ ) of the liquid droplet, where ( $\epsilon_0$ ) is the permittivity of free space:

$$Q_r = 8\pi\sqrt{\epsilon_0\gamma r^3} \dots\dots\dots (10)$$



When the particles are in the formation stage, and gold vapour is condensing forming nanoparticles in the liquid state, the maximum charge that a gold droplet would be able to carry can be calculated using the Rayleigh limit.

The surface tension of molten gold is reported to be in the order of 1100mN/m [21, 22], and the Rayleigh charge limit for different droplet diameters is shown in figure 8.

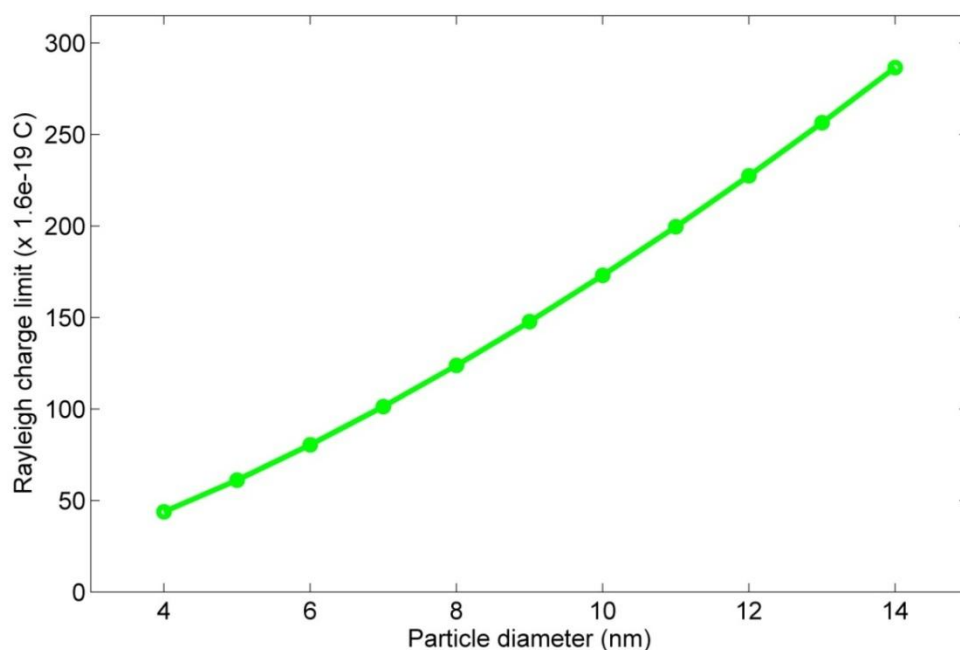


**Figure 8** maximum charge of particles for different size calculated from the Rayleigh charge limit.

Comparing the theoretical limit of charge from Rayleigh limit with the estimated charge for each particle size shown in figure 7, for the 4nm, 8nm and 12nm particle sizes, the Rayleigh charge is 44, 124 and 228 elementary charges, respectively. This shows that the peaks of the charge histogram shown in figure 7 for each size are well within the Rayleigh charge limit.

### **7. Conclusion:**

We have used a theoretical analysis and experimental study to determine the transit time and charge of nanoparticles that are generated by an electrical discharge. A spinning disk with known angular speed is used, and the transit time of the nanoparticles is represented by the position of particles on the spinning disk. This method gives a distribution of time rather than an average transit time for all particles, and it allows for further analysis on the deposited nanoparticles, unlike the on-flight measurements which allows only for short period observations.

Using this spinning disk method it was found that the transit time of the nanoparticles generated by an electrical discharge is ranging from 20ms to 210ms with the highest density of deposition appearing at around 55ms. When the theoretical analysis is combined with the experimental results it was possible to estimate the charge of the nanoparticles for different particle size, where the peak of the charge distribution appears at around 60 elementary charges for 10nm diameter particles.

The results of this study led to further understanding of the time it takes nanoparticles generated by an electrical discharge inside a focusing tube to reach the substrate, which allows for more control over the nanoparticles motion in order to manipulate their trajectories for electrostatic focusing purposes.

### **Acknowledgment**

The authors gratefully acknowledge funding support from EPSRC (Engineering and Physical Sciences Research Council) under the GlassJet Printer project, and the EPSRC Centre for Innovative Manufacturing in Photonics at the University of Southampton-UK.

## References:

- [1] Hutchins D K, Holm J, Addison S R, 1991, Electrodynamic Focusing of Charged Aerosol Particles, *Aerosol Science and Technology*, 14:389-405
- [2] Kane D, Oktem B, Johnston M V, 2001, An Electrostatic Lens for Focusing Charged Particles in a Mass Spectrometer, *Aerosol Science and Technology*, 35: 990–997
- [3] Rysanek F and Burton R, 2008, Charging of Macroparticles in a Pulsed Vacuum Arc Discharge, *IEEE TRANSACTIONS ON PLASMA SCIENCE*, 36(5)
- [4] Sato T 1980, Drift velocity measurement of charged particles under corona discharge in an air gap. I, *Journal of Electrostatics*, 8:271–278
- [5] Ray K, Zhang J, Lakowicz J R, 2008, Fluorescence Lifetime Correlation Spectroscopic Study of Fluorophore-Labeled Silver Nanoparticles, *Anal. Chem.*, 80:7313–7318
- [6] Qian M, Liu J, Yan M S, Shen Z H, Lu J, Ni X W, Li Q, Xuan Y M, 2006, Investigation on utilizing laser speckle velocimetry to measure the velocities of nanoparticles in nanofluids, *Optics Express*, 14(17):7559–7566
- [7] Jennings S 1988, The mean free path in air, *J. Aerosol Sci.*, 19(2):159-166
- [8] Kim H, Kim J, Yang H, Suh J, Kim T, Han B, Kim S, Kim D S, Pikhitsa P V, Choi M, 2006, Parallel patterning of nanoparticles via electrodynamic focusing of charged aerosols, *Nat. Nanotechnology*, 1:117–121
- [9] Cole J J, Lin E, Barry C R, Jacobs H O 2009, Continuous nanoparticle generation and assembly by atmospheric pressure arc discharge, *Appl. Phys. Lett.* 95:113101
- [10] Lee H, You S, Pikhitsa P V, Kim J, Kwon S, Woo C G, Choi M, 2011, Three-Dimensional Assembly of Nanoparticles from Charged Aerosols, *Nano Lett.* 11:119–124

- [11] Saleh E, Praeger M, Vaughan A S, Stewart W, Loh W H, 2012, The direct writing and focusing of nanoparticles generated by an electrical discharge, *Journal of Nanoparticle Research*, 14:1220
- [12] Einstein A, 1905, Investigations on the Theory of the Brownian Movement, *Annalen der Physik*, 17: 549
- [13] Lee W, Lee S Y, Zhang X, Rabin O, Briber R M, 2013, Hexagonally ordered nanoparticles templated using a block copolymer film through Coulombic interactions, *Nanotechnology*, 24:045305
- [14] Benzerga L, Lhiaubet C, Meyer R M, 1985, Improvement of a proposed model for heat conduction in an electrode submitted to an electric discharge: Application to the indirect determination of the anodic and cathodic voltage drops, *J. Appl. Phys.* 58(1).1
- [15] DiBitonto D., Eubank P., Patel M, Barrufet M. (1989) Theoretical models of the electrical discharge machining process. I. A simple cathode erosion model, *J. Appl. Phys.* 66(9)
- [16] Albinski K, Musiol K, Miernikiewicz A, Labuz S and Malota M, 1996, The temperature of a plasma used in electrical discharge machining, *Plasma Sources Sci. Technol.* 5:736–742
- [17] Salah N., Ghanem G., Atig K, 2008, Thermal and mechanical numerical modelling of electric discharge machining proces, *Communications in Numerical Methods in Engineering*, 24:2021–2034
- [18] Tabrizi N, Ullmann M, Vons V, Lafont U, Schmidt-Ott A, 2009, Generation of nanoparticles by spark discharge, *J. Nanopart. Res*, 11:315–332
- [19] Boddu S, Gutti V, Ghosh T, Thompson R, Loyalka S, 2011, Gold, silver, and palladium nanoparticle/nano-agglomerate generation, collection, and characterization, *J. Nanoparticle Research*, 13:6591–6601

[20] Rayleigh L, 1882, On the equilibrium of liquid conducting masses charged with electricity, Philos.

Mag. 14:184

[21] Ricci E and Novakovic R, 2001, Wetting and Surface Tension Measurements on Gold Alloys, Gold

Bulletin, 34(2)

[22] Lu H M and Jiang Q, 2005, Surface Tension and Its Temperature Coefficient for Liquid Metals, J.

Phys. Chem. B, 109:15463-15468

## Bibliography

1. LE, H. Progress and Trends in Ink-jet Printing Technology. **Journal of Imaging Science and Technology**, v. 42, p. 49-62, 1998.
2. ZOLTAN., S.; AL., E. **PULSED DROPLET EJECTING SYSTEM**. 3683212, Aug 1972.
3. KELLY, A. **Method and apparatus for fluid jet printing**. 4364054, Dec 1982.
4. P. H. CHEN, ET AL. Droplet formation of a thermal sideshooter inkjet printhead. **International Journal of Heat and Fluid Flow**, v. 19, n. 4, p. 382-390, 1998.
5. C.D. MEINHART, H.S. ZHANG. The flow structure inside a microfabricated inkjet printhead. **Journal of Microelectromechanical Systems**, v. 9, n. 1, p. 67-75, 2000.
6. ENDO, I. **Liquid jet recording process and apparatus therefor**. GB2007162, May 1979.
7. GALE, M. et al. Fabrication of continuous-relief micro-optical elements by direct laser writing in photoresists. **Optical Engineering**, v. 33, n. 11, p. 3556-3566, 1994.
8. NAESSENS, K. et al. Direct writing of microlenses in polycarbonate. **APPLIED OPTICS**, v. 42, n. 31, p. 6349, 2003.
9. KAUR, K.; SUBRAMANIAN, A.; YING, Y.; BANKS, D.; FEINAEUGLE, M.; HORAK, P.;

## Bibliography

- APOSTOLOPOULOS, V.; SONES, C.; MAILIS, S.; EASON, R.. Waveguide mode filters fabricated using laserinduced forward transfer. **OPTICS EXPRESS**, v. 19, n. 10, p. 9814, 2011.
10. DEMERS, L. et al. Direct Patterning of Modified Oligonucleotides on Metals and Insulators by Dip-Pen Nanolithography. **SCIENCE**, v. 296, p. 1836, 2002.
11. HWANG, K. et al. Control of line width with active nano fountain pen (ANFP) for nano manufacturing. **Journal of Mechanical Science and Technology**, v. 22, p. 1339-1348 , 2008.
12. SALATA, O. Tools of Nanotechnology: Electrospray. **Current Nanoscience**, v. 1, p. 25-33, 2005.
13. PARK, J. et al. High-resolution electrohydrodynamic jet printing. **Nature Materials**, v. 6, p. 782-789, 2007.
14. BROWN, T.; DALTON, P.; HUTMACHER, D. Direct Writing By Way of Melt Electrospinning. **Adv. Mater.**, v. 23, p. 5651–5657, 2011.
15. LEE, J. et al. Fabrication of Patterned Nanofibrous Mats Using Direct-Write Electrospinning. **Langmuir**, v. 28, n. 18, p. 7267–7275, 2012.
16. LIU, Q.; ORME, M. High precision solder droplet printing technology and the state-of-the-art. **Journal of Materials Processing Technology**, v. 115, n. 3, p. 271–283, 1999.

17. LIU, Q.; ORME, M. **High precision solder droplet printing technology**: principle and applications. International Symposium on Advanced Packaging Materials. [S.l.]: [s.n.]. 2001. p. 104-109.
  
18. HARA, T. et al. **Ink jet recording device using thermal propulsion and mechanical pressure changes**. 4296421, 20 out. 1981.
  
19. HAWKINS, W. G. **Bubble jet printing device**. 4532530, 30 jul. 1985.
  
20. WU, H. et al. Study of Micro-Droplet Behavior for a Piezoelectric Inkjet Printing Device Using a Single Pulse Voltage Pattern. **Materials Transactions**, v. 45, n. 4, p. 1794-1801, 2004.
  
21. LEE, T. et al. Drop-on-Demand Solder Droplet Jetting System for Fabricating Microstructure. **IEEE TRANSACTIONS ON ELECTRONICS PACKAGING MANUFACTURING**, v. 31, n. 3, p. 202, 2008.
  
22. ZELENY, J. On the conditions of instability of liquid drops, with applications to the electrical discharge from liquid points. **Proceedings of the Cambridge Philosophical Society**, v. 18, p. 71-93, 1915.
  
23. JAYASINGHE, S.; EDIRISINGHE, M.; WANG, D. Controlled deposition of nanoparticle clusters by electrohydrodynamic atomization. **Nanotechnology**, v. 15, p. 1519-1523, 2004.
  
24. WANG, D. et al. Coaxial electrohydrodynamic direct writing of nano-suspensions.



## Bibliography

**Journal of Nanoparticle Research**, v. 9, p. 825–831, 2007.

25. KHAN, S. et al. Direct patterning and electrospray deposition through EHD for fabrication of printed thin film transistors. **Current Applied Physics**, v. 11, n. 1, p. S271–S279, 2011.
26. HUANG, Z. et al. A review on polymer nanofibers by electrospinning and their applications in nanocomposites. **Composites Science and Technology**, v. 63, n. 15, p. 2223–2253, 2003.
27. AHMED, Z.; RASEKH, M.; EDIRISINGHE, M. Electrohydrodynamic direct writing of biomedical polymers and composites. **Macromol Mater Eng**, v. 295, p. 315–319, 2010.
28. LASTOW, O.; BALACHANDRAN, W. Novel low voltage EHD spray nozzle for atomization of water in the cone jet mode. **Journal of Electrostatics**, v. 65, p. 490–499, 2007.
29. LI, D.; HERRICKS, T.; XIA, Y. Magnetic nanofibers of nickel ferrite prepared by electrospinning. **Appl Phys Lett**, v. 83, n. 22, p. 4586–4588, 2003.
30. MARGINEAN, I. et al. Flexing the electrified meniscus: the birth of a jet in electrosprays. **Anal. Chem.**, v. 76, p. 4202–4207, 2004.
31. RENEKER, D. et al. Electrospinning of Nanofibers from Polymer Solutions and Melts. **Advances in Applied Mechanics**, v. 41, p. 43–195, 2007.

32. SAGEMAN, D.; BURNET, G. Predicting the surface tension of liquid metals. **J Inorg Nucl Chem**, v. 36, p. 1105-1107, 1974.
33. JIANG, Q.; LU, H. Surface tension and its temperature coefficient for liquid metals. **J Phys Chem B**, v. 109, p. 15463-15468, 2005.
34. FLINT, O. SURFACE TENSION OF LIQUID METALS. **JOURNAL OF NUCLEAR MATERIALS**, v. 16, p. 233-248, 1965.
35. TAYLOR, G. I. Disintegration of water drops in electric field. **Proceedings of the Royal Society**, v. 280, n. 1382, p. 383-397, 1964.
36. RAYLEIGH, L. On the equilibrium of liquid conducting masses charged with electricity. **Philos. Mag.**, v. 14, p. 184, 1882.
37. ABBAS, M.; LATHAM, J. The Instability of Evaporating Charged Drops. **J. Fluid Mech.**, v. 30, p. 663, 1967.
38. TAFLIN, D.; WARD, T.; DAVIS, E. Electrified Droplet Fission and the Rayleigh Limit. **Langmuir**, v. 5, p. 376-384, 1988.
39. SHRIMPTON, J. Dielectric Charged Drop Breakup at Sub-Rayleigh Limit. **IEEE Transactions on Dielectrics and Electrical Insulation**, v. 12, n. 3, p. 573-578, 2005.
40. KRPOUN, R.; SHEA, H. A method to determine the onset voltage of single and

## Bibliography

- arrays. **JOURNAL OF APPLIED PHYSICS**, v. 104, 2008.
41. SI, B.; BYUN, D.; LEE, S. Experimental and theoretical study of a cone-jet for an electro spray microthruster considering the interference effect in an array of nozzles. **Aerosol Science**, v. 38, p. 924 – 934, 2007.
42. XIONG, J. et al. Investigation of the Onset Voltage for the Design of a Microfabricated Colloid Thruster. **IEEE/ASME TRANSACTIONS ON MECHATRONICS**, v. 11, n. 1, 2006.
43. IKONOMOU, M.; BLADES, A.; KEBARLE, P. Electro spray mass spectrometry of methanol and water solutions suppression of electric discharge with SF6 gas. **American Society for Mass Spectrometry**, v. 2, n. 6, p. 497–505, 1991.
44. TANG, K.; GOMEZ, A. Generation by electro spray of monodisperse water droplets for targeted drug delivery by inhalation. **Journal of Aerosol Science**, v. 25, n. 6, p. 1237–1249, 1994.
45. LO ´PEZ-HERRERA, J. et al. An Experimental Study of the Electro spraying of Water in Air at Atmospheric Pressure. **J. American Society for Mass Spectrometry**, v. 15, p. 253–259, 2004.
46. MARGINEAN, I.; NEMES, P.; VERTES, A. Order-Chaos-Order Transitions in Electro sprays: The Electrified Dripping Faucet. **PHYSICAL REVIEW LETTERS**, v. 97, n. 6, 2006.

47. WHITE, D. W. The Surface Tensions of Indium and Cadmium. **METALLURGICAL TRANSACTIONS**, v. 3, p. 1972-1933, 1971.
48. LU, M.; JIANG, Q. Surface Tension and Its Temperature Coefficient for Liquid Metals. **J. Phys. Chem. B**, v. 109, p. 15463-15468, 2005.
49. DAVIS, J.; BARTEL, F. Determination of Surface Tension of Molten Materials. **ANALYTICAL CHEMISTRY**, v. 20, n. 12, p. 1182, 1948.
50. SHIM, S. et al. Wetting and surface tension of bismate glass melt. **Thermochimica Acta**, v. 496, n. 1-2, p. 93-96, 2009.
51. FUJINO, S.; HWANG, C.; MORINAGA, K. Surface tension of PbO-B<sub>2</sub>O<sub>3</sub> and Bi<sub>2</sub>O<sub>3</sub>-B<sub>2</sub>O<sub>3</sub> glass melts. **Journal of Materials Science**, v. 40, n. 9-10, p. 2207-2212, 2005.
52. WRAY, P. Cotton candy' that heals? **American Ceramic Society Bulletin**, v. 90, n. 4, 2011.
53. FU, Q. et al. Silicate, borosilicate, and borate bioactive glass scaffolds with controllable degradation rate for bone tissue engineering applications. I. Preparation and in vitro degradation. **Journal of Biomedical Materials Research Part A**, v. 95A, n. 1, 2010.
54. RAHAMAN, M. et al. Bioactive glass in tissue engineering. **Acta Biomater**, v. 7, n. 6, p. 2355-2373, 2011.

## Bibliography

55. UHM, H.; JUNG, S.; KIM, H. Influence of Gas Temperature on Electrical Breakdown in Cylindrical Electrodes. **Journal of the Korean Physical Society**, v. 42, p. S989-S993, 2003.
56. HUSAIN, E.; NEMA, R. S. Analysis of Paschen Curves for air, N<sub>2</sub> and SF<sub>6</sub> Using the Townsend Breakdown Equation. **IEEE Transactions on Electrical Insulation**, v. EI-17, n. 4, p. 350, 1982.
57. GO, D.; POHLMAN, D. A mathematical model of the modified Paschen's curve for breakdown in microscale gaps. **JOURNAL OF APPLIED PHYSICS**, v. 107, p. 103303, 2010.
58. DHARIWAL, R.; TORRES, J.; DESMULLIEZ, M. Electric field breakdown at micrometre separations in air and nitrogen at atmospheric pressure. **IEE Proc.Sci. Mcus. Technol.**, v. 147, n. 5, 2000.
59. TIRUMALA, R.; GO, D. An analytical formulation for the modified Paschen's curve. **APPLIED PHYSICS LETTERS**, v. 97, p. 151502, 2010.
60. SILI, E.; CAMBRONNE, J.; KOLIATENE, F. Temperature Dependence of Electrical Breakdown Mechanism on the Left of the Paschen Minimum. **IEEE TRANSACTIONS ON PLASMA SCIENCE**, v. 39, n. 11, p. 3173, 2011.
61. TORRES, J.; DHARIWAL, R. Electric field breakdown at micrometre separations. **Nanotechnology**, v. 10, p. 102-107, 1999.

62. SLADE, P.; TAYLOR, E. Electrical Breakdown in Atmospheric Air Between Closely Spaced (0.2  $\mu\text{m}$ –40  $\mu\text{m}$ ) Electrical Contacts. **IEEE TRANSACTIONS ON COMPONENTS AND PACKAGING TECHNOLOGIES**, v. 25, n. 3, p. 390-396, 2002.
63. ZHANG, W.; FISHER, T.; GARIMELLA, S. Simulation of ion generation and breakdown in atmospheric air. **JOURNAL OF APPLIED PHYSICS**, v. 96, n. 11, 2004.
64. PRAEGER, M. et al. Fabrication of nanoscale glass fibers by electrospinning. **APPLIED PHYSICS LETTERS**, v. 100, p. 063114, 2012.
65. M., L. **Artificial light, its influence upon civilization**. New York: THE CENTURY CO., 1920.
66. BENZERGA, L.; LHIAUBET, C.; MEYER, R. M. Improvement of a proposed model for heat conduction in an electrode submitted to an electric discharge: Application to the indirect determination of the anodic and cathodic voltage drops. **J. Appl. Phys.**, v. 58, p. 604, 1985.
67. DIBITONTO, D. D. et al. Theoretical models of the electrical discharge machining process. I. A simple cathode erosion model. **J. Appl. Phys**, v. 66, p. 4095, 1989.
68. ALBINSKI, K. et al. The temperature of a plasma used in electrical discharge machining. **Plasma Sources Sci. Technol.**, v. 5, p. 736–742, 1996.
69. SALAH, N.; GHANEM, F.; ATIG, K. Thermal and mechanical numerical modelling of

## Bibliography

- electric discharge machining process. **Communications in Numerical Methods in Engineering**, v. 24, p. 2021-2034, 2008.
70. DULEBOHN, D.; MINN, M. **Tracer controlled machining by electrically induced erosion**. 3,614,372, Oct 1971.
71. PANDEY, A.; SINGH, S. Current research trends in variants of Electrical Discharge Machining: A review. **International Journal of Engineering Science and Technology**, v. 2, n. 6, p. 2172-2191, 2010.
72. LOPEZ-ESTEBAN, S. et al. Electrical discharge machining of ceramic/semiconductor/metal nanocomposites. **Scripta Materialia**, v. 63, p. 219-222, 2010.
73. MALEK, C.; BOY, L. J.; BLIND, P. Deep microstructuring in glass for microfluidic applications. **Microsystem Technologies**, v. 13, n. 5-6, p. 447-453, 2007.
74. RICHARDSON, M.; GIANCHANDANI, Y. Achieving precision in high density batch mode micro-electro-discharge machining. **JOURNAL OF MICROMECHANICS AND MICROENGINEERING**, v. 18, p. 12, 2008.
75. TAKAHATA, K.; GIANCHANDANI, Y. Batch Mode Micro-Electro-Discharge Machining. **JOURNAL OF MICROELECTROMECHANICAL SYSTEMS**, v. 11, n. 2, p. 102-110, 2002.
76. GRAY, E. W.; PHARNEY, J. R. Electrode erosion by particle ejection in lowcurrent

arcs, v. 45, p. 667, 1974.

77. SCHWYN, S.; GARWIN, E.; SCHMIDT-OTT, A. AEROSOL GENERATION BY SPARK DISCHARGE, v. 19, p. 639-642, 1988.

78. LUNG, J. et al. Preparation of gold nanoparticles by arc discharge in water. **J. Alloy Compd.**, v. 434-435, p. 655-658, 2007.

79. TABRIZI, N. et al. Generation of nanoparticles by spark discharge. **J. Nanoparticles Research**, v. 11, p. 315-332, 2009.

80. BODDU, S. et al. Gold, silver, and palladium nanoparticle/nano-agglomerate generation, collection, and characterization. **J. Nanoparticle Research**, v. 13, p. 6591-6601, 2011.

81. VONS, V. et al. Silicon nanoparticles produced by spark discharge. **J. Nanoparticle Research**, v. 13, p. 4867-4879, 2011.

82. KIM, H. et al. Parallel patterning of nanoparticles via electrodynamic focusing of charged aerosols. **Nature Nanotechnology**, v. 1, p. 117-121, 2006.

83. COLE, J. et al. Continuous nanoparticle generation and assembly by atmospheric pressure arc discharge. **Appl. Phys. Lett.**, v. 95, p. 113101, 2009.

84. LEE, H. et al. Three-Dimensional Assembly of Nanoparticles from Charged Aerosols. **Nano Lett.**, v. 11, n. 1, p. 119-124, 2011.



## Bibliography

85. ZELNY, J. The Mechanism of the Electric Spark. **J. Appl. Phys**, v. 13, p. 444, 1942.
86. JONES, F. L. Physics of electrical discharge. **Nature**, v. 168, p. 140, 1951.
87. TREUMANN, R.; KIOS, Z.; PARROT, M. Physics of Electric Discharges in Atmospheric Gases: An Informal Introduction. **Space Sci Rev**, v. 137, p. 133–148, 2008.
88. SOLDERA, F. et al. Determination of the cathode erosion and temperature for the phases of high voltage discharges using FEM simulations. **Computational Materials Science**, v. 32, p. 123–139, 2005.
89. THOMSON, J. J. Cathode Rays. **Philos. Mag.**, v. 44, n. 293, 1897.
90. DAVIS, E.; FALCONER, I. **J.J. Thompson And The Discovery Of The Electron**. London : Taylor & Francis, 1997.
91. SELIGER, R. et al. A high-intensity scanning ion probe with submicrometer spot size. **Appl. Phys. Lett.**, v. 34, n. 5, 1979.
92. REYNTJENS, S.; PUERS, R. A review of focused ion beam applications in microsystem technology. **J. Micromech. Microeng.**, v. 11, p. 287–300, 2001.
93. KANG, P.; SHAH, D. Filtration of Nanoparticles with Dimethyldioctadecylammonium Bromide Treated Microporous Polypropylene

- Filters. **Langmuir**, v. 13, p. 1820-1826, 1997.
94. ZHANG, R.; KOPLIK, J. Separation of nanoparticles by flow past a patterned substrate. **PHYSICAL REVIEW E**, v. 85, n. 2, p. 026314, 2012.
95. KRINKE, T.; FISSAN, H. Positioning of nanometer-sized particles on flat surfaces by direct deposition from the gas phase. **APPLIED PHYSICS LETTERS**, v. 78, n. 23, 2001.
96. BARRY, C.; GU, J.; JACOBS, H. Charging Process and Coulomb-Force-Directed Printing of Nanoparticles with Sub-100-nm Lateral Resolution. **NanoLetters**, v. 5, n. 10, p. 2078-2084, 2005.
97. GALLIKER, R. et al. Direct printing of nanostructures by electrostatic autofocussing of ink nanodroplets. **Nature Communications**, v. 3, n. 390, 2012.
98. COMISKEY, B. et al. An electrophoretic ink for all-printed reflective electronic displays. **Nature**, v. 394, p. 253-255, 1998.
99. JACOBSON, J.; COMISKEY, B. **Nonemissive displays and piezoelectric power supplies therefor**. US5930026, 27 jul. 1999.
100. SHACKELFORD, J. F.; ALEXANDER, W. CRC Materials Science and Engineering Handbook. [S.l.]: CRC Press, 2000. p. 568.
101. ABDEL-KADER, A. et al. Chemical analysis and electrical conductivity of tellurium phosphate glasses doped with bismuth oxide. **Journal of Materials Science**, v.

## Bibliography

26, n. 16, p. 4298-4302, 1991.

102. EL-MALLAWANY, R.; ABBAS AHMED, I. Thermal properties of multicomponent tellurite glass. **Journal of Materials Science**, v. 43, n. 15, p. 5131-5138, 2008.
103. BROWN , T. E. et al. Chemistry: The Central Science. Upper Saddle River, NJ: Prentice Hall, 2000. p. 884. Disponivel em:  
<<http://www.crystran.co.uk/uploads/files/73.pdf>>.
104. LEE, H.; CHOUA, K.; SHIH, Z. Effect of nano-sized silver particles on the resistivity of polymeric conductive adhesives. **International Journal of Adhesion & Adhesives**, v. 25, p. 437-441, 2005.
105. HSU, C.; YANG, Y.; WOOD, K. Self-Assembled Patterns and Percolation Thresholds of 2D Nanoparticle Films Formed by Colloidal Droplet Evaporation. **CHINESE JOURNAL OF PHYSICS**, v. 45, n. 6-II, p. 686, 2007.
106. EINSTEIN, A. Investigations on the Theory of the Brownian Movement. **Annalen der Physik**, v. 17, p. 549, 1905.
107. RICCI, E.; NOVAKOVIC, R. Wetting and Surface Tension Measurements on Gold Alloys. **Gold Bulletin**, v. 34, n. 2, 2001.
108. MARDIKYAN, K. et al. AC breakdown strength of N<sub>2</sub>, SF<sub>6</sub> and a mixture of N<sub>2</sub>+SF<sub>6</sub> contacting a small amount of SF<sub>6</sub>. **Conference Record of the 1996 IEEE International Symposium on Electrical Insulation**, v. 2, p. 763 - 765, 1996.

109. MARDIKYAN, K. Breakdown strength of air, SF<sub>6</sub> and a mixture of air plus SF<sub>6</sub> containing a small amount of SF<sub>6</sub>. **European Transactions on Electrical Power**, v. 9, n. 5, p. 313-316, 1999.
110. POOTAWANG, P. et al. Synthesis and characteristics of Ag/Pt bimetallic nanocomposites by arc-discharge solution plasma processing. **Nanotechnology**, v. 23, p. 395602, 2012.
111. BYEON, J.; PARK, J.; HWANG, J. Spark generation of monometallic and bimetallic aerosol nanoparticles. **Journal of Aerosol Science**, v. 39, n. 10, p. 888–896, 2008.
112. FORSTER, H.; WOLFRUM, C.; PEUKERT, W. Experimental study of metal nanoparticle synthesis by an arc evaporation/condensation process. **J. Nanopart Res.**, v. 14, n. 926, 2012.
113. LIU, S. et al. Synthesis of silicon nanowires and nanoparticles by arc-discharge in water. **Chem. Commun.**, p. 4690–4692, 2005.
114. MARDANIAN, M.; NEVAR, A.; TARASENKO, N. Optical properties of silicon nanoparticles synthesized via electrical spark discharge in water. **Appl Phys A**, 2012.
115. GARWIN, E.; SCHWYN, S.; SCHMIDT-OTT, A. AEROSOL GENERATION BY SPARK DISCHARGE. **J. Aerosol Science**, v. 19, n. 5, p. 639-642, 1988.

## Bibliography

116. ROTH, C. et al. Generation of Ultrafine Particles by Spark Discharging. **Aerosol Science and Technology**, v. 38, p. 228–235, 2004.
117. MOSBAH, A.; CALKA, A.; WEXLER, D. Rapid synthesis of titanium nitride powder by electrical discharge assisted mechanical milling. **Journal of Alloys and Compounds**, v. 424, p. 279–282, 2006.
118. DHAWAN, A.; MUTH, J. Plasmon resonances of gold nanoparticles incorporated inside an optical fibre matrix. **Nanotechnology**, v. 17, p. 2504–2511, 2006.
119. LIN, A.; HAN, W. Au-nanoparticle-incorporated germano-silicate glass fiber with high resonant nonlinearity. **Journal of Nanophotonics**, v. 1, p. 013554, 2007.
120. CONROY, R. et al. Optical waveguiding in suspensions of dielectric particles. **APPLIED OPTICS**, v. 44, n. 36, p. 7853, 2005.
121. LIU, J.; LU, Y. A Colorimetric Lead Biosensor Using DNAzyme-Directed Assembly of Gold Nanoparticles. **J. AM. CHEM. SOC.**, v. 125, p. 6642–6643, 2003.
122. DANIEL, M.; ASTRUC, D. Gold Nanoparticles: Assembly, Supramolecular Chemistry, Quantum-Size-Related Properties, and Applications toward Biology, Catalysis, and Nanotechnology. **Chem. Rev.**, v. 104, p. 293–346, 2004.
123. KAYANI, A. et al. Optofluidics incorporating actively controlled micro- and nano-particles. **BIOMICROFLUIDICS**, v. 6, p. 031501, 2012.

124. LIN, A.; WATEKAR, P.; HAN, W. Visible Optical Limiting Property of Germano-Silicate Glass Fibers with Au Nanoparticles Incorporated. **Journal of the Korean Physical Society**, v. 53, n. 3, p. 1315-1318, 2008.
125. BANKS, D. et al. Ballistic laser-assisted solid transfer (BLAST) from a thin film precursor. **OPTICS EXPRESS**, v. 16, n. 5, p. 3249, 2008.
126. FEINAEUGLE, M. et al. **Deposition of elements for a thermoelectric generator via laser-induced forward transfer**. Lasers and Electro-Optics (CLEO). San Jose: [s.n.]. 2012.
127. MARDANIAN, M.; NEVAR, A.; TARASENKO, N. Optical properties of silicon nanoparticles synthesized via electrical spark discharge in water. **Applied Physics A**, v. 109, 2012.
128. RYSANEK, F.; BURTON, R. Charging of Macroparticles in a Pulsed Vacuum Arc Discharge. **IEEE Transactions on Plasma Science**, v. 36, n. 5, p. 2147-2162, 2008.
129. HULL, A.; LANGMUIR, I. Control of an Arc Discharge by Means of a Grid. **Proc Nat. Acad. Sci.**, v. 15, n. 3, p. 218-225, 1929.
130. CLEMENTI, E.; RAIMONDI, D. L. Atomic Screening Constants from SCF Functions. **Journal of Chemical Physics**, v. 38, n. 11, p. 2686, 1963.
131. SLATER, J. C. Atomic Radii in Crystals. **Journal of Chemical Physics**, v. 41, n. 10,

## Bibliography

p. 3199, 1964.